UNIVERSIDADE FEDERAL DE SANTA CATARINA
CAMPUS TRINDADE - CENTRO TECNOLÓGICO
PROGRAMA DE PÓS-GRADUAÇÃO EM ENGENHARIA DE AUTOMAÇÃO E SISTEMAS

Luiz Henrique Tonon Schmidt

Analysis and Design of Passive Capacitor Voltage Balancing in Modular Multilevel Converter During Precharge Operation

Florianópolis
2020

Luiz Henrique Tonon Schmidt

Analysis and Design of Passive Capacitor Voltage Balancing in Modular Multilevel Converter During Precharge Operation

Dissertação submetida ao Programa de Pós-Graduação em Engenharia de Automação e Sistemas da Universidade Federal de Santa Catarina para a obtenção do título de mestre em Engenharia de Automação e Sistemas.
Supervisor: Prof. Daniel Juan Pagano, Dr.
Co-supervisor: Rony Cristiano, Dr.

Florianópolis
2020

Ficha de identificação da obra elaborada pelo autor,
através do Programa de Geração Automática da Biblioteca Universitária da UFSC.

Schmidt, Luiz Henrique Tonon
Analysis and design of passive capacitor voltage balancing in modular multilevel converter during precharge operation / Luiz Henrique Tonon Schmidt ; orientador, Daniel Juan Pagano, coorientador, Rony Cristiano, 2020.
122 p.

Dissertação (mestrado) - Universidade Federal de Santa Catarina, Centro Tecnológico, Programa de Pós-Graduação em Engenharia de Automação e Sistemas, Florianópolis, 2020.

Inclui referências.

1. Engenharia de Automação e Sistemas. 2. Sistemas dinâmicos não lineares. 3. Eletrônica de potência. I. Pagano, Daniel Juan. II. Cristiano, Rony. III. Universidade Federal de Santa Catarina. Programa de Pós Graduação em Engenharia de Automação e Sistemas. IV. Título.

Luiz Henrique Tonon Schmidt

Analysis and Design of Passive Capacitor Voltage Balancing in Modular Multilevel Converter During Precharge Operation

O presente trabalho em nível de mestrado foi avaliado e aprovado por banca examinadora composta pelos seguintes membros:

Prof. Hector Bessa Silveira, Dr.
Universidade Federal de Santa Catarina

Prof. Marcelo De Lellis Costa de Oliveira, Dr.
Universidade Federal de Santa Catarina

Prof. Marcelo Lobo Heldwein, Dr.
Universidade Federal de Santa Catarina

Certificamos que esta é a **versão original e final** do trabalho de conclusão que foi julgado adequado para obtenção do título de mestre em Engenharia de Automação e Sistemas.

Documento assinado digitalmente
Werner Kraus Junior
Data: 03/08/2020 14:39:12-0300
CPF: 531.085.239-53

Prof. Werner Kraus Jr., Dr.
Coordenador do Programa

Documento assinado digitalmente
Daniel Juan Pagano
Data: 03/08/2020 13:47:57-0300
CPF: 762.839.419-15

Prof. Daniel Juan Pagano, Dr.
Supervisor:

Florianópolis, 04 de Junho de 2020.

ACKNOWLEDGEMENTS

My sincere gratitude to everyone that has collaborated to this work.

To my advisor, prof. Pagano, for the partnership and being always willing to help. For the knowledge passed on, the comprehension during difficult times and for trusting me to do this work. As well as to my co-advisor, Rony, also always willing to help and improve the work.

To prof. Marcelo Lobo and Gean, who have helped to come up with this research subject, and also for all the collaboration during the work - exchange of ideas, help with the experiments and also for the collaboration in the research paper written based on this thesis.

To the members of the examining board, prof. Marcelo De Lellis, prof. Hector and prof. Marcelo Lobo, that have accepted the invitation to contribute with their time and attention for the improvement of this work.

To my family, specially my parents, Marize and Luiz Alberto (in memorian) and my sister, Maria Cristine, for all the generosity, love, dedication and support in this life.

To all my friends in the PGEAS, especially Dado, Thamiris, Julio, Thiesco, Alan, Jean, Carla, Bernardo, Fábio, Gabriel, Lucas, Renan, Diogo, Sid and Feres. For helping in technical or personal matters, but mostly for making the days so much lighter, for bringing so much fun, both in times of joy and in difficult times. The same goes for friends in other circles, like Matias, Heron, Denise, Diego, Henrique, Hector, Inez, Doris, Kleber, Lúcio, Fábio, Lucas, Bruno, Leo, Ana, Gui, and many others, whose names are not explicitly written here, and may not have been present so often, but also contributed in some way, for which I thank.

To all the teachers who taught me during the master period.

To the administrative members of the PGEAS, especially Ênio, Lívia, Rodrigo and prof. Werner, always wiling to help. To the Federal University of Santa Catarina, and to the Personnel Improvement Coordination of Superior Level (CAPES), for funding and making this thesis feasible.

To all the people somehow contributed to the realization of this work and are not explicitly listed above.

ABSTRACT

The Modular Multilevel Converter (MMC) is a topology that has been increasingly attracting interest in research. It is applied in High Voltage Direct Current systems (HVDC), Medium Voltage Drives (MVD), and integration of renewable power sources to a grid. Some advantages of this topology are its modular design, based on the connection of submodules (SMs), which facilitates its manufacturing and maintenance, and possibility of operating without bulky transformers and output filters. It is advantageous that each SM local signal electronics circuits is self-powered by means of a power supply fed from the respective SM capacitor. This configuration, however, can lead to unbalanced and even unstable voltages during the precharge process. The balancing of the MMC's capacitor voltages during its precharge stage is crucial to its correct operation. A passive balancing strategy consisting in adding a balancing resistance in parallel with each SM is analyzed in this work. An instantaneous piecewise smooth (PWS) nonlinear model is proposed. The system nonlinear dynamics are analyzed for a system with two SMs. Conditions for local stability of the operating point are obtained, and the results are extended for a system with an arbitrary number of SMs. The effects of variation of the balance resistance in the dynamics of the system are studied. Also, conditions for global stability are obtained for a system with two SMs, and some guidelines for the design of the balancing resistance are proposed.

Keywords: Modular Multilevel Converter. Voltage Balancing. Stability. Nonlinear Dynamics. Piecewise Smooth Systems.

RESUMO

O Conversor Modular Multinível (MMC) é uma topologia que vem atraindo muito interesse em pesquisa. Suas aplicações incluem sistemas de Alta Tensão em Corrente Contínua, acionamentos em médias tensões e integração de fontes renováveis a uma rede. Algumas vantagens desta topologia são seu design modular baseado na conexão de submódulos, que facilita sua fabricação e manutenção, e possibilidade de operação sem transformadores e filtros de saída. É vantajoso que cada circuito eletrônico local de sinais de cada submódulo seja alimentado por uma fonte auxiliar conectada ao respectivo capacitor deste submódulo, e que todos sejam alimentados por uma fonte conectada à porta de corrente contínua do conversor. Entretanto, durante a etapa de pré-carga este arranjo pode não levar a tensões balanceadas ou mesmo estáveis nos capacitores dos submódulos. O balanço das tensões nos capacitores do MMC durante sua précarga é crucial para sua operação correta. Uma estratégia passiva de balanceamento que consiste em adicionar uma resistência de balanço em paralelo com cada um dos submódulos é analisada neste trabalho. É proposto um modelo instantâneo e suave por partes levando em conta as dinâmicas não lineares deste sistema. Estas são analisadas para um sistema com dois submódulos. São obtidas condições para estabilidade local do ponto de operação do sistema, e o resultado é estendido para um sistema com número arbitrário de submódulos. É estudado o efeito da variação da resistência de balanço nas dinâmicas do sistema. Também se obtém condições de estabilidade global para um sistema com dois submódulos, e se propõe algumas diretrizes para o projeto da resistência de balanço. Experimentos confirmam os resultados analíticos e de simulação.

Palavras-chave: Conversor Modular Multinível. Balanceamento de Tensões. Estabilidade. Dinâmicas Não Lineares. Sistemas Suaves por Partes.

RESUMO EXPANDIDO

Introdução

O Conversor Modular Multinível (MMC) é uma topologia que vem atraindo muito interesse em pesquisa. Suas aplicações incluem sistemas de Alta Tensão em Corrente Contínua, acionamentos em médias tensões e integração de fontes renováveis a uma rede. Algumas vantagens desta topologia são seu design modular baseado na conexão de submódulos (SM), que facilita sua fabricação e manutenção, e possibilidade de operação sem transformadores e filtros de saída, que podem ser bastante pesados ou volumosos.

Um dos aspectos do funcionamento do MMC é a sua operação de précarga. Embora menos reportada na literatura do que temas como sua modelagem, projeto, sistemas de controle ou técnicas de modulação empregadas, é um problema que deve ser considerado em aplicações práticas. A précarga consiste em carregar os capacitores dos SM até um nível mínimo antes de conectar o conversor com a rede para evitar a entrada de correntes de grande magnitude, que podem danificar o conversor.

Diversas soluções existem na literatura para tentar resolver este problema. Uma delas é adequada para se usar no caso em que conectado a cada SM há uma fonte auxiliar, usada para alimentar circuitos de comunicação, controle, e sensores nos SM, entre outros. Nesta configuração ainda, a fonte auxiliar é alimentada pelo capacitor de cada submódulo - Isso é vantajoso pois nessa configuração seu projeto acaba se tornando mais simples. Entretanto, as fontes introduzem instabilidade, desbalanceando as tensões nos capacitores. Os próprios controladores são alimentados por essas fontes e precisam de uma tensão mínima para funcionar, o que justifica o emprego de uma solução passiva. Esta consiste em conectar uma resistência de balanceamento em paralelo com cada SM, o que causa o balanceamento das tensões.

Embora seja uma estratégia pertinente, foram identificadas limitações na forma em que é exposta na literatura. O cálculo das resistências para obter a estabilidade foi feito em um sistema considerando apenas um SM, e a rigor seu resultado não pode ser estendido para sistemas maiores. Além disso, foram identificadas situações em que o valor teórico proposto não é suficiente para balancear as tensões nos capacitores. Também observou-se que a medida em que se os valores das capacitâncias dos SMs se desviam dos valores nominais, um valor da resistência de balanceamento que era a priori suficiente, o deixa de ser. Desvios dos valores das capacitâncias ocorrem na prática, devido ao envelhecimento dos componentes ou mesmo devido à tolerâncias de fabricação.

Estas limitações e questões motivaram o presente trabalho. Este tem o intuito de realizar uma análise de estabilidade em profundidade da solução proposta, e propor orientações para o projeto da resistência de balanceamento, tendo em vista que um projeto adequado do conversor deveria levar em conta a estabilidade e comportamento dinâmico durante o processo de précarga. Os objetivos do trabalho estão descritos a seguir.

Objetivos

OBJETIVO GERAL

Modelar e analisar as dinâmicas da operação de précarga com a resistência de balanço, para analisar sua estabilidade levando em consideração variações paramétricas na resistência de balanço e capacitâncias dos SM, e adequadamente projetar a resistência de balanço.

OBJETIVOS ESPECÍFICOS

1. Modelar as dinâmicas instantâneas da operação de précarga do MMC durante o estágio não controlado.
2. Analisar as dinâmicas não lineares de um sistema simplificado com apenas dois SM em toda faixa de operação do sistema, não apenas no ponto de operação.
3. Investigar sobre a estabilidade do ponto de operação.
4. Investigar a influência da variação paramétrica nas dinâmicas do sistema, especificamente a variação da resistência de balanceamento e capacitâncias dos SM.
5. Propor orientações para ajudar no projeto da resistência de balanço.

Metodologia

A dissertação foi realizada seguindo-se os passos e ferramentas abaixo:

- Uma revisão da literatura foi realizada a fim de confirmar a relevância científica e de aplicação do problema estudado. O problema foi inicialmente proposto por colegas do Departamento de Engenharia Elétrica da Universidade Federal de Santa Catarina. Com base em um conhecimento inicial proveniente de discussões a artigos, fez-se uma busca exploratória inicial para se levantar palavras chave sobre o tema. Com base nisso, foram buscados artigos nas principais bases de dados e selecionados os mais relevantes. Através de uma leitura inicial mais rápida, pode-se identificar diferentes abordagens e linhas de pesquisa. Uma destas linhas era coerente com o problema e algumas das propostas de solução discutidas inicialmente, e esta foi estudada mais a fundo.
- Ferramentas de análise de sistemas não lineares foram escolhidas para analisar o problema, como análise qualitativa e de sistemas suaves por partes. Este tipo de ferramenta foi escolhida pois o orientador já possuía experiência com estas técnicas e o autor já possuía alguma experiência prévia. Também por que elas já foram utilizadas com sucesso na análise de sistemas não lineares, o qual o sistema estudado se enquadra, e em particular em problemas na área da eletrônica de potência (CRISTIANO et al., 2018; CESAR et al., 2017).
- Foi feita a modelagem de uma versão simplificada do problema em um modelo instantâneo, suave por partes e não linearizado, fenomenológico, adequado para se tratar o problema em questão.

- Análises qualitativas feitas com o auxílio de ferramentas de computação simbólica foram realizadas.
- Também foram empregadas ferramentas de computação numérica e de simulação. Estas facilitaram o entendimento e também auxiliaram o direcionamento das análises simbólicas ao longo do trabalho. Estas foram especialmente úteis para se investigar a efeitos das variações paramétricas no modelo proposto.
- Experimentos foram realizados afim de se testar a efetividade da solução proposta.

É importante ressaltar que nem todas estas etapas foram realizadas de forma exclusivamente sequencial. As ferramentas de simulação, por exemplo, auxiliaram na investigação e direcionamento das análises simbólicas e vice-versa. O escopo do trabalho também mudou ao longo do processo conforme se verificava sua viabilidade e se amadureceu o entendimento sobre o problema estudado.

Resultados e Discussão

Esta dissertação resultou nas seguintes contribuições:

- Um modelo instantâneo considerando as não linearidades do sistema estudado, modelado como um sistema suave por partes.
- Para o método de balanceamento passivo estudado, condições analíticas para estabilidade local do ponto de operação são derivadas para um sistema com número arbitrário de SMs.
- Análises qualitativas de uma versão simplificada do problema, um sistema com apenas dois SMs, para investigação do comportamento dinâmico do sistema.
- Simulações numéricas ilustram os resultados da análise para o caso nominal e também a influência de variações paramétricas nas dinâmicas do sistema.
- Um resultado experimental no qual a solução proposta funciona.
- Condições para estabilidade global do sistema foram determinadas para um sistema simplificado com dois SM por fase.
- Orientações que auxiliam no projeto da resistência de balanceamento são propostas.

Os objetivos foram alcançados de forma satisfatória. Algumas das análises feitas podem ser aprofundadas ou pode-se tentar expandi-las para casos mais gerais. O problema da précarga é de relevância para aplicação prática do conversor, embora receba menos atenção que outros temas como modelagem, técnicas de controle ou modulação. Também não é comum o emprego de técnicas de análises de sistemas não lineares para este problema específico. Os resultados obtidos mostram que essas técnicas podem ser empregadas de forma promissora, e o entendimento das dinâmicas do sistema pode até mesmo direcionar a busca de soluções de caráter mais heurístico, como ocorre em problemas de engenharia e aqui em particular considerando aplicações da eletrônica de potência.

Considerações Finais

Trabalhos futuros podem ser conduzidos com base no conteúdo abordado nesta dissertação. A operação de précarga pode ser estudada para um sistema trifásico, a partir do estudo simplificado de um SM por fase. Os mesmos métodos e ferramentas podem ser utilizados para estudo de um sistema ativo de balanceamento, por exemplo comutando as resistências de balanceamento. As mesmas técnicas e métodos utilizados podem ser empregados no estudo de um sistema tridimensional, o que pode ajudar a verificar a generalidade de alguns resultados obtidos para o sistema simplificado. Ferramentas de cálculo numérico podem auxiliar na abordagem do problema considerando o sistema geral com mais dimensões do que duas ou três. Modelos normalizados também podem ser utilizados para diminuir a complexidade do sistema estudado reduzindo o seu número de parâmetros, e também porque podem ser usados para se obter resultados mais gerais.

Palavras-chave: Conversor Modular Multinível. Balançeamento de Tensões. Estabilidade. Dinâmicas Não Lineares. Sistemas Suaves por Partes.

LIST OF FIGURES

LIST OF TABLES

LIST OF SYMBOLS

K_{ac}	Circuit breaker switch in the alternate current bus
Σ_1^+	Σ_1 part between $\boldsymbol{f}^{-+}$ and $\boldsymbol{f}^{++}$
Σ_1^-	Σ_1 part between $\boldsymbol{f}^{--}$ and $\boldsymbol{f}^{+-}$
$\boldsymbol{f}^{s1+}$	Sliding vector field in Σ_1^+
S_1	Switching cell 2 of a submodule
S_2	Switching cell 2 of a submodule
C	Capacitance of a submodule
K_1	Circuit breaker switch in the direct current bus
K_2	Circuit breaker switch bypassing the current limiting resistor
R_l	Current limiting resistance
R_b	Balancing resistance of a submodule
V_{DC}	Direct current bus voltage
L_a	Arm Inductance
P	Power consumed by the auxiliary power supply of a submodule
v_{Ci}	Capacitor voltage of the i-th submodule
$\boldsymbol{v_C}$	Vector of submodules' capacitor voltages
i_L	Current in the equivalent phase inductance
i_{Ci}	Capacitor current of the i-th submodule
i_{Pi}	Auxiliary power supply current of the i-th submodule
i_{Rbi}	Balancing resistance current of the i-th submodule
t	time
V_{Cmin}	Minimum voltage necessary for turning on the auxiliary power supplies
P_{APSi}	Power consumed by the i-th submodule's auxiliary power supply in extended model
h_i	Scalar functions corresponding to the i-th submodule that delimits the turning on/off for the auxiliary power supply in the extended model
$\mathbb{D}$	Domain in which the two submodules system is analyzed
Σ_1	First Switching boundary
Σ_2	Second Switching boundary
$\mathbb{D}_1$	First region of the two submodule system domain
$\mathbb{D}_2$	Second region of the two submodule system domain
$\mathbb{D}_3$	Third region of the two submodule system domain
$\mathbb{D}_4$	Fourth region of the two submodule system domain
$\boldsymbol{f}$	Vector field representing the two submodule system
$\boldsymbol{f}^{--}$	Vector field representing the two submodule system with both auxiliary power supplies turned off
$\boldsymbol{f}^{-+}$	Vector field representing the two submodule system with only the second auxiliary power supply turned on

$\boldsymbol{f}^{+-}$	Vector field representing the two submodule system with only the first auxiliary power supply turned on
$\boldsymbol{f}^{++}$	Vector field representing the two submodule system with both auxiliary power supplies turned off
$\boldsymbol{0}$	Null vector
$\boldsymbol{E}^{--}$	Equilibrium point of $\boldsymbol{f}^{--}$
$\boldsymbol{A}^{--}$	Jacobian matrix of $\boldsymbol{f}^{--}$ in respect to $\boldsymbol{v_C}$
$\boldsymbol{E}_{\boldsymbol{1}}^{-+}$	First equilibrium point of $\boldsymbol{f}^{-+}$
$\boldsymbol{E}_{\boldsymbol{2}}^{-+}$	Second equilibrium point of $\boldsymbol{f}^{-+}$
P_{2c}^{-+}	P_2 critical value that delimits the existence of $\boldsymbol{E}_{\boldsymbol{1}}^{-+}$ and $\boldsymbol{E}_{\boldsymbol{2}}^{-+}$
$\boldsymbol{A}^{-+}$	Jacobian matrix of $\boldsymbol{f}^{-+}$ in respect to $\boldsymbol{v_C}$
$\boldsymbol{E}_{\boldsymbol{1}}^{++}$	First equilibrium point of $\boldsymbol{f}^{++}$
$\boldsymbol{E}_{\boldsymbol{2}}^{++}$	Second equilibrium point of $\boldsymbol{f}^{++}$
$\boldsymbol{E}_{\boldsymbol{3}}^{++}$	Third equilibrium point of $\boldsymbol{f}^{++}$
$\boldsymbol{E}_{\boldsymbol{4}}^{++}$	Fourth equilibrium point of $\boldsymbol{f}^{++}$
P_{c14}^{++}	P critical value that delimits the existence of $\boldsymbol{E}_{\boldsymbol{1}}^{++}$ and $\boldsymbol{E}_{\boldsymbol{4}}^{++}$
P_{c23}^{++}	P critical value that delimits the existence of $\boldsymbol{E}_{\boldsymbol{2}}^{++}$ and $\boldsymbol{E}_{\boldsymbol{3}}^{++}$
$\boldsymbol{A}^{++}$	Jacobian matrix of $\boldsymbol{f}^{++}$ in respect to $\boldsymbol{v_C}$
γ	Ratio between power consumed in the auxiliary power supply and in the balancing resistence
i_{R_l}	Current in the limiting current resistance
γ_{max}	Maximum possible value of γ
∇h_1	Gradient vector of h_1 in respect to $\boldsymbol{v_C}$
$L_{f^{--}}h_1$	Lie derivative of h_1 in respect to $\boldsymbol{f}^{--}$
$L_{f^{-+}}h_1$	Lie derivative of h_1 in respect to $\boldsymbol{f}^{-+}$
$L_{f^{+-}}h_1$	Lie derivative of h_1 in respect to $\boldsymbol{f}^{+-}$
$L_{f^{++}}h_1$	Lie derivative of h_1 in respect to $\boldsymbol{f}^{-+}$
Σ_1^{as}	Attractive sliding segment in Σ_1
$\boldsymbol{T}_{\boldsymbol{1}}^{-}$	Tangency point of $\boldsymbol{f}^{--}$ or $\boldsymbol{f}^{-+}$ in Σ_1
$\boldsymbol{T}_{\boldsymbol{1}}^{+}$	Tangency point of $\boldsymbol{f}^{+-}$ or $\boldsymbol{f}^{++}$ in Σ_1
$\boldsymbol{f}^{s\boldsymbol{1}-}$	Sliding vector field in Σ_1^-
$\boldsymbol{E}^{s\boldsymbol{1}-}$	Equilibrium point of $\boldsymbol{f}^{s\boldsymbol{1}+}$
$\boldsymbol{E}_{\boldsymbol{1}}^{s\boldsymbol{1}+}$	First equilibrium point of $\boldsymbol{f}^{s\boldsymbol{1}+}$
$\boldsymbol{E}_{\boldsymbol{2}}^{s\boldsymbol{1}+}$	Second equilibrium point of $\boldsymbol{f}^{s\boldsymbol{1}+}$

CONTENTS

1 INTRODUCTION

This introduction is composed of six sections. In section 1.1, we briefly present modular multilevel converter topology. In section 1.2, the problem of the precharge operation is defined. Also, we present a literature review and the state of the art in this subject, that motivated us to do this thesis. The thesis objectives are stated in section 1.3. In section 1.4 and 1.5 we show respectively the main contributions and further publication resulted from this research. In section 1.6 we present the structure of the present thesis.

1.1 THE MMC

The multilevel converters have a widespread usage in the industry and in power systems, since they allow the design of high and medium voltage system, with excellent output voltage quality (KOURO; RODRIGUEZ, et al., 2012) (KOURO; MALINOWSKI, et al., 2010) and also because semiconductors' maximum voltage ratings are usually lower than the system's input or output voltage, and the connection in series of many semiconductor devices can be challenging (KNAAK, 2011). One of these is the modular multilevel converter (MMC). This topology was first proposed by professor R. Marquardt (2001). The MMC was originally intended for applications in High Voltage Direct Current (HVDC) systems. The main advantages of using this converter are its modularity, scalability, high efficiency, transformer-less operation and direct current (DC) bus without capacitor (LESNICAR; MARQUARDT, 2003). The modular design also reduces manufacturing costs (DEBNATH et al., 2015). Among its disadvantages, are the elevated number of semiconductors and passive necessary components, and the high complexity of modulation and control schemes (SOUZA, 2014).

The MMC is used in several applications. For example in HVDC systems, in which it has become the most promising voltage source inverter (VSI), but also in variable speed drives, with advantages in relation to other converters like the Neutral Point Clamped (NPC) converter and the Cascaded-HBridge (CHB) in respect to the installed area and energy in DC port (FLOURENTZOU; AGELIDIS; DEMETRIADES, 2009). These capabilities have allowed manufacturers to develop MMC based machine drives (SIEMENS AG, 2017), and researchers to propose new MMC topologies and applications in medium voltage DC/DC conversion (ADAM et al., 2016), wind power (LYU; CAI; MOLINAS, 2018), energy storage systems (LACHICHI, 2014), static compensation, among others (GEYER; DARIVIANAKIS; VAN DER MERWE, 2015). Other applications are cited in (DEBNATH et al., 2015). Examples of applications can be seen in Figure 1.

Figure 1 – Examples of applications using the MMC.

First application in a HVDC system in the city of San Francisco.

Source – Knaak (2011).

Medium-voltage wind energy conversion system with integrated energy storage.

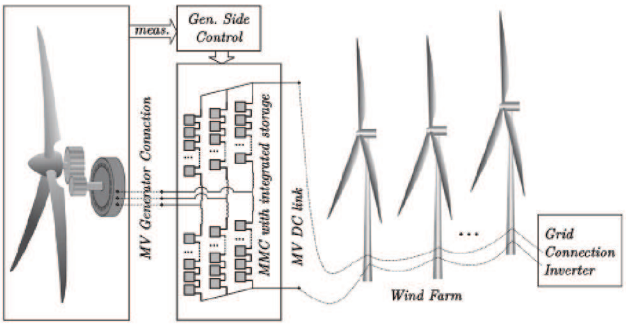

Source – Novakovic and Nasiri (2017).

Medium voltage drives, for industrial applications in general.

Source – Siemens AG (2017).

Figure 2 – MMC converter.

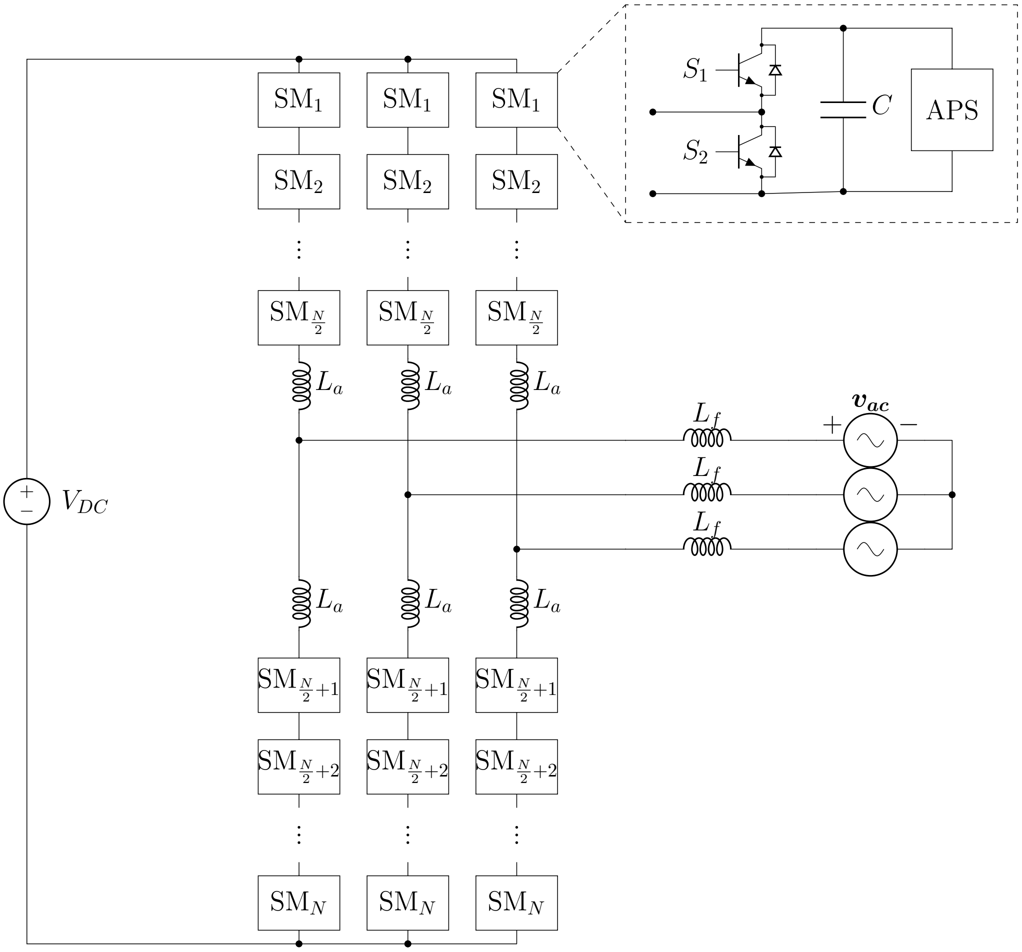

Source – Own Elaboration.

In Figure 2 we can see this topology is in one of its most common configurations, a three phase Alternate Current (AC) to DC[1]. This converter is bidirectional, that means it can work as a rectifier or as an inverter. The voltages in the AC and DC ports are respectively $\boldsymbol{v_{AC}}$ and V_{DC}. The MMC is composed of fundamental units called submodules (SM). A set with series connected submodules is called an arm, and two arms, one superior and one inferior, compose one phase leg of the MMC. The topology used within the SMs may vary, being the most common the half-bridge (HB), and full-bridge (FB) converters, connected to a capacitor (PEREZ et al., 2015). Summing up the output voltages of several SMs it is possible to have different levels of voltage in each phase. It is also possible to work with redundant SMs to provide fault tolerance capabilities. Also arm and filter inductors, represented by L_a and L_f respectively in Figure 2, compose the MMC. These are used to limit high frequency currents resulting from the differences between the arm generated voltages. Besides, they limit the growing-rate of DC current in case of a fault (SOUZA, 2014). It is also depicted in Figure 2 the parts that

---

[1] Alternative configurations are presented in (PEREZ et al., 2015).

constitute a SM. Besides the main components, the switching cell (S_1 and S_2) and the energy storage element C, a real converter submodule, to properly operate, needs other components including transistor's gate drivers, sensors, communication networks to transmit sensor readings and switching commands between between own SM and main command circuits (TOH; NORUM, 2013; ZHU et al., 2014). An auxiliary power supply is needed in each SM to power these components.

Each APS can be powered from its own submodule capacitor or externally through a high voltage isolated power supply system, with each approach having advantages and disadvantages. The latter allows the submodule controllers to perform test routines before the main power is connected, enabling early detection of failures in the control and communication systems. The always-on controller also simplifies the challenges of hot swapping submodules (COTTET et al., 2015). The APS cost and complexity, however, are high, since its insulation has to withstand medium/high working voltages. An APS designed to be powered from its own submodule has to insulate only the much lower SM capacitor voltage. On the other hand, the controllers can only perform test routines after the main power connection, decreasing chances of early detecting failures that could potentially lead to damage.

The connection of the converter to the grid can only be performed after precharging all capacitors to minimum voltage levels, that prevents inrush currents (SCHMIDT et al., 2019). The precharge operation can be done in different ways and it is better covered in the next session[2].

1.2 THE PRECHARGE

One often overlooked aspect of the MMC operation is the precharge operation. Though not so often reported in current literature as aspects of normal operation, it is a problem that must be considered in practical applications. All the capacitors need to be precharged to their nominal values before the MMC gets into operation. Otherwise, a large inrush current may occur at the system start, risking the integrity of the SMs or even the whole MMC (LI et al., 2015). These currents occur because if the MMC is connected to a nominal AC or DC bus with all capacitors discharged, the only thing opposing the growth of the current are the arm inductances, which use to be relatively small. The precharge operation can be made either via the AC or the DC port, via AC being used usually in HVDC systems and via DC in drive applications (ZHANG et al., 2017).

During the precharge, also, the SMs have three possible working states in gen-

---

[2] The complete operation of the MMC is a complex subject and out of scope of this work. There is a vast literature about its modeling, design, modulation techniques and control systems employed, among other topics. These are addressed in the literature review papers by Dekka et al. (2017) and Debnath et al. (2015).

eral. Either they are blocked, with both S_1 and S_2 closed, or they are bypassed, with S_2 turned on and S_1 turned off, disconnecting the capacitor from the arm, or yet they are inserted, with S_1 turned on and S_2 turned off (Figure 2). When the SM are blocked, they can be charged if the current flows through the freewheeling diode of S_1. Note that if the capacitor is paralleled with a bleeder resistor or an APS, used to discharge the capacitors when the MMC is turned off, and is disconnected from the arm for a long time (e.g., a few seconds), then it will still get discharged. We consider here the half-bridge topology for the SM, but other topologies can have the same behavior (LI et al., 2015).

Considering the case where the APS is fed internally, the precharge procedure can be divided into three stages, namely:

1. *Uncontrolled and inactive* – In this stage, the IGBTs of the SM are blocked. The precharge happens in all capacitors at the same time, with current flowing through the antiparallel diode of S_1. If the current goes in the oposite direction, the diodes do not conduct and the capacitor voltage is kept constant, or discharge if there is a parallel bleeding resistance connected to it.

2. *Uncontrolled and active* – This stage starts when all APSs are on. We can model the APS as a constant power load, which is associated with the system instability (LUO, 2018). In this stage, all the capacitor voltages can be measured and the IGBT S_1 and S_2 can just be manipulated. That usually follows a control law, and defines the third stage.

3. *Controlled* – In this stage the control system commands the switches S_1 and S_2 of each submodule according to an appropriate control strategy that targets bringing all capacitor voltages to their nominal values.

Several strategies have been proposed in order to realize the precharge. The first solution was proposed together with the MMC topology. It employs a low voltage DC source to charge the SMs one by one (LESNICAR; MARQUARDT, 2003). Some years later, a topology that includes four anti-parallel thyristors for each SM and the connection to external DC bus bars to accelerate the precharge process was proposed. However, the latter solution can increase complexity and costs by adding a significant number of extra semiconductor devices per SM (XU et al., 2011). Another alternative, tested for a specific topology, the clamp double submodule MMC (C-MMC), connects a C-MMC to the AC grid using a current limiting resistor and a breaker to bypass it after the precharge is over. It proposes that SM are charged in groups during a closed loop controlled precharge, and later, charges another C-MMC connected to the first in a back-to-back configuration, via its DC port (XUE; XU; TANG, 2014).

Some strategies are more recent. The one proposed in (TIAN et al., 2016) employs a low voltage DC source, and connects and disconnects the SM turning the equivalent circuit in a boost converter. Its advantages are that there is no need for a current limiting resistor and breaker, and is also flexible due to the boost topology used. However, it was tested by only charging SM one by one or two by two, which can be time consuming specially in MMC with an elevated number of SMs. Another closed-loop controlled precharge scheme is presented in (LI et al., 2015). This makes use of the current limiting resistor and circuit breaker, and can be used in both ports, AC or DC. Also, it charges all the SMs at the same time ensuring a reduced charging time. Even further, Zhang et al. (2017) propose a generalized precharging strategy, based on the adjustment of inserted and bypassed SMs and propose a sorting algorithm. This last can be used to precharge MMC with SM of diverse topologies, including the HB, full-bridge (FB), CD and three-level cross connected (3LCC).

Most of these strategies deal with the controlled stage of the precharge process. However, there is a problem that may happen during the uncontrolled stages. If the APSs are fed internally, tolerances in the capacitances or in the power consumed by the APSs may cause the system voltages to diverge during the uncontrolled stages. If they diverge largely enough, one of them may reach a lower or upper threshold and the whole MMC may be turned off for safety reasons. The solution in (LUO; CAO, et al., 2016) is a precharge through the DC port, using a current-limiting resistor R_l and a circuit breaker, and also propose the connection of a parallel resistor in order to stabilize the system during the uncontrolled stage. This solution is further developed in (LUO, 2018), where in controlled stage, the APS input current is manipulated in order to balance the capacitor voltages. Until the date of the present work completion, the present author has not found another work dealing with the problem of instability in the uncontrolled precharge stage.

Regarding the uncontrolled precharge stage, there are some limitations in current research, though. The stability proof in (LUO; CAO, et al., 2016) is made for only one SM, and can not be extrapolated for a MMC with arbitrary number of SM, or even for two per phase. Also, it is made only for the equilibrium operating point of the system, which is not necessarily sufficient for the system to work properly. Some preliminary studies and simulations have shown that, taking into account uncertainties or tolerance in the capacitance values the proposed solution is not sufficient. These uncertainties are present in practical cases and are associated with manufacturing tolerances and also with the aging of the components. Also, the uncontrolled and inactive stage dynamics are not modeled neither taken into account. There is a recent study that takes into account tolerances in the capacitance values, but it is made only numerically for a controlled precharge scheme (BISSAL; ALI, 2019). Also, stage 1 of the precharge operation dynamics are not modeled nor taken into account.

With the limitations of the previous seen solutions in mind, we consider a precharge scheme similar presented in Figure 3. This is similar to the one addressed by Luo (2018): the precharge is made from the DC side, simultaneously charging all the SMs, internally fed APS and a balancing resistance R_b in parallel with each SM. The difference is that it also has the commonly employed current limiting resistance R_l together with a circuit breaker composed of the switches K_1 and K_2. This scheme is based on a circuit prototype we have in our facilities and makes it possible for the three stages of the precharge to happen. The circuit breaker K_{ac} is considered open during the precharge process.

First K_1 is turned on, beginning the uncontrolled and inactive stage. Then, if the voltages in the capacitors reach a minimum level, the APSs turn on, characterizing the uncontrolled and active stage. Finally, when all the APS are turned on, the switch K_2 is turned on and K_1 is turned off, bypassing the current limiting resistance R_l. Finally, the controlled precharge begins, rising the capacitor voltages to their nominal values[3].

Figure 3 – MMC converter and its precharge circuit.

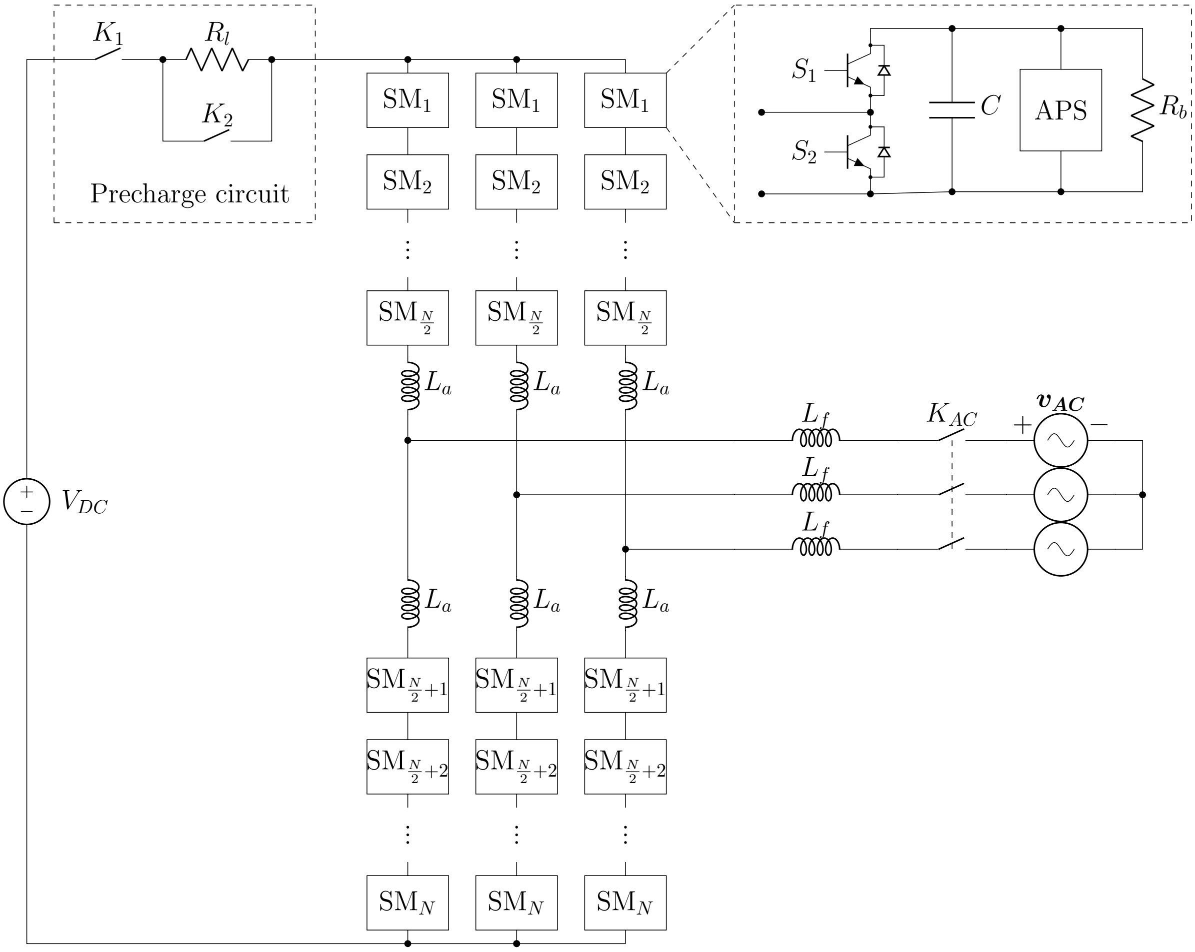

Source – Adapted from (SCHMIDT et al., 2019).

---

[3] An additional circuit could be used to remove R_b from the circuit once the MMC is working during normal operation in order to improve efficiency. The converter will still work properly, since its control system can be used to balance the capacitor voltages after the precharge process is complete.

The aim of this work is to present an in-depth analysis of the stability of the first and second stages and to provide a guideline for choosing R_b. The main motivation is to overcome the problem of instability in these stages. An adequate design of the MMC should take in consideration the stability in dynamic behavior during the precharge process.

We begin by modeling the system corresponding to the precharge process equivalent circuit. The model is phenomenological, as it is usual in power electronic systems, and instantaneous, in order to model all the system dynamics. The dynamics of the stage 1 of the precharge process are modeled as a piecewise smooth system (PWS). Tools for qualitative analysis of nonlinear systems, such as the Hartman-Grobman theorem, the Filippov convention for dynamics in switching boundaries, representations on the phase plane and bifurcation theory are used in order to analyze the system dynamics. Part of the analysis was made with the aid of symbolic computational tools. Numerical simulations of different cases illustrate the analytical results and give quantitative insight about parameter dependencies, like the variation of the balancing resistance and the capacitances values.

1.3 OBJECTIVES

Main Objective

To model and to analyze the dynamics of the MMC precharge operation with balancing resistance, in order to analyze its stability taking into account parametric variation of the balancing resistance and the SMs capacitances and to properly design the balancing resistance.

Specific Objectives

1. To model the instantaneous dynamics of the MMC precharge operation during stages 1 and 2.

2. To analyze the nonlinear dynamics of a simplified system with only two SM in the system operating range, not just in the operating point.

3. To investigate the stability of the operating point.

4. To investigate the influence of parametric variation on the system dynamics, specifically the variation of the balancing resistance and SMs capacitances.

5. To propose guidelines to help the design of the balancing resistance.

1.4 WORK CONTRIBUTIONS

- An instantaneous model taking into account the nonlinearities of the system, modeled as a piecewise smooth (PWS) system. It models the first and second stages of the precharge.
- For the studied passive balancing method, analytical conditions for the local stability of the operating point are derived for a system with an arbitrary number of SMs.
- Qualitative analysis of a simplified version of the problem, in a system with only two SM, in order to investigate the system dynamic behavior.
- Numerical simulation illustrate the analysis results in nominal case and also the influence of parametric variation on the sytem dynamics.
- An experimental result in which the proposed solution works.
- Conditions for the global stability were determined for a system with two submodules per phase.
- Guidelines that help in the design of the balancing resistance were proposed.

1.5 RESULTING PUBLICATION

- This work resulted in the publication and presentation of the paper entitled "Passive Capacitor Voltage Balancing in Modular Multilevel Converter During its Precharge: Analysis and Design" at the 15th Brazilian Power Electronics Conference and 5th IEEE Southern Power Electronics Conference (SCHMIDT et al., 2019)

1.6 THESIS STRUCTURE

This thesis is composed of 7 chapters. In chapter 2, the modeling of stages 1 and 2 of the precharge operation is made. In chapter 3, an analysis of a simplified system with two submodules is made, in order to better understand the system dynamics. In chapter 4, simulations are used to illustrate the cases analyzed in Chapter 3 and to investigate parameter variation influence on the system dynamics. In chapter 5, experimental results are presented. In chapter 6, the conditions needed to guarantee global stability are proved, for a system with two submodules per phase. The last chapter is the conclusion, synthesizing all the work main results and presenting perspective of future works.

2 MODELING

In this chapter, we propose a model for the precharge dynamics during uncontrolled stage, active and inactive. The model proposed here is used in chapter 3 for the analysis of a simplified version of the problem, from which results regarding the stability of the operating point and design of R_b are obtained. The model is also is used in chapter 4 for simulation and numerical results that illustrate the system dynamics and also for investigation of the influence of parametric variation in the system dynamics. Finally, it is used in chapter 6 to obtain the results about global stability of the operating point in the simplified system.

In section 2.1, a model for the active stage, in which all the APSs are turned on, is made. In section 2.2, this model is extended to a PWS one that represents both active and inactive dynamics and also the transition from inactive to active. This is the model used in the next chapters. After the models are presented, a numerical example illustrating the validity of one of the modeling assumptions, that the effect of L_a can be neglected, is shown in section 2.3. Finally, in section 2.4, a summary of this chapter is presented.

2.1 UNCONTROLLED AND ACTIVE STAGE OF PRECHARGE OPERATION

We begin by analyzing the uncontrolled precharge process of one phase of the MMC precharge circuit (Figure 4 (a)). At the beginning, all the capacitors are discharged, and all the IGBTs are switched off and blocked. Then, K_1 closes, current flows through the anti parallel diode in S_1. The equivalent circuit of the uncontrolled and inactive stage of precharge can be seen in Figure 4 (b). For means of simplicity, we begin by analyzing the precharge in only one phase. The voltage from the DC bus is V_{DC}, R_l is the precharge current limiting resistance, $2L_a$ is the equivalent arm inductance, C_i are the SM capacitances, P is the power consumed in the APS, modeled as a constant power load, as in Luo, Zhang, et al. (2018), and R_{bi} is the balancing resistance of the i-th SM, for $i \in \{1,2,\ldots,N\}$, being N, the number of SMs per phase, an even number.

The main goal of the modeling is for analysis of the dynamics, so that we can investigate the system stability and properly design the balancing resistance. A state space, time-domain, instantaneous and not linearized model is suitable for that goal. Not linearized, because we know that the APS can be modeled by a constant power load, that is a nonlinearity associated with the system instability. Instantaneous, instead of the average-value model commonly used in power electronics because we intend to model the dynamics in the uncontrolled stage, which lead the system to the operating point, and they are essentially transitory. Besides, qualitative analysis tools can be used with that model in order to investigate the system stability.

Figure 4 – MMC precharge circuit (a) and equivalent circuit during uncontrolled precharge (b). In the equivalent circuit, K_1 is closed, K_2 open, K_{ac} is open, all the IGBT are blocked and the APS are turned on.

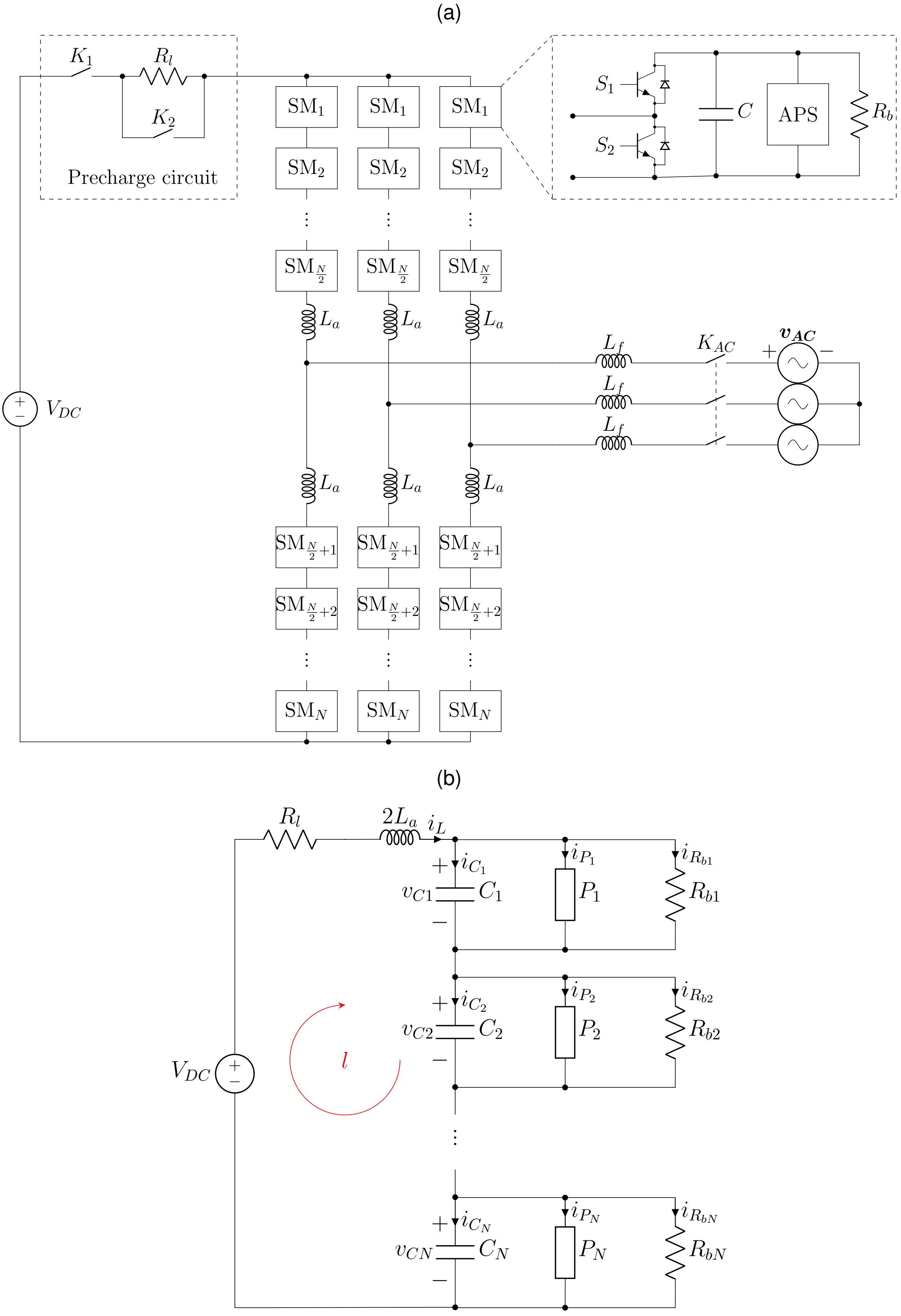

Source – Adapted from Schmidt et al. (2019).

In addition, the model is phenomenological, as it is usual with electric circuits because we know its topology and parameter values. We use Kirchhoff current and voltage laws, together with the voltage-current relations in the components to derive it.

We are specially interested in the capacitor voltages balancing problem and finding out which value of the discharging resistances makes balancing possible and the system operating point stable. The variables of interest are the voltages v_{Ci}[1], since the main control goal is to balance them. Hence, the chosen states are v_{Ci}, that can be grouped in the vector $\boldsymbol{v_C} = [v_{C1}\ v_{C2}\ \dots\ v_{CN}]^T$, and also the current i_L in the equivalent phase inductance. The circuit parameters are V_{DC}, R_l, C_i, and P_i. The resistance R_b can be seen as a design parameter.

We then use the Kirchhoff Currents Law and the voltage-current relations in the circuit components to obtain the model equations. In the i-th SM, for $i \in \{1,2\dots,N\}$ (Figure 4(b)), we have

$$i_L - i_{Ci} - i_{Pi} - i_{Rbi} = 0. \tag{1}$$

Also, using the current-voltage relations in each element we can express the current in each component in terms of the defined states as

$$i_{Ci} = C_i \frac{dv_{Ci}}{dt}, \tag{2}$$

$$i_{Pi} = \frac{P_i}{v_{Ci}}, \tag{3}$$

$$i_{Rbi} = \frac{v_{Ci}}{R_{bi}}. \tag{4}$$

For i_L, we have, applying the Kirchhoff voltage law in the loop l of Figure 4:

$$V_{DC} - R_l i_L - \sum_{k=1}^{N} v_{Ck} - 2L_a \frac{di_L}{dt} = 0. \tag{5}$$

Considering a relatively small arm inductance ($L_a \to 0$), an assumption that is valid in practical applications (ZYGMANOWSKI; GRZESIK; NALEPA, 2013), in (5), we can approximate the inductor current as

$$i_L \approx \frac{V_{DC} - \sum_{k=1}^{N} v_{Ck}}{R_l}. \tag{6}$$

The equivalent circuit, neglecting the effect of L_a can be seen in Figure 5. Replacing (6), (2), (3) and (4) in (1), we have the model equations:

$$\frac{dv_{C_i}}{dt} = \frac{1}{C_i}\left(\frac{V_{DC} - \sum_{k=1}^{N} v_{Ck}}{R_l} - \frac{P_i}{v_{C_i}} - \frac{v_{C_i}}{R_{bi}}\right). \tag{7}$$

for $i \in \{1,\ 2,\ \dots,\ N\}$.

---

[1] In order to simplify the notation, we omit the variable dependencies like in: $v_{C1} = v_{C1}(t)$.

Figure 5 – MMC precharge equivalent circuit neglecting the effect of L_a

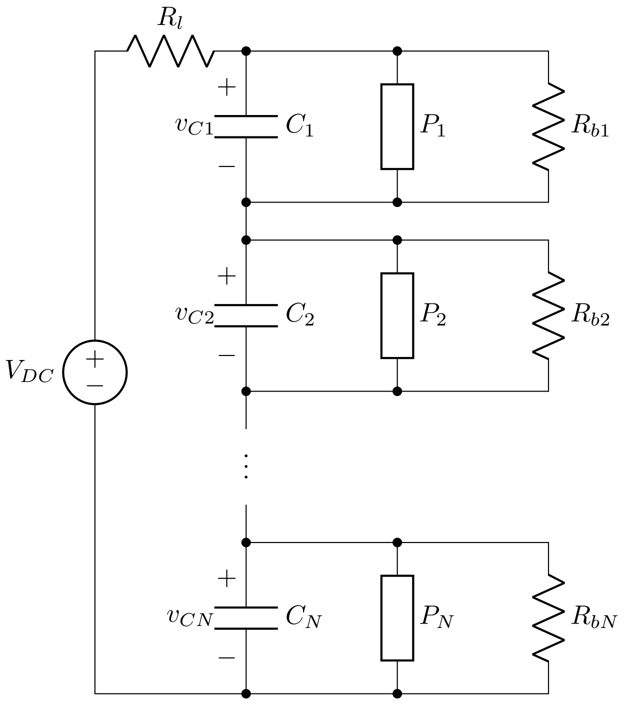

Source – Own elaboration.

2.2 EXTENDED MODEL - STAGE 1 AND 2 OF THE PRECHARGE OPERATION

Now we propose a model for the stage uncontrolled and inactive of the precharge operation. In this stage, not all the APS are turned on. In fact, in the prototype which this work is based on, each one just turns on when their respective voltage v_{Ci} has reached a minimum level V_{Cmin} - which is a parameter dependent on the circuit hardware design. We then propose a model for systems that fits this situation. We also consider the dynamics of the APS turning on to be much faster than the balancing dynamics, so we consider it ideally to be instantaneous. So, the power consumed by the i-th CPL that models the APS is:

$$P_{APSi} = \begin{cases} 0, \text{ if } v_{Ci} < V_{Cmin} \\ P_i, \text{ if } v_{Ci} > V_{Cmin} \end{cases} .$$

There is a discontinuity in this power, dependent on voltage. That can be expressed in terms of the sgn function:

$$\begin{aligned} P_{APSi} &= w_i P_i \\ w_i &= \frac{1+sgn(h_i)}{2} \\ h_i &= v_{Ci} - V_{Cmin} \end{aligned}$$

The same method used to obtain the model (7), but now considering P_{APSi} as the power consumed in the i-th APS, is used to derive the extended one:

$$\frac{dv_{C_i}}{dt} = \frac{1}{C_i}\left(\frac{V_{DC}-\sum_{k=1}^{N} v_{Ck}}{R_l} - \frac{P_i}{v_{Ci}}w_i - \frac{v_{C_i}}{R_i}\right), \tag{8}$$

$$w_i = \frac{1+sgn(h_i)}{2} \tag{9}$$

with,

$$h_i = v_{Ci} - V_{Cmin}, \tag{10}$$

in which v_{Ci} are the state variables and V_{DC}, R_l, C_i, P_i, V_{Cmin} and R_{bi} are the parameters. This model represents a PWS system since there is discontinuity in the power terms. Note that equation (10) stands for multiple switching boundaries since $i \in \{1, 2, \dots, N\}$ and thus the switching law operates with multiple boundaries $h_i = 0$.

2.3 SIMULATION EXAMPLE: APPROXIMATION OF INDUCTOR CURRENT

In this section we show an example illustrating the approximation of the inductor current, by neglecting the efect of the arm inductances. Two models for the same system were simulated, one taking into account the approximation, using (8), (9) and (10), and another one replacing (8) by

$$\frac{dv_{Ci}}{dt} = \frac{1}{C_i}\left(i_L - \frac{P_i}{v_{Ci}}w_i - \frac{v_{Ci}}{R_{bi}}\right), \tag{11}$$

$$\frac{di_L}{dt} = \frac{1}{2L_a}\left(V_{DC} - \sum_{k=1}^{N} v_{Ck} - Ri_L\right), \tag{12}$$

thus taking into account the effects of L_a. The variables v_{Ci} and i_L are the states and V_{DC}, R_l, L_a, C_i, P_i, V_{Cmin} and R_{bi} are the parameters. For simulation, we consider as it is in the nominal case, that is $C_1 = C_2 = C$, $P_1 = P_2 = P$ and $R_{b1} = R_{b2} = R_b$.

The parameter values used for simulation are shown in Table 1. They were based on a prototype he have in our facilities. The number of submodules per phase $N = 2$ is used for simplicity. In the next chapter, the advantages of using $N = 2$ regardless of real systems having a typically a greater number of SMs are explained.

Table 1 – Circuit parameters for comparison between models with and without L_a effect.

N	V_{DC}[V]	$R_l[\Omega]$	C[mF]	P[W]	V_{Cmin}[V]	$R_b[\Omega]$	L_a[mH]
2	150	100	2,82	10	50	250	1

Source – Own elaboration.

Figure 6 – Comparison between models - with i_L and with approximated i_L

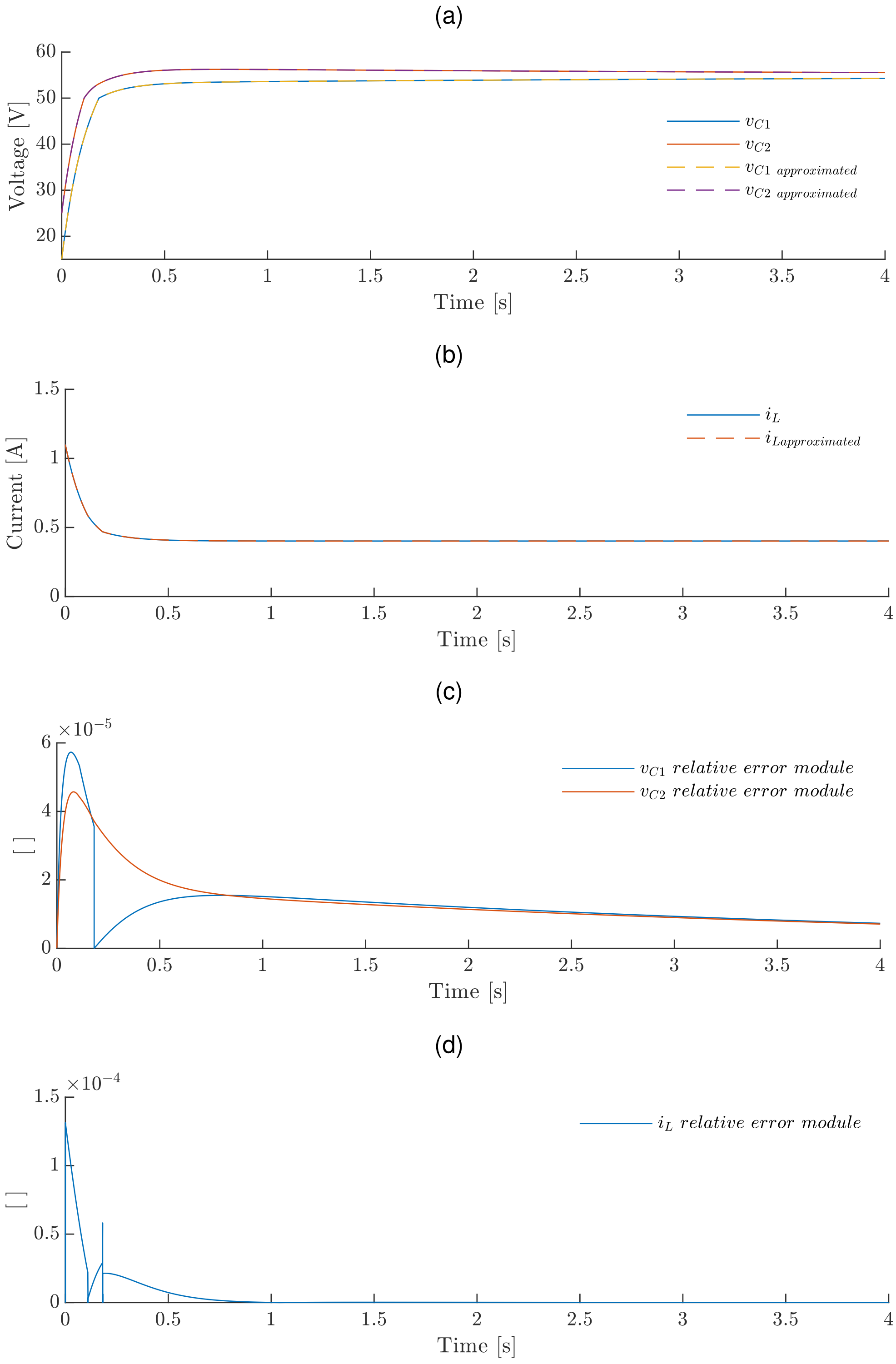

Source – Own elaboration.

In Figure 6, we can see the comparison between the two models. In 6(a) we observe both models time responses for the same initial condition. The model taking into account the effects of L_a responses are represented in solid lines, meanwhile the model neglecting these effects are represented in dashed lines. No significant difference can be seen between these responses. In Figure 6(b), it is depicted the inductor current and the approximation in (6), respectively in solid and dashed lines. Again, there is no visible difference at this scale.

The magnitude of the error between the two models can be seen in Figure 6 (c) and (d). These are respectively, the voltage and current time responses relative errors between the two models. For these tipical parameters, the relative error is in the order of 10^{-5} for the states and 10^{-4} for the inductor current. This exemplifies that the effect of the arm inductance can be neglected if L_a is relatively small.

2.4 SUMMARY

In this chapter we have seen:

- The modeling of the stage 1 and 2 of the precharge of the MMC for the proposed passive balancing solution.
- The model is phenomenological, instantaneous, and nonlinear.
- We assumed the arm inductances are low enough so that their dynamics can be neglected, because the voltage drop in it is relatively much lower than the others. This is true in practical applications.
- We modeled stage 1 of the precharge, when the APS turn on, considering their dynamics as ideally instantaneous. We consider them relatively much faster than the dynamics of v_{Ci}.
- Stage 1 was included in the model as a disturbance governed by a discontinuity, the sgn function, so the resulting model is a PWS system.

In the next chapter we use this model and qualitative analysis tools in order to better understand the system dynamics.

3 ANALYSIS OF A TWO SUBMODULE SYSTEM DYNAMICS

In this chapter, a simplified system with only two SM is defined based on the PWS model obtained in chapter 2. From this system, conditions for the stability of the operating point are derived and then this result is extend for a general case for a N-SM system. Based on that, we propose first guidelines on the design of R_b. The simplified system is used to obtain simulation results in chapter 4. The guidelines to design R_b are used in chapter 5 to obtain experimental results. The two SM system is further analyzed in 6 to obtain the results about the global stability of its operating point.

In section 3.1, the simplified system is defined. We show that its dynamics are governed by four vector fields and two switching boundaries. These are analyzed in sections 3.2,3.3, 3.4, 3.5, 3.6 and 3.7. For each one of the vector fields, we present the analytical expressions for their nullclines, equilibrium points and, when feasible, the classification and stability of these equilibrium points. For the switching boundaries, we present the tangency points, crossing and sliding regions and corresponding sliding vector fields. In these sliding vector fields, we present the pseudo-equilibrium points and their stability and classification. Part of the analysis was made with the aid of symbolic computation tools.

In the section 3.5 we present the vector field that contains the operating point of the system. Therefore, it is analyzed in more depth. In the secondary section 3.5.1, the result about the stability of the operating point is extended for a system with N SM. Based on that, in the secondary section 3.5.2 we propose first guidelines for the design of R_b. A summary of this chapter is presented in 3.8.

3.1 THE TWO SUBMODULE SYSTEM

In order to facilitate the analysis, we consider first a two dimensional case, that is, the MMC composed by two submodules in one phase leg. In that way we can use the phase plane tool to analyze the system, and the results obtained in this chapter can be simulated and plotted in the phase plane (simulation results are shown in chapter 4), and information and insight about the qualitative behavior of the system can be obtained.

The equations (8-10) for a system with $N=2$ are:

$$\frac{dv_{C1}}{dt} = \frac{1}{C_1}\left(\frac{V_{DC}-(v_{C1}+v_{C2})}{R_l} - \frac{P_1}{v_{C1}}w_1 - \frac{v_{C_1}}{R_{b1}}\right), \tag{13}$$

$$\frac{dv_{C2}}{dt} = \frac{1}{C_2}\left(\frac{V_{DC}-(v_{C1}+v_{C2})}{R_l} - \frac{P_2}{v_{C2}}w_2 - \frac{v_{C_2}}{R_{b2}}\right), \tag{14}$$

$$w_1 = \frac{1+sgn(h_1)}{2}, \tag{15}$$

$$w_2 = \frac{1+sgn(h_2)}{2}, \tag{16}$$

$$h_1 = v_{C1} - V_{Cmin}, \tag{17}$$

$$h_2 = v_{C2} - V_{Cmin}. \tag{18}$$

We analyze the system in the domain $\mathbb{D}$, defined as:

$$\mathbb{D} = \{(v_{C1}, v_{C2}) \in \mathbb{R}^2 : 0 < v_{C1} \leq V_{DC} \text{ and } 0 < v_{C2} \leq V_{DC}\}, \tag{19}$$

since the capacitor voltages are positive and in principle do not surpass V_{DC} in a real system[1]. Because of the sgn function, there are two switching boundaries in the state space, defined as

$$\Sigma_1 = \{(v_{C1}, v_{C2}) \in \mathbb{D} : h_1 = 0\}, \tag{20}$$

$$\Sigma_2 = \{(v_{C1}, v_{C2}) \in \mathbb{D} : h_2 = 0\}. \tag{21}$$

These boundaries divide the phase plane in four regions defined by

$$\mathbb{D}_1 = \{(v_{C1}, v_{C2}) \in \mathbb{D} : h_1 < 0 \text{ and } h_2 < 0\},$$
$$\mathbb{D}_2 = \{(v_{C1}, v_{C2}) \in \mathbb{D} : h_1 < 0 \text{ and } h_2 > 0\},$$
$$\mathbb{D}_3 = \{(v_{C1}, v_{C2}) \in \mathbb{D} : h_1 > 0 \text{ and } h_2 < 0\},$$
$$\mathbb{D}_4 = \{(v_{C1}, v_{C2}) \in \mathbb{D} : h_1 > 0 \text{ and } h_2 > 0\}.$$

In each one of these regions, there is a vector field from (13)-(18) governing the system dynamics, defined as in Figure 7. In that way, we can redefine the system as the

---

[1] In chapter 6, it is proved that the domain $\mathbb{D}$ is positively invariant. That means: any trajectories that start within $\mathbb{D}$, will remain inside it for all positive time. This means that for any initial condition inside $\mathbb{D}$, it is always valid that $0 \leq v_{C1} \leq V_{DC}$, and also $0 \leq v_{C2} \leq V_{DC}$.

equivalent discontinuous piecewise smooth system (DPWS):

$$f = \begin{bmatrix} \dfrac{dv_{C1}}{dt} \\ \dfrac{dv_{C2}}{dt} \end{bmatrix} = \begin{bmatrix} f_1 \\ f_2 \end{bmatrix} = \begin{cases} f^{--}, \text{ if } (v_{C1}, v_{C2}) \in \mathbb{D}_1, \\ f^{-+}, \text{ if } (v_{C1}, v_{C2}) \in \mathbb{D}_2, \\ f^{+-}, \text{ if } (v_{C1}, v_{C2}) \in \mathbb{D}_3, \\ f^{++}, \text{ if } (v_{C1}, v_{C2}) \in \mathbb{D}_4, \end{cases} \tag{22}$$

composed of the vector fields

$$f^{--} = \begin{bmatrix} f_1^- \\ f_2^- \end{bmatrix} = \begin{bmatrix} \dfrac{1}{C_1}\left(\dfrac{V_{DC}-(v_{C1}+v_{C2})}{R} - \dfrac{v_{C1}}{R_{b1}}\right) \\ \dfrac{1}{C_2}\left(\dfrac{V_{DC}-(v_{C1}+v_{C2})}{R} - \dfrac{v_{C2}}{R_{b2}}\right) \end{bmatrix}, \tag{23}$$

$$f^{-+} = \begin{bmatrix} f_1^- \\ f_2^+ \end{bmatrix} = \begin{bmatrix} \dfrac{1}{C_1}\left(\dfrac{V_{DC}-(v_{C1}+v_{C2})}{R} - \dfrac{v_{C1}}{R_{b1}}\right) \\ \dfrac{1}{C_2}\left(\dfrac{V_{DC}-(v_{C1}+v_{C2})}{R} - \dfrac{P_2}{v_{C2}} - \dfrac{v_{C2}}{R_{b2}}\right) \end{bmatrix}, \tag{24}$$

$$f^{+-} = \begin{bmatrix} f_1^+ \\ f_2^- \end{bmatrix} = \begin{bmatrix} \dfrac{1}{C_1}\left(\dfrac{V_{DC}-(v_{C1}+v_{C2})}{R} - \dfrac{P_1}{v_{C1}} - \dfrac{v_{C1}}{R_{b1}}\right) \\ \dfrac{1}{C_2}\left(\dfrac{V_{DC}-(v_{C1}+v_{C2})}{R} - \dfrac{v_{C2}}{R_{b2}}\right) \end{bmatrix}, \tag{25}$$

$$f^{++} = \begin{bmatrix} f_1^+ \\ f_2^+ \end{bmatrix} = \begin{bmatrix} \dfrac{1}{C_1}\left(\dfrac{V_{DC}-(v_{C1}+v_{C2})}{R_l} - \dfrac{P_1}{v_{C1}} - \dfrac{v_{C1}}{R_{b1}}\right) \\ \dfrac{1}{C_2}\left(\dfrac{V_{DC}-(v_{C1}+v_{C2})}{R_l} - \dfrac{P_2}{v_{C2}} - \dfrac{v_{C2}}{R_{b2}}\right) \end{bmatrix}, \tag{26}$$

for $w_1 = w_2 = 0$; $w_1 = 0$ and $w_2 = 1$; $w_1 = 1$ and $w_2 = 0$; $w_1 = w_2 = 1$; respectively. The vector fields can be extended to the switching boundaries by using the Filippov theory (KUZNETSOV; RINALDI; GRAGNANI, 2003).

We begin the analysis by first studying f^{--}, f^{-+}, f^{+-} and f^{++}. We study the null isoclines, equilibrium points and their stability and classification. Then we define the dynamics over Σ_1 and Σ_2 using Fillipov's theory. There we look for sliding regions, tangency points, pseudo equilibrium points and their stability. Here in this chapter, the dynamics of each vector field is studied separately. The interaction between them in f is first addressed in chapter 4 in some simulation results, and then further in chapter 6, where the matter of global stability is discussed.

Figure 7 – Phase Plane Regions and respective governing vector fields for the system (18)-(22)

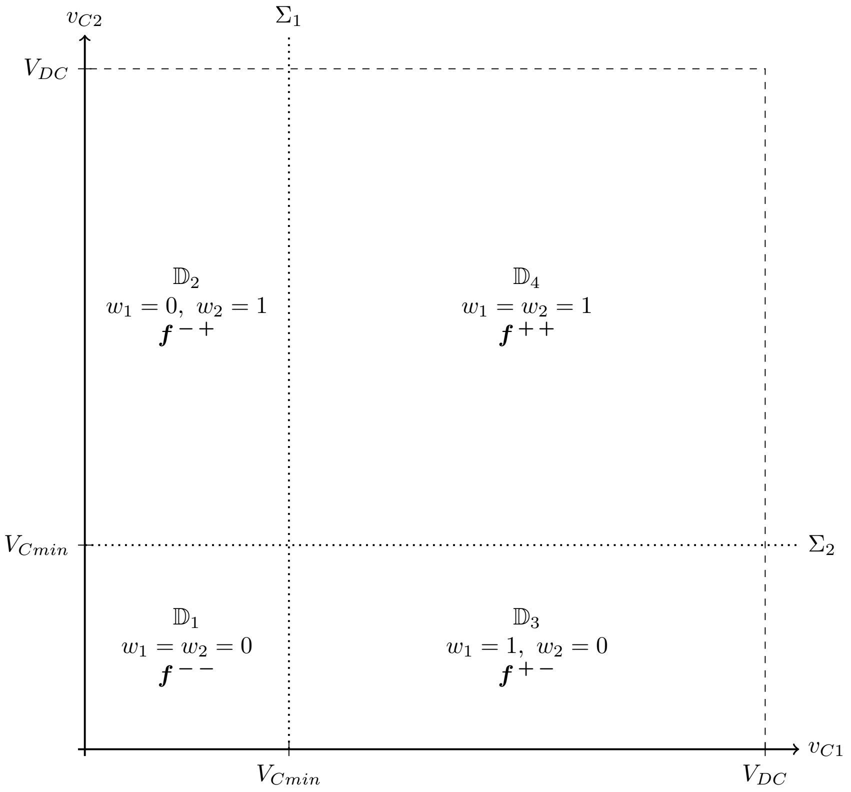

Source – Own Elaboration.

3.2 f^{--} DYNAMICS

The $\boldsymbol{f}^{--}$ field is given by the equation (23), rewritten below:

$$\boldsymbol{f}^{--} = \begin{bmatrix} f_1^- \\ f_2^- \end{bmatrix} = \begin{bmatrix} \dfrac{1}{C_1}\left(\dfrac{V_{DC}-(v_{C1}+v_{C2})}{R_l} - \dfrac{v_{C1}}{R_{b1}}\right) \\ \dfrac{1}{C_2}\left(\dfrac{V_{DC}-(v_{C1}+v_{C2})}{R_l} - \dfrac{v_{C2}}{R_{b2}}\right) \end{bmatrix}.$$

It is important to notice that this is a linear vector field. So there can be only one equilibrium point and its stability properties are global. Its equivalent circuit is shown in Figure 8, and correspond to the case where all the APS are turned off.

Nullclines

The nullclines of $\boldsymbol{f}^{--}$ are $f_1^- = 0$ and $f_2^- = 0$, respectively

$$v_{C2} = V_{DC} - v_{C1}\left(1 + \frac{R_l}{R_{b1}}\right), \tag{27}$$

$$v_{C1} = V_{DC} - v_{C2}\left(1 + \frac{R_l}{R_{b2}}\right). \tag{28}$$

Figure 8 – $\boldsymbol{f}^{--}$ equivalent circuit.

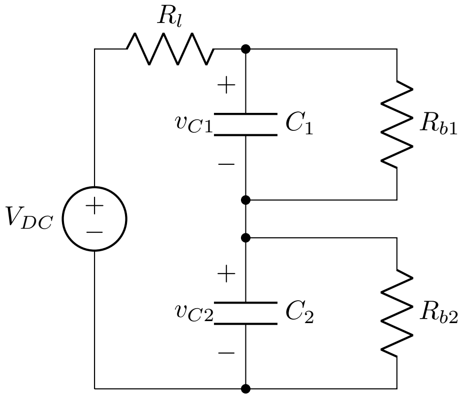

Source – Own Elaboration.

Equilibrium Point

The equilibrium point is given by the intersection of (27) and (28) or yet $\boldsymbol{f}^{--} = \boldsymbol{0}$ [2] which is

$$\boldsymbol{E}^{--} = \left(E_1^{--}, E_2^{--}\right) = \left(\frac{V_{DC}R_{b1}}{R_l + R_{b1} + R_{b2}}, \frac{V_{DC}R_{b2}}{R_l + R_{b1} + R_{b2}}\right). \tag{29}$$

One can see that the equilibrium voltages simply correspond to the voltages in the voltage division circuit of Figure 8.

Stability of the Equilibrium Point

As it can be already expected, $\boldsymbol{E}^{--}$ is globally asymptotically stable. We can verify its stability by calculating the field's Jacobian matrix (denoted by $\boldsymbol{A}^{--}$) in respect to $\boldsymbol{v_C}$ evaluated at the given equilibrium point, and verifying the standard equilibrium points stability conditions for planar (another name for by-dimensional) systems: $det(\boldsymbol{A}^{--}) > 0$ and $tr(\boldsymbol{A}^{--}) < 0$. Then, we get

$$\boldsymbol{A}^{--} = \begin{bmatrix} \dfrac{\partial f_1^-}{\partial v_{C1}} & \dfrac{\partial f_1^-}{\partial v_{C2}} \\ \dfrac{\partial f_2^-}{\partial v_{C1}} & \dfrac{\partial f_2^-}{\partial v_{C2}} \end{bmatrix} = \begin{bmatrix} -\left(\dfrac{1}{R_l} + \dfrac{1}{R_{b1}}\right)\dfrac{1}{C_1} & -\dfrac{1}{R_l C_1} \\ -\dfrac{1}{R_l C_2} & -\left(\dfrac{1}{R_l} + \dfrac{1}{R_{b2}}\right)\dfrac{1}{C_2} \end{bmatrix},$$

whose determinant and trace are

$$det(\boldsymbol{A}^{--}) = \frac{1}{C_1 C_2}\left(\frac{1}{R_l R_{b1}} + \frac{1}{R_l R_{b2}} + \frac{1}{R_{b1} R_{b2}}\right) > 0, \tag{30}$$

$$tr(\boldsymbol{A}^{--}) = -\left(\frac{1}{R_l} + \frac{1}{R_{b1}}\right)\frac{1}{C_1} - \left(\frac{1}{R_l} + \frac{1}{R_{b2}}\right)\frac{1}{C_2} < 0. \tag{31}$$

Since $\boldsymbol{f}^{--} = \boldsymbol{A}^{--}\boldsymbol{v_C}$ and $\boldsymbol{A}^{--}$ has all eigenvalues with negative real part, one concludes that $\boldsymbol{E}^{--}$ is globally asymptotically stable.

---

[2] $\boldsymbol{0}$ is the null vector. In this case, the null vector of dimensions 2×1.

3.3 f^{-+} DYNAMICS

Now we proceed studying the dynamics of $\boldsymbol{f}^{-+}$, which is given by (24):

$$\boldsymbol{f}^{-+} = \begin{bmatrix} f_1^- \\ f_2^+ \end{bmatrix} = \begin{bmatrix} \dfrac{1}{C_1}\left(\dfrac{V_{DC}-(v_{C1}+v_{C2})}{R_l} - \dfrac{v_{C1}}{R_{b1}}\right) \\ \dfrac{1}{C_2}\left(\dfrac{V_{DC}-(v_{C1}+v_{C2})}{R_l} - \dfrac{P_2}{v_{C2}} - \dfrac{v_{C2}}{R_{b2}}\right) \end{bmatrix}.$$

Differently from $\boldsymbol{f}^{--}$, $\boldsymbol{f}^{-+}$ is nonlinear. It corresponds to the case where only one APS is turned on. Its equivalent circuit can be seen in Figure 9.

Figure 9 – $\boldsymbol{f}^{-+}$ equivalent circuit.

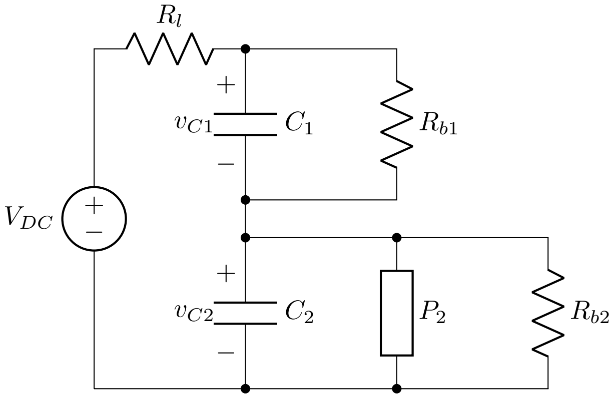

Source – Own Elaboration.

Nullclines

The nullcline $f_1^- = 0$ (27), present in $\boldsymbol{f}^{--}$ is also present in $\boldsymbol{f}^{-+}$. We rewrite it here as a reminder:

$$v_{C2} = V_{DC} - v_{C1}\left(1 + \frac{R_l}{R_{b1}}\right).$$

The other one is $f_2^+ = 0$, or

$$v_{C1} = V_{DC} - v_{C2}\left(1 + \frac{R_l}{R_{b2}}\right) - \frac{P_2 R_l}{v_{C2}}. \tag{32}$$

Equilibrium Points

The equilibrium points of $\boldsymbol{f}^{-+}$ are given by the intersection of $f_1^- = 0$ and $f_2^+ = 0$, the same as $\boldsymbol{f}^{-+} = \boldsymbol{0}$. There are two equilibrium points:

$$\boldsymbol{E}_1^{-+} = \left(E_{11}^{-+}, E_{12}^{-+},\right) \tag{33}$$

with

$$E_{11}^{-+} = \frac{2R_{b1}(R_l+R_{b1})V_{DC}+R_{b1}R_{b2}V_{DC}+R_{b1}\sqrt{R_{b2}^2V_{DC}^2-4P_2R_{b2}(R_l+R_{b1})(R_l+R_{b1}+R_{b2})}}{2(R_l+R_{b1})(R_l+R_{b1}+R_{b2})}, \tag{34}$$

$$E_{12}^{-+} = \frac{R_{b2}V_{DC}-\sqrt{R_{b2}^2V_{DC}^2-4P_2R_{b2}(R_l+R_{b1})(R_{+}R_{b1}+R_{b2})}}{2(R_l+R_{b1}+R_{b2})}, \tag{35}$$

and

$$\boldsymbol{E_2^{-+}} = \left(E_{21}^{-+}, E_{22}^{-+}\right), \tag{36}$$

with

$$E_{21}^{-+} = \frac{2R_{b1}(R_l+R_{b1})V_{DC}+R_{b1}R_{b2}V_{DC}-R_{b1}\sqrt{R_{b2}^2V_{DC}^2-4P_2R_{b2}(R_l+R_{b1})(R_l+R_{b1}+R_{b2})}}{2(R_l+R_{b1})(R_l+R_{b1}+R_{b2})}, \tag{37}$$

$$E_{22}^{-+} = \frac{R_{b2}V_{DC}+\sqrt{R_{b2}^2V_{DC}^2-4P_2R_{b2}(R_l+R_{b1})(R_l+R_{b1}+R_{b2})}}{2(R_l+R_{b1}+R_{b2})}. \tag{38}$$

The condition that ensures that the components of both of these equilibria are indeed real numbers is:

$$P_2 \leq \frac{R_{b2}V_{DC}^2}{4(R_l+R_{b1})(R_l+R_{b1}+R_{b2})} = P_{2c}^{-+}. \tag{39}$$

That is, if $P_2 < P_{2c}^{-+}$, both equilibrium points exist. If it reaches the critical value $P_2 = P_{2c}^{-+}$, they collide, and if $P_2 > P_{2c}^{-+}$, they cease to exist. That characterizes a bifurcation, and as it has co-dimension one – that means only one parameter is varied in order to produce it. In bi-dimensional systems, the bifurcation that is characterized for the collision and disappearance of equilibrium points is a saddle-node bifurcation.

Stability of the Equilibrium Points

We can check the stability of $\boldsymbol{E_1^{-+}}$ and $\boldsymbol{E_2^{-+}}$ in case they exist (are real). The equilibrium point $\boldsymbol{E_1^{-+}}$ is unstable, and a saddle point. An classification of $\boldsymbol{E_1^{-+}}$ stability by analytical proof could not be made. However, the first steps are written here and the rest may be completed in future works. Also, an numeric approach for practical problems is suggested.

We begin verifying the stability of $\boldsymbol{E_1^{-+}}$. For that, we compute the Jacobian matrix of $\boldsymbol{f^{-+}}$ in respect to $\boldsymbol{v_C}$, which is

$$\boldsymbol{A^{-+}} = \begin{bmatrix} \frac{1}{C_1}\left(-\frac{1}{R_l}-\frac{1}{R_{b1}}\right) & -\frac{1}{R_lC_1} \\ -\frac{1}{R_lC_2} & \frac{1}{C_2}\left(-\frac{1}{R_l}+\frac{P_2}{v_{C2}^2}-\frac{1}{R_{b2}}\right) \end{bmatrix}.$$

Then we calculate

$$det(\boldsymbol{A}^{-+})\big|_{v_C=\boldsymbol{E}_1^{-+}} = \\ \frac{4P_2R_{b2}(R_l+R_{b1})(R_l+R_{b1}+R_{b2})-R_{b2}V_{DC}^2-V_{DC}\sqrt{R_{b2}^2V_{DC}^2-4P_2(R_l+R_{b1})(R_l+R_{b1}+R_{b2})}}{2R_lC_1C_2P_2R_{b1}R_{b2}(R_{b1}+R_{b2})}.$$

If $\boldsymbol{E}_1^{-+}$ exists, the condition (39) is satisfied. That implies

$$4P_2(R_l+R_{b1})(R_l+R_{b1}+R_{b2})-R_{b2}V_{DC}^2 \leq 0,$$
$$-V_{DC}\sqrt{R_{b2}^2V_{DC}^2-4P_2(R_l+R_{b1})(R_l+R_{b1}+R_{b2})} \leq 0,$$

so

$$det(\boldsymbol{A}^{-+})\big|_{v_C=\boldsymbol{E}_1^{-+}} \leq 0.$$

If $P_2 = P_{2c}^{-+}$, $det(\boldsymbol{A}^{-+})\big|_{v_C=\boldsymbol{E}_1^{-+}} = 0$ and $\boldsymbol{E}_1^{-+}$ is non hyperbolic (and coliding with $\boldsymbol{E}_2^{-+}$). If $P_2 < P_{2c}^{-+}$, $det(\boldsymbol{A}^{-+})\big|_{v_C=\boldsymbol{E}_1^{-+}} < 0$ and therefore $\boldsymbol{E}_1^{-+}$ is unstable and a saddle point.

Now, regarding the stability of $\boldsymbol{E}_2^{-+}$, it is shown here that $det(\boldsymbol{A}^{-+})\big|_{v_C=\boldsymbol{E}_2^{-+}} \geq 0$, but no conclusion about the sign of $tr(\boldsymbol{A}^{-+})\big|_{v_C=\boldsymbol{E}_2^{-+}}$. If it exists, condition (39) is satisfied. We have

$$det(\boldsymbol{A}^{-+})\big|_{v_C=\boldsymbol{E}_2^{-+}} = \\ \frac{4P_2(R_l+R_{b1})(R_l+R_{b1}+R_{b2})-R_{b2}V_{DC}^2+V_{DC}\sqrt{R_{b2}^2V_{DC}^2-4P_2R_{b2}(R_l+R_{b1})(R_l+R_{b1}+R_{b2})}}{2C_1C_2P_2R_lR_{b1}R_{b2}(R_l+R_{b1})}.$$

We show that

$$4P_2(R_l+R_{b1})(R_l+R_{b1}+R_{b2})-R_{b2}V_{DC}^2+V_{DC}\sqrt{R_{b2}^2V_{DC}^2-4P_2R_{b2}(R_l+R_{b1})(R_l+R_{b1}+R_{b2})} > 0. \tag{40}$$

Using the substitution

$$a = R_{b2}^2V_{DC}^2-4P_2R_{b2}(R_l+R_{b1})(R_l+R_{b1}+R_{b2}) \tag{41}$$

in (40), we have

$$-\frac{a}{R_{b2}}+V_{DC}\sqrt{a} > 0,$$

that can be manipulated into

$$R_{b2}V_{DC} > \sqrt{a}. \tag{42}$$

Now, replacing (41) again in (42) we have

$$R_{b2}V_{DC} > \sqrt{R_{b2}^2V_{DC}^2-4P_2R_{b2}(R_{b1}+R_{b2})(R_l+R_{b1}+R_{b2})}.$$

Therefore, $det(\boldsymbol{A}^{-+})\big|_{\boldsymbol{v_C}=\boldsymbol{E_2^{-+}}} > 0$ if $P_2 \le P_{2c}^{-+}$ and $det(\boldsymbol{A}^{-+})\big|_{\boldsymbol{v_C}=\boldsymbol{E_2^{-+}}} = 0$ if $P_2 = P_{2c}^{-+}$.

The other condition for the stability of $\boldsymbol{E_2^{-+}}$ is

$$
\begin{aligned}
tr(\boldsymbol{A}^{-+})\big|_{\boldsymbol{v_C}=\boldsymbol{E_2^{-+}}} = &-\frac{1}{C_1}\left(\frac{1}{R_l}+\frac{1}{R_{b1}}\right)\\
&-\frac{1}{C_2}\left(\frac{1}{R_l}+\frac{1}{R_{b2}}-\frac{4P_2(R_l+R_{b1}+R_{b2})^2}{\left(-R_{b2}V_{DC}+\sqrt{R_{b2}^2V_{DC}^2-4P_2R_{b2}(R_l+R_{b1})(R_l+R_{b1}+R_{b2})}\right)^2}\right)<0.
\end{aligned}
$$

In this context, it remains to prove that

$$
\frac{1}{R_l}+\frac{1}{R_{b2}}-\frac{4P_2(R_l+R_{b1}+R_{b2})^2}{\left(-R_{b2}V_{DC}+\sqrt{R_{b2}^2V_{DC}^2-4P_2R_{b2}(R+R_{b1})(R_l+R_{b1}+R_{b2})}\right)^2}>0.
$$

Due to the system's own complexity, there is an inherent difficulty in proving analytically the stability for a general case. In chapter 4, for parameter values based on a real MMC prototype, the equilibrium points $\boldsymbol{E_2^{-+}}$ and $\boldsymbol{E_3^{-+}}$ actually do not exist. As future works, a normalized model may be used to calculate numerically the stability of these points for parameter values in ranges that are typically used in practical applications. The use of the normalized model can reduce complexity by reducing the parameter number, and also permits to obtain more general results.

3.4 f^{+-} DYNAMICS

The field $\boldsymbol{f}^{+-}$ is

$$
\boldsymbol{f}^{+-}=\begin{bmatrix} f_1^+\\ f_2^- \end{bmatrix}=\begin{bmatrix} \dfrac{1}{C_1}\left(\dfrac{V_{DC}-(v_{C1}+v_{C2})}{R_l}-\dfrac{P_1}{v_{C1}}-\dfrac{v_{C1}}{R_{b1}}\right)\\ \dfrac{1}{C_2}\left(\dfrac{V_{DC}-(v_{C1}+v_{C2})}{R_l}-\dfrac{v_{C2}}{R_{b2}}\right) \end{bmatrix}.
$$

The field $\boldsymbol{f}^{+-}$ has the same dynamic characteristics of $\boldsymbol{f}^{-+}$, rewritten below:

$$
\boldsymbol{f}^{-+}=\begin{bmatrix} f_1^-\\ f_2^+ \end{bmatrix}=\begin{bmatrix} \dfrac{1}{C_1}\left(\dfrac{V_{DC}-(v_{C1}+v_{C2})}{R_l}-\dfrac{v_{C1}}{R_{b1}}\right)\\ \dfrac{1}{C_2}\left(\dfrac{V_{DC}-(v_{C1}+v_{C2})}{R_l}-\dfrac{P_2}{v_{C2}}-\dfrac{v_{C2}}{R_{b2}}\right) \end{bmatrix}.
$$

This can be seen examining both equivalent circuits (Figure 10), which have the same topology. Also, the fields $\boldsymbol{f}^{+-}$ and $\boldsymbol{f}^{-+}$ have the same expression, except for a permutation in the states and parameters. Because of that, the dynamics of $\boldsymbol{f}^{-+}$ are omitted here for the sake of simplicity and to avoid repetitions.

Figure 10 – $\boldsymbol{f}^{+-}$ equivalent circuit (a) and $\boldsymbol{f}^{-+}$ equivalent circuit (b). Both have the same topology.

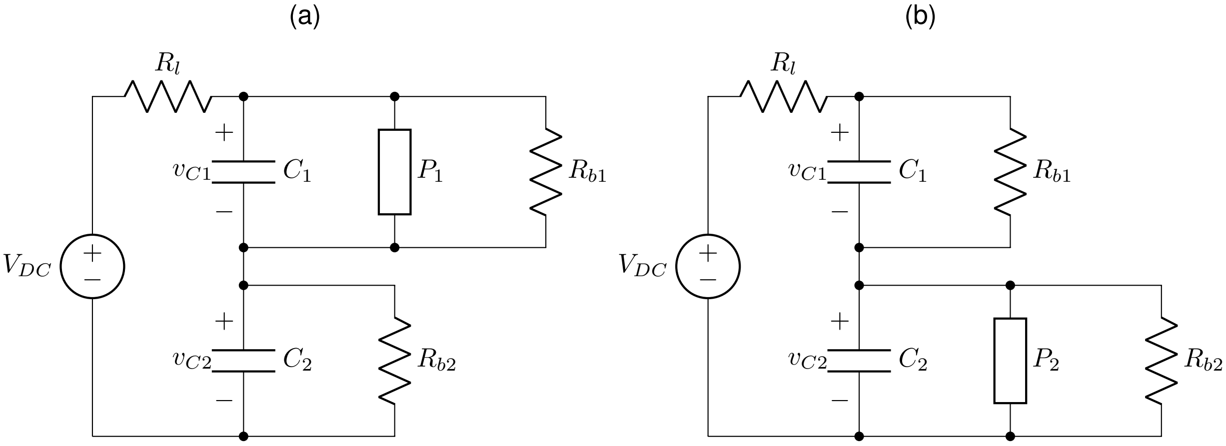

Source – Own Elaboration.

3.5 f^{++} DYNAMICS

The $\boldsymbol{f}^{++}$ field is, as defined in (26):

$$\boldsymbol{f}^{++} = \begin{bmatrix} f_1^+ \\ f_2^+ \end{bmatrix} = \begin{bmatrix} \dfrac{1}{C_1}\left(\dfrac{V_{DC}-(v_{C1}+v_{C2})}{R_l} - \dfrac{P_1}{v_{C1}} - \dfrac{v_{C1}}{R_{b1}}\right) \\ \dfrac{1}{C_2}\left(\dfrac{V_{DC}-(v_{C1}+v_{C2})}{R_l} - \dfrac{P_2}{v_{C2}} - \dfrac{v_{C2}}{R_{b2}}\right) \end{bmatrix}.$$

It corresponds to the precharge uncontrolled and active stage, in which all the APS are turned on (Figure 11).

Figure 11 – $\boldsymbol{f}^{++}$ equivalent circuit.

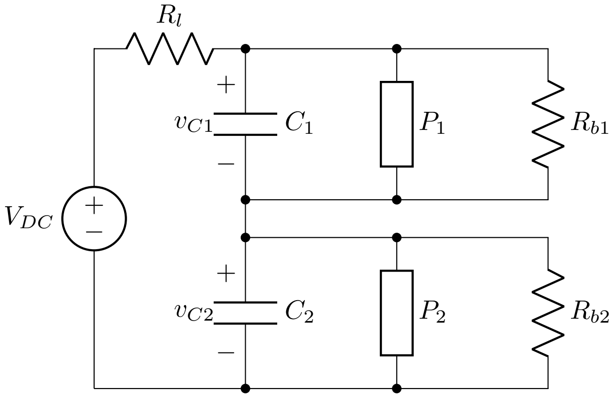

Source – Own Elaboration.

Nullclines

The null isoclines of $\boldsymbol{f}^{++}$ are $f_1{}^+ = 0$ and $f_2{}^+ = 0$, given by (32), respectively

$$v_{C2} = V_{DC} - v_{C1}\left(1 + \frac{R_l}{R_{b1}}\right) - \frac{P_1 R_l}{v_{C1}}, \tag{43}$$

$$v_{C1} = V_{DC} - v_{C2}\left(1 + \frac{R_l}{R_{b2}}\right) - \frac{P_2 R_l}{v_{C2}}.$$

Equilibrium Points

The equilibrium points are given by the intersection of (43) and (32) or solution of $\boldsymbol{f}^{++} = \boldsymbol{0}$ for $\boldsymbol{v_C}$. As these equilibrium coordinates are more dificult to compute in this case, we assume the simplifying hipothesis:

$$P_1 = P_2 = P, \tag{44}$$

$$R_{b1} = R_{b2} = R_b, \tag{45}$$

which happens in the nominal case. For these simplifications, the equilibrium points coordinates are

$$\boldsymbol{E_1^{++}} = \left(E_{11}^{++}, E_{12}^{++}\right) = \left(\frac{R_b V_{DC} + \sqrt{R_b^2 V_{DC}^2 - 4PR_l R_b(R_l + 2R_b)}}{2(R_l + 2R_b)}, \frac{R_b V_{DC} + \sqrt{R_b^2 V_{DC}^2 - 4PR_l R_b(R_l + 2R_b)}}{2(R_l + 2R_b)}\right), \tag{46}$$

$$\boldsymbol{E_2^{++}} = \left(E_{21}^{++}, E_{22}^{++}\right) = \left(\frac{R_b V_{DC} - \sqrt{R_b^2 V_{DC}^2 - 4PR_b(R_l + R_b)^2}}{2(R_l + R_b)}, \frac{R_b V_{DC} + \sqrt{R_b^2 V_{DC}^2 - 4PR_b(R_l + R_b)^2}}{2(R_l + R_b)}\right), \tag{47}$$

$$\boldsymbol{E_3^{++}} = \left(E_{31}^{++}, E_{32}^{++}\right) = \left(\frac{R_b V_{DC} + \sqrt{R_b^2 V_{DC}^2 - 4PR_b(R_l + R_b)^2}}{2(R_l + R_b)}, \frac{R_b V_{DC} - \sqrt{R_b^2 V_{DC}^2 - 4PR_b(R_l + R_b)^2}}{2(R_l + R_b)}\right), \tag{48}$$

$$\boldsymbol{E_4^{++}} = \left(E_{41}^{++}, E_{42}^{++}\right) = \left(\frac{R_b V_{DC} - \sqrt{R_b^2 V_{DC}^2 - 4PR_l R_b(R_l + 2R_b)}}{2(R_l + 2R_b)}, \frac{R_b V_{DC} - \sqrt{R_b^2 V_{DC}^2 - 4PR_l R_b(R_l + 2R_b)}}{2(R_l + 2R_b)}\right). \tag{49}$$

For the equilibrium points $\boldsymbol{E_1^{++}}$ and $\boldsymbol{E_4^{++}}$, $v_{C1} = v_{C2}$, meaning the capacitor voltages are balanced in them. In fact, $\boldsymbol{E_1^{++}}$ is the desired operating point, as its voltages are closer to E/N, which is ideal voltage in the uncontrolled stage of the precharge. The existence conditions for $\boldsymbol{E_1^{++}}$ and $\boldsymbol{E_4^{++}}$ are the same:

$$P \leq \frac{R_b V_{DC}^2}{4R_l(R_l + 2R_b)} = P_{c14}^{++}. \tag{50}$$

That is, if $P < P_{c14}^{++}$, they both exist with different coordinates, if $P = P_{c14}^{++}$, they both collide and if $P > P_{c14}^{++}$, both cease to exist. This characterizes a bifurcation. That means also, that if P is relatively large enough, it is impossible for this system to reach the desired operating point.

Now there is also the pair $\boldsymbol{E}_{\mathbf{2}}^{++}$ and $\boldsymbol{E}_{\mathbf{3}}^{++}$. One can notice that the voltages are unbalanced in both of them. Also, $\boldsymbol{E}_{\mathbf{21}}^{++} = \boldsymbol{E}_{\mathbf{32}}^{++}$ and $\boldsymbol{E}_{\mathbf{22}}^{++} = \boldsymbol{E}_{\mathbf{31}}^{++}$. Regarding their existence condition, we have

$$P \leq \frac{V_{DC}^2 R_b}{4(R_l + R_b)^2} = P_{c23}^{++}. \tag{51}$$

If $P < P_{c23}^{++}$, they both exist with distinct coordinates. If $P = P_{c23}^{++}$ they collide together with $\boldsymbol{E}_{\mathbf{1}}^{++}$, at

$$\boldsymbol{v}_{\boldsymbol{C}} = \left(\frac{R_b V_{DC}}{2(R_l + R_b)}, \frac{R_b V_{DC}}{2(R_l + R_b)} \right),$$

and if $P > P_{c23}^{++}$, they cease to exist. The collision of three natural equilibrium points in a planar system, caused by the variation of only one parameter, characterizes a pitchfork bifurcation.

Stability and Classification of the Equilibrium Points

We are especially interested in verify the conditions of stability of the operating point $\boldsymbol{E}_{\mathbf{1}}^{++}$. Assuming (44-45) case, the stability of $\boldsymbol{E}_{\mathbf{2}}^{++}$ and $\boldsymbol{E}_{\mathbf{3}}^{++}$ are linked to it - these points are related in a pitchfork bifurcation. The analytical proof of neither the stability of $\boldsymbol{E}_{\mathbf{4}}^{++}$ nor the other ones could be done analytically for the general case, and are left for future work. As suggested for $\boldsymbol{E}_{\mathbf{2}}^{-+}$, these may be done numerically for a parameter range typically used in practical applications.

We begin by calculating the Jacobian Matrix of $\boldsymbol{f}^{++}$ in respect to $\boldsymbol{v}_{\boldsymbol{C}}$, that is

$$\boldsymbol{A}^{++} = \begin{bmatrix} \frac{1}{C_1}\left(\frac{P}{v_{C1}^2} - \frac{1}{R_l} - \frac{1}{R_b}\right) & -\frac{1}{R_l C_1} \\ -\frac{1}{R_l C_2} & \frac{1}{C_2}\left(\frac{P}{v_{C2}^2} - \frac{1}{R_l} - \frac{1}{R_b}\right) \end{bmatrix}.$$

We know that, in $\boldsymbol{E}_{\mathbf{1}}^{++}$ as well as in $\boldsymbol{E}_{\mathbf{4}}^{++}$ the voltages are balanced. We then rewrite the coordinates of $\boldsymbol{E}_{\mathbf{1}}^{++}$ as

$$\boldsymbol{E}_{\mathbf{1}}^{++} = (V_{Cb}, V_{Cb}).$$

As $\boldsymbol{A}^{++}$ is symmetric, both of its eigenvalues are real. The following stability conditions come from both eigenvalues of $\boldsymbol{A}^{++}|_{\boldsymbol{v}_{\boldsymbol{C}} = \boldsymbol{E}_{\mathbf{1}}^{++}}$ being negative.

We can calculate the eigenvalues of such a matrix knowing that a matrix $\boldsymbol{M}$ in such a form

$$m_{ij} = \begin{cases} D & \text{, if } i = j \\ O & \text{, if } i \neq j \end{cases} \tag{52}$$

has the following eigenvalues[3]

$$\lambda_1 = \lambda_2 = \cdots = \lambda_{N-1} = D - O \tag{53}$$

$$\lambda_N = D + (N-1)O. \tag{54}$$

Therefore the stability conditions are

$$\frac{V_{Cb}^2}{R_b} > P, \tag{55}$$

$$\frac{V_{Cb}^2}{R_b} > P - \frac{V_{Cb}^2}{R_l}. \tag{56}$$

As (55) is more restrictive than (56) regarding maximum value of R_c, (55) is a sufficient condition needed to delimit this value. This is the condition of local stability of the system operating point and it means that the power consumed in R_c must be greater than P, for $\boldsymbol{E_1^{++}}$ to be stable.

As for the stability of $\boldsymbol{E_2^{++}}$ and $\boldsymbol{E_3^{++}}$, it is known that they exist with distinct coordinates if $P < P_{c23}^{++}$. Also, that they have a relation with $\boldsymbol{E_1^{++}}$ stability through a pitchfork bifurcation. When (55) is satisfied, P is also lower than a critical value so to say. That indicates that, if $\boldsymbol{E_1^{++}}$ is stable, both $\boldsymbol{E_2^{++}}$ and $\boldsymbol{E_3^{++}}$ exist and are unstable. When $\boldsymbol{E_1^{++}}$ is unstable, $\boldsymbol{E_2^{++}}$ and $\boldsymbol{E_3^{++}}$ do not exist.

3.5.1 Local Stability of Operating point - Extending Results For a N-SM System

The local stability conditions for the operating point can be generalized for the case with an arbitrary number N of SMs. We begin by retrieving the model equation for the uncontrolled and active stage of the precharge in (7), rewritten below:

$$\frac{dv_{C_i}}{dt} = \frac{1}{C_i}\left(\frac{V_{DC} - \sum_{k=1}^{N} v_{Ck}}{R_l} - \frac{P_i}{v_{Ci}} - \frac{v_{Ci}}{R_{bi}}\right),$$

with $i \in \{1, 2, \ldots, N\}$.

We also consider the simplifying hipothesis

$$C_1 = C_2 = \cdots = C_N = C, \tag{57}$$

$$P_1 = P_2 = \cdots = P_N = P, \tag{58}$$

$$R_{b1} = R_{b2} = \cdots = R_{bN} = R_b. \tag{59}$$

Substituting (57)-(59) in (7), we have

$$\frac{dv_{Ci}}{dt} = \frac{1}{C}\left(\frac{V_{DC} - \sum_{k=1}^{N} v_{Ck}}{R} - \frac{P}{v_{Ci}} - \frac{v_{Ci}}{R_b}\right), \tag{60}$$

with $i \in \{1, 2, \ldots, N\}$.

---

[3] These eigenvalues were calculated for values of N, such that $N \geq 2$, with the aid of a symbolic computation tool.

Now, we calculate the Jacobian matrix of (60), which is given by

$$\boldsymbol{A} = \begin{bmatrix} a_{11} & a_{12} & \cdots & a_{1N} \\ a_{21} & a_{22} & \cdots & a_{2N} \\ \vdots & \vdots & \ddots & \vdots \\ a_{N1} & a_{N2} & \cdots & a_{NN} \end{bmatrix},$$

whose elements are defined as

$$a_{ij} = \begin{cases} \frac{1}{C}\left(-\frac{1}{R_l} + \frac{P}{v_{Ci}^2} - \frac{1}{R_b}\right) & \text{, if } i = j, \\ -\frac{1}{R_l C} & \text{, if } i \neq j, \end{cases}$$

with $\{i,j\} \in \{1, 2, \cdots, N\}$.

Assuming that, calculating the eigenvalues λ_n of $\boldsymbol{A}$ at the operating equilibrium point where $v_{C1} = v_{C2} = \cdots = v_{CN} = V_{Cb}$ in the same way it was calculated in the previous case by (52-54), we have

$$\lambda_1 = \lambda_2 = \cdots = \lambda_{N-1} = \frac{1}{C}\left(\frac{P}{V_{Cb}^2} - \frac{1}{R_b}\right),$$
$$\lambda_N = \frac{1}{C}\left(-\frac{N}{R_l} + \frac{P}{V_{Cb}^2} - \frac{1}{R_b}\right).$$

from which it is possible to establish the following stability conditions:

$$\frac{V_{Cb}^2}{R_b} > P, \tag{61}$$
$$\frac{V_{Cb}^2}{R_b} > P - \frac{N V_{Cb}^2}{R_l}. \tag{62}$$

As we are interested in the maximum value of R_b, the condition (61) is more restrictive than (62). The condition (61) is the same for two or for an arbitrary number N of SM per phase.

3.5.2 Guidelines for the Design of R_b

Now that we've seen the local stability conditions for the operating point, we have some first guidelines for the design of R_b. In order to properly function, the system has to satisfy (61). As this means the power consumed in R_b must be greater than P, we can define the design parameter γ as the ratio

$$\gamma = \frac{\left(\frac{V_{Cb}^2}{R_b}\right)}{P}. \tag{63}$$

So that with $\gamma > 1$, $\boldsymbol{E}_{\mathbf{1}}^{++}$ is locally stable. With a chosen γ value, it is possible to calculate the corresponding R_b value. We first compute V_{Cb} as a function of γ, and then solve (63) for R_b.

For that, we begin considering the circuit in Figure 12 in steady state, at $\boldsymbol{E}_{\mathbf{1}}^{++}$. The total power consumed in the SM is

$$NV_{Cb}i_{R_l} = N(P + \gamma P), \tag{64}$$

with γP being the power consumed in R_b. We have two unknown variables, i_{Rl} and V_{Cb}, therefore we add another equation in order to solve for V_{Cb}. We also have, at the loop l (Figure 12):

$$V_{DC} - R_l i_{Rl} - NV_{Cb} = 0. \tag{65}$$

Solving the equation system (64)-(65), we have the possible solutions for V_{Cb}

$$V_{Cb} = \frac{V_{DC} \pm \sqrt{V_{DC}^2 - 4R_l(1+\gamma)PN}}{2N}.$$

The value of V_{Cb} in $\boldsymbol{E}_{\mathbf{1}}^{++}$ is the term with positive square root:

$$V_{Cb} = \frac{V_{DC} + \sqrt{V_{DC}^2 - 4R_l(1+\gamma)PN}}{2N}. \tag{66}$$

In that way, we calculate R_b from (63)

$$R_b = \frac{V_{Cb}^2}{\gamma P}. \tag{67}$$

From (66), assuming that $\boldsymbol{E}_{\mathbf{1}}^{++}$ exists, we can calculate the maximum possible γ value:

$$\gamma < \frac{V_{DC}^2}{4NPR_l} - 1 = \gamma_{max}. \tag{68}$$

So, the range of γ values that one can choose, in order to guarantee local stability of the operating point must satisfy, according to (61), (63) and (68) is

$$1 < \gamma < \gamma_{max}. \tag{69}$$

In addition, for (69) to be feasible, it is necessary that $\gamma_{max} > 1$, which means, from (68):

$$\frac{V_{DC}^2}{8NR_l} > P, \tag{70}$$

otherwise, it is simply not possible for the system to function as desired.

With that, we have the first guidelines for the design of R_b. One can choose γ within the range in (69) and then calculate the corresponding R_b. It is important to state that, a local stable operating point is necessary, but not sufficient in order to make the system to function as desired. The attraction domain of $E_{\mathbf{1}}^{++}$ must be large enough so that trajectories starting with initial conditions $\boldsymbol{v_{C0}} = \mathbf{0}$ must end up in this domain as they reach $\mathbb{D}_4$. In chapter 4 the relation between R_b variation and size of the attraction domain is investigated by using numerical simulations. It shows there is a trade-off between the power consumed in R_b and size of the attraction domain. For now, we have already a range from which to choose and guarantee local stability. The safest measure, when ensuring stability is desired, is to choose R_b correspondent to γ_{max}, if this is feasible.

Figure 12 – MMC precharge equivalent circuit assuming (57)-(59).

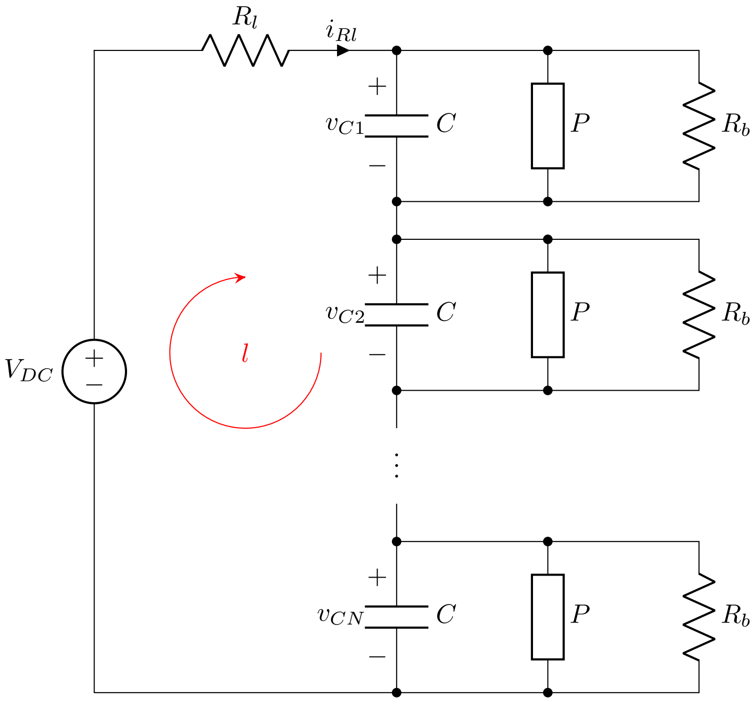

Source – Own elaboration.

3.6 DYNAMICS IN Σ_1

In this section, we analyze the dynamics in Σ_1. We look for sliding segments, crossing segments and tangency points in it. The dynamics of f^{--}, f^{-+}, f^{+-} and f^{++} are properly extended to Σ_1 using the Filippov theory. In the vector fields defined in Σ_1, we look for pseudo-equilibrium points and study their stability.

Sliding or Crossing Segments and Tangency Points

To find whether there are sliding segments and respective extreme tangency points, we begin by calculating the Lie derivatives[4] of the four fields. The switching boundary Σ_1, defined in (20), is determined by the scalar function h_1, defined in (17) and rewritten below:

$$h_1 = v_{C1} - V_{Cmin},$$

with respective gradient vector

$$\nabla h_1 = \begin{bmatrix} \dfrac{\partial h_1}{\partial v_{C1}} \\ \dfrac{\partial h_1}{\partial v_{C2}} \end{bmatrix} = \begin{bmatrix} 1 \\ 0 \end{bmatrix}.$$

The fields on the left of Σ_1 are these boundaries are $\boldsymbol{f}^{--}$ and $\boldsymbol{f}^{-+}$, and on the right of it are $\boldsymbol{f}^{+-}$ and $\boldsymbol{f}^{++}$, as defined in (23-26):

$$\boldsymbol{f}^{--} = \begin{bmatrix} f_1^- \\ f_2^- \end{bmatrix} = \begin{bmatrix} \dfrac{1}{C_1}\left(\dfrac{V_{DC}-(v_{C1}+v_{C2})}{R_l} - \dfrac{v_{C1}}{R_{b1}}\right) \\ \dfrac{1}{C_2}\left(\dfrac{V_{DC}-(v_{C1}+v_{C2})}{R_l} - \dfrac{v_{C2}}{R_{b2}}\right), \end{bmatrix}$$

$$\boldsymbol{f}^{-+} = \begin{bmatrix} f_1^- \\ f_2^+ \end{bmatrix} = \begin{bmatrix} \dfrac{1}{C_1}\left(\dfrac{V_{DC}-(v_{C1}+v_{C2})}{R_l} - \dfrac{v_{C1}}{R_{b1}}\right) \\ \dfrac{1}{C_2}\left(\dfrac{V_{DC}-(v_{C1}+v_{C2})}{R_l} - \dfrac{P_2}{v_{C2}} - \dfrac{v_{C2}}{R_{b2}}\right) \end{bmatrix},$$

$$\boldsymbol{f}^{+-} = \begin{bmatrix} f_1^+ \\ f_2^- \end{bmatrix} = \begin{bmatrix} \dfrac{1}{C_1}\left(\dfrac{V_{DC}-(v_{C1}+v_{C2})}{R_l} - \dfrac{P_1}{v_{C1}} - \dfrac{v_{C1}}{R_{b1}}\right) \\ \dfrac{1}{C_2}\left(\dfrac{V_{DC}-(v_{C1}+v_{C2})}{R_l} - \dfrac{v_{C2}}{R_{b2}}\right) \end{bmatrix},$$

$$\boldsymbol{f}^{++} = \begin{bmatrix} f_1^+ \\ f_2^+ \end{bmatrix} = \begin{bmatrix} \dfrac{1}{C_1}\left(\dfrac{V_{DC}-(v_{C1}+v_{C2})}{R_l} - \dfrac{P_1}{v_{C1}} - \dfrac{v_{C1}}{R_{b1}}\right) \\ \dfrac{1}{C_2}\left(\dfrac{V_{DC}-(v_{C1}+v_{C2})}{R_l} - \dfrac{P_2}{v_{C2}} - \dfrac{v_{C2}}{R_{b2}}\right) \end{bmatrix}.$$

For these, we have the Lie derivatives in Σ_1, where $v_{C1} = V_{Cmin}$:

$$L_{f^{--}}h_1 = L_{f^{-+}}h_1 = \frac{1}{C_1}\left(\frac{V_{DC}-(V_{Cmin}+v_{C2})}{R_l} - \frac{V_{Cmin}}{R_{b1}}\right), \tag{71}$$

$$L_{f^{+-}}h_1 = L_{f^{++}}h_1 = \frac{1}{C_1}\left(\frac{V_{DC}-(V_{Cmin}+v_{C2})}{R_l} - \frac{P_1}{V_{Cmin}} - \frac{V_{Cmin}}{R_{b1}}\right). \tag{72}$$

---

[4] The first order Lie derivative of a scalar function h in respect to a vector field f is calculated as: $L_f h = \langle \nabla h, f \rangle$, in which ∇h is the gradient vector of h, and $\langle , \rangle$ is the scalar product operation.

We test for example if there are attractive sliding segments and where they are. The attractive sliding conditions are:

$$\begin{aligned} L_{f^{--}}h_1 &= L_{f^{-+}}h_1 > 0, \\ L_{f^{+-}}h_1 &= L_{f^{++}}h_1 < 0, \end{aligned}$$

respectively

$$\begin{aligned} v_{C2} &< V_{DC} - \frac{V_{Cmin}(R_l + R_{b1})}{R_{b1}}, \\ v_{C2} &> V_{DC} - \frac{P_1 R_l}{V_{Cmin}} - \frac{V_{Cmin}(R_l + R_{b1})}{R_{b1}}. \end{aligned}$$

In that way, we can define the sliding segment Σ_1^{as} as

$$\Sigma_1^{as} = \left\{ (v_{C1}, v_{C2}) \in \Sigma_1 : V_{DC} - \frac{P_1 R_l}{V_{Cmin}} - \frac{V_{Cmin}(R_l + R_{b1})}{R_{b1}} < v_{C2} < V_{DC} - \frac{V_{Cmin}(R_l + R_{b1})}{R_{b1}} \right\}. \tag{73}$$

Now, the extremes of Σ_1^{as} are tangency points in Σ_1, given by

$$\boldsymbol{T_1^-} = \left(T_{11}^-, T_{12}^-\right) = \left(V_{Cmin}, V_{DC} - \frac{V_{Cmin}(R_l + R_{b1})}{R_{b1}} \right), \tag{74}$$

$$\boldsymbol{T_1^+} = \left(T_{11}^+, T_{12}^+\right) = \left(V_{Cmin}, V_{DC} - \frac{P_1 R_l}{V_{Cmin}} - \frac{V_{Cmin}(R_l + R_{b1})}{R_{b1}} \right), \tag{75}$$

with $\boldsymbol{T_1^-}$ being the tangency point of f^{--} or f^{-+} and $\boldsymbol{T_1^+}$ being the tangency point of f^{+-} or f^{++}. Note that $T_{12}^- > T_{12}^+$. All of these elements are ilustrated in Figure 13.

Other than that in Σ_1, if $v_{C2} > T_{12}^-$, $L_{f^{--}}h_1 = L_{f^{-+}}h_1 < 0$ and $L_{f^{+-}}h_1 = L_{f^{++}}h_1 < 0$, then it is a crossing region from $\mathbb{D}_4$ to $\mathbb{D}_2$, or, from $\mathbb{D}_3$ to $\mathbb{D}_1$. And if $v_{C2} < T_{12}^+$, it is a crossing region from $\mathbb{D}_1$ to $\mathbb{D}_3$ or from $\mathbb{D}_2$ to $\mathbb{D}_4$.

Figure 13 – Regions and tangency points in Σ_1. Vector field $\frac{dv_{C1}}{dt}$ components are drawn in gray.

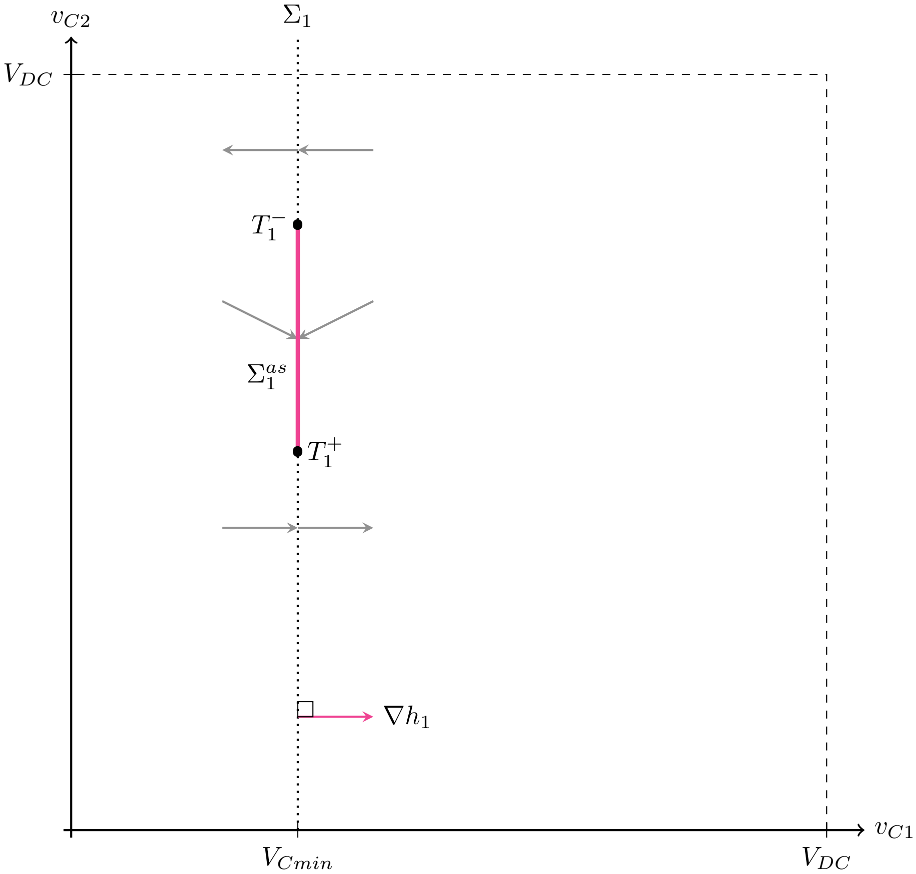

Source – Own Elaboration.

Sliding Vector Fields

We can extend the dynamics of f^{--}, f^{-+}, f^{+-} and f^{++} to Σ_1 using Filipov's theory. According to Kuznetsov, Rinaldi, and Gragnani (2003), the sliding dynamics field of a field f^s in the boundary $h = 0$ between two fields f^- and f^+ can be calculated acording to the expression:

$$f^s = \frac{\langle \nabla h, f^+ \rangle f^- - \langle \nabla h, f^- \rangle f^+}{\langle \nabla h, f^+ - f^- \rangle}.$$

In our case, in order to calculate the dynamics in Σ_1, we divide it in two regions:

$$\Sigma_1^- = \{(v_{C1}, v_{C2}) \in \Sigma_1 : h_2 < 0\},$$
$$\Sigma_1^+ = \{(v_{C1}, v_{C2}) \in \Sigma_1 : h_2 > 0\},$$

and calculate a sliding vector field for each one, respectively $\boldsymbol{f}^{s\mathbf{1}-}$ and $\boldsymbol{f}^{s\mathbf{1}+}$. The field $\boldsymbol{f}^{s\mathbf{1}-}$ is given by

$$\begin{aligned}
\boldsymbol{f}^{s\mathbf{1}-} &= \frac{\langle \nabla h_1, \boldsymbol{f}^{+-} \rangle \boldsymbol{f}^{--} - \langle \nabla h_1, \boldsymbol{f}^{--} \rangle \boldsymbol{f}^{+-}}{\langle \nabla h_1, \boldsymbol{f}^{+-} - \boldsymbol{f}^{--} \rangle} \\
&= \begin{bmatrix} f_1^{s1-} \\ f_2^{s1-} \end{bmatrix} = \begin{bmatrix} 0 \\ \dfrac{1}{C_2} \left(\dfrac{V_{DC} - (V_{Cmin} + v_{C2})}{R_l} - \dfrac{v_{C2}}{R_{b2}} \right) \end{bmatrix}.
\end{aligned}$$

Note that there are no dynamics in $\dfrac{dv_{C1}}{dt}$, and in the $\dfrac{dv_{C2}}{dt}$ component, they are equal to f_2^-. Analogously, $\boldsymbol{f}_{\mathbf{1}}^{s+}$ is given by:

$$\begin{aligned}
\boldsymbol{f}^{s\mathbf{1}+} &= \frac{\langle \nabla h_1, \boldsymbol{f}^{++} \rangle \boldsymbol{f}^{-+} - \langle \nabla h_1, \boldsymbol{f}^{-+} \rangle \boldsymbol{f}^{++}}{\langle \nabla h_1, \boldsymbol{f}^{++} - \boldsymbol{f}^{-+} \rangle} \\
&= \begin{bmatrix} f_1^{s1+} \\ f_2^{s1+} \end{bmatrix} = \begin{bmatrix} 0 \\ \dfrac{1}{C_2} \left(\dfrac{V_{DC} - (V_{Cmin} + v_{C2})}{R_l} - \dfrac{P_2}{v_{C2}} - \dfrac{v_{C2}}{R_{b2}} \right) \end{bmatrix}.
\end{aligned}$$

In a similar way, the $\dfrac{dv_{C1}}{dt}$ component is null, and $\dfrac{dv_{C2}}{dt} = f_2^+$.

Pseudo-Equilibrium Points

The pseudo-equilibrium points in Σ_1 occur where $\boldsymbol{f}^{s\mathbf{1}-} = \mathbf{0}$ and also where $\boldsymbol{f}^{s\mathbf{1}+} = \mathbf{0}$. As $\dfrac{dv_{C1}}{dt} = 0$ for both of them, they coincide with the geometrical locus corresponding to the intersection of the nullclines $f_2^- = 0$ and $f_2^+ = 0$ with Σ_1.

For $\boldsymbol{f}^{s\mathbf{1}-}$, we have only one solution for $\boldsymbol{f}^{s\mathbf{1}-} = \mathbf{0}$, that is the pseudo-equilbrium point

$$\boldsymbol{E}^{s\mathbf{1}-} = \left(E_{11}^{s1-}, E_{12}^{s1-} \right) = \left(V_{Cmin}, \frac{R_{b2} (V_{DC} - V_{Cmin})}{R_l + R_{b2}} \right).$$

Now, for $\boldsymbol{f}^{s\mathbf{1}+} = \mathbf{0}$, we have two solutions: the pseudo-equilibrium points

$$\begin{aligned}
\boldsymbol{E}_{\mathbf{1}}^{s\mathbf{1}+} &= \left(E_{11}^{s1+}, E_{12}^{s1+} \right) = \left(V_{Cmin}, \frac{R_{b2} (V_{DC} - V_{Cmin}) - \sqrt{R_{b2}^2 (V_{DC} - V_{Cmin})^2 - 4 P_2 R_l R_{b2} (R_l + R_{b2})}}{2 (R_l + R_{b2})} \right), \\
\boldsymbol{E}_{\mathbf{2}}^{s\mathbf{1}+} &= \left(E_{21}^{s1+}, E_{22}^{s1+} \right) = \left(V_{Cmin}, \frac{R_{b2} (V_{DC} - V_{Cmin}) + \sqrt{R_{b2}^2 (V_{DC} - V_{Cmin})^2 - 4 P_2 R_l R_{b2} (R_l + R_{b2})}}{2 (R_l + R_{b2})} \right). \quad (76)
\end{aligned}$$

Note that $E_{12}^{s1-} \geq E_{22}^{s1+} \geq E_{12}^{s1+}$. Also, we have an existence condition for $\boldsymbol{E}_{\mathbf{1}}^{s\mathbf{1}+}$ and $\boldsymbol{E}_{\mathbf{2}}^{s\mathbf{1}+}$, that can be expressed as

$$P_2 \leq \frac{R_{b2} (V_{DC} - V_{Cmin})^2}{4 R_l (R_l + R_{b2})} = P_{2c}^{s1+}.$$

If $P_2 < P_{2c}^{s1+}$, both exist and $E_{22}^{s1+} > E_{12}^{s1+}$. If $P_2 = P_{2c}^{s1+}$, both pseudo-equilibrium points collide, and for $P_2 < P_{2c}^{s1+}$, they cease to exist.

Stability of Pseudo-Equilibrium Points

We can check the stability of the pseudo-equilibrium points in Σ_1 as it is done in one-dimensional systems. In $\boldsymbol{f}^{s\mathbf{1}-}$, for $\boldsymbol{E}^{s\mathbf{1}-}$, we have

$$\left.\frac{\partial f_2^{s1-}}{\partial v_{C2}}\right|_{v_C=\boldsymbol{E}^{s\mathbf{1}-}} = -\frac{R_l+R_{b2}}{C_2R_lR_{b2}} < 0.$$

So $\boldsymbol{E}^{s\mathbf{1}-}$ is stable, and can be classified as a stable node, since it is in an attractive sliding region. As this not necessarily coincides with the desired operation point, it is undesirable that the system trajectory converge to this point, in case it is real.

Now, for the $\boldsymbol{f}^{s\mathbf{1}+}$ field, we can check the stability of $\boldsymbol{E}_{\mathbf{1}}^{s\mathbf{1}+}$. We prove that it is unstable. We have in this case

$$\left.\frac{\partial f_2^{s1+}}{\partial v_{C2}}\right|_{v_C=\boldsymbol{E}^{s\mathbf{1}-}} =$$

$$-\frac{(V_{Cmin}-V_{DC})\left(\sqrt{R_{b2}^2(V_{DC}-V_{Cmin})^2-4P_2R_l(R_l+R_{b2})}+R_{b2}(V_{DC}-V_{Cmin})\right)+4P_2R_l(R_l+R_{b2})}{2C_2P_2R_l^2R_{b2}} > 0.$$

That is equivalent to:

$$\frac{(V_{DC}-V_{Cmin})\sqrt{R_{b2}^2(V_{DC}-V_{Cmin})^2-4P_2R_l(R_l+R_{b2})}+R_{b2}(V_{DC}-V_{Cmin})^2}{4R_l(R_l+R_{b2})} > P_2,$$

which is true, so $\boldsymbol{E}_{\mathbf{1}}^{s\mathbf{1}+}$ is unstable, assuming that $P_2 < P_{2c}^{s1+}$, or $\boldsymbol{E}_{\mathbf{1}}^{s\mathbf{1}+}$ if and $\boldsymbol{E}_{\mathbf{2}}^{s\mathbf{1}+}$ exist with distinct coordinates.

Finally, we test if $\boldsymbol{E}_{\mathbf{2}}^{s\mathbf{1}+}$ is stable. We prove that it is stable, that is

$$\left.\frac{\partial f_2^{s1+}}{\partial v_{C2}}\right|_{v_C=\boldsymbol{E}_{\mathbf{2}}^{s\mathbf{1}+}} = \left.\frac{P_2R_lR_{b2}-(R_{b2}+R_l)v_{C2}^2}{C_2R_lR_{b2}v_{C2}^2}\right|_{v_C=\boldsymbol{E}_{\mathbf{2}}^{s\mathbf{1}+}} < 0,$$

which is equivalent to

$$P_2 < \left.\frac{R_l+R_{b2}}{R_lR_{b2}}v_{C2}^2\right|_{v_C=\boldsymbol{E}_{\mathbf{2}}^{s\mathbf{1}+}}.$$

Replacing (76), we have

$$P_2 < \frac{R_{b2}(V_{DC}-V_{Cmin})^2+(V_{DC}-V_{Cmin})\sqrt{R_{b2}^2(V_{DC}-V_{Cmin})^2-4P_2R_lR_{b2}(R_l+R_{b2})}}{2R_l(R_l+R_{b2})} - P_2,$$

which is true, if $P_2 < P_{2c}^{s1+}$. Therefore, if $\boldsymbol{E}_{\mathbf{1}}^{s\mathbf{1}+}$ and $\boldsymbol{E}_{\mathbf{2}}^{s\mathbf{1}+}$ exist with distinct coordinates, $\boldsymbol{E}_{\mathbf{2}}^{s\mathbf{1}+}$ is stable.

As both pseudo-equilibrium points are in an attractive sliding region, we can classify $\boldsymbol{E}_{\mathbf{1}}^{s\mathbf{1}+}$ as a pseudo-saddle equilibrium point and $\boldsymbol{E}_{\mathbf{2}}^{s\mathbf{1}+}$ as a pseudo-node. When $P_2 < P_{2c}^{s1+}$, these points collide, and when $P_2 > P_{2c}^{s1+}$, they cease to exist. This characterizes a pseudo-saddle-node bifurcation in Σ_1.

3.7 DYNAMICS IN Σ_2

The set Σ_2 presents the same elements and subsets of Σ_1. In the particular case which $P_1 = P_2 = P$ and $C_1 = C_2 = C$, such elements and subsets are disposed symmetrically to the ones in Σ_1, in relation to the line $v_{C1} = v_{C2}$. Besides, the sliding dynamics in Σ_2 has the same qualitative characteristics of the sliding dynamics in Σ_1, studied in the previous section. Therefore, for the sake of simplicity, they are omitted here. That concludes the matter of dynamics in Σ_2 in this chapter, and also of all the fields in $\mathbb{D}$.

3.8 SUMMARY

In this chapter we have seen:

- The dynamics of a two submodule system was studied, for matters of simplicity. This helps to obtain insight about the system dynamics, because the phase plane tool can be used for analyzing them.
- There are dynamics in four different fields: f^{--}, which corresponds to a system with no APS turned on; f^{-+} and f^{+-}, which corresponds to a system with one APS turned on; and f^{++}, with corresponds to the system with all (two) APS turned on. Each of these was studied separately.
- In addition to these, in the switching boundaries Σ_1 and Σ_2 in between those fields, there are also sliding modes f^{s1-}, f^{s1+}, f^{s2-} and f^{s2+}.
- The dynamics studied included nullclines, equilibrium points, their classification and stability; and for the sliding modes: sliding regions, tangency points and pseudo-equilibrium points. For some fields, the presence of bifurcation was detected.
- Regarding the dynamics in each field, we have:
  - In f^{--}, there is one equilibrium, globally asymptotically stable.
  - In f^{-+} and f^{+-}, there is a saddle point and another point whose stability could not be analytically proved for the general case. This can be made in a numerical approach in future works, by using parameter values typically used in practical applications.
  - In f^{++}, there are four equilibrium points, calculated assuming a simplifying hypothesis, that $P_1 = P_2 = P$ and $R_{b1} = R_{b2} = R_b$ (this occurs in the nominal case). One of them is the operating point where $v_{C1} = v_{C2} = V_{Cb}$, that can be stable node under a condition, explained better in the next bullet point.

    Two other equilibrium points, with symmetry in relation to the straight line $v_{C1} = v_{C2}$ are present. Depending on the parameter values, these two collide with the operating point and then can cease to exist. This is an indicative of a pitchfork bifurcation. The last equilibrium point also satisfies $v_{C1} = v_{C2} = V_{Cb}$, but it is closer to the origin. The stability of these three points was not proved analytically for the general case, and can be made using a numerical approach using parameter values typically used in practical applications. This is left for future works.

  - In $\boldsymbol{f}^{s\mathbf{1}-}$ and $\boldsymbol{f}^{s\mathbf{2}-}$, there is one pseudo-node in each.
  - In $\boldsymbol{f}^{s\mathbf{1}+}$ and $\boldsymbol{f}^{s\mathbf{2}+}$, there is a pseudo-saddle and a pseudo-node in each. Also, in both of them, it is possible to have a pseudo-saddle-node bifurcation.

- Regarding the stability of the operating point, conditions for local stability of a system with two SM were obtained and then the results were extended for a system with an arbitrary number of SM.
  - This extends the work from (LUO; CAO, et al., 2016), that has proven this condition for a system with one SM only.
  - The condition is that the power consumption in R_b must be greater than P.
  - This condition is not a natural choice when R_b is only a bleeder resistance, intended just for discharging the capacitors when the MMC is turned off.

- Based on that, the parameter γ was defined by the ratio between these two powers. Its possible range was calculated, and also how to calculate R_b from a chosen γ within this range.

In the next chapter, we run simulations of vector fields, phase portrait and time responses of $\boldsymbol{f}^{--}$, $\boldsymbol{f}^{-+}$, and $\boldsymbol{f}^{++}$. Also, the sliding regions and tangency points in Σ_1 and Σ_2, vector field and phase portrait of $\boldsymbol{f}$. We also study the dependence of the parametetric variation in the system stability and operation.

4 SIMULATION RESULTS

In this chapter we show simulations of the two SM system from chapter 3. The parameter values used are based on a prototype from which we made the experiments presented in chapter 5. The results exposed here also help to clarify the analysis made in chapter 6.

We show the simulation results for the nominal case, in which the SM parameter have equal values, in section 4.1. The analysis of influence of parametric variation is exhibited in section 4.2. For the nominal case, we have simulated the fields f^{--}, f^{-+}, f^{++} and f from the previous chapter, respectively in the secondary sections 4.1.1, 4.1.2, 4.1.3 and 4.1.4. We have simulated the vector field, phase portrait, sliding dynamics (when present) and time responses for each one of these fields.

In the cases of parametric variations, we have analyzed the influences of R_b, C_i and V_{Cmin} variation, respectively in the secondary sections 4.2.1, 4.2.2 and 4.2.3. As the design of R_b is one of the main issues of the conducted research, the variation of this parameter is analyzed in more depth.

In the tertiary section 4.2.1.1, we present the f^{++} field for the case in which the operating equilibrium point is unstable. Then, in the section 4.2.1.2, the influence of R_b variation in the operating equilibrium point attraction domain is analyzed in f^{++}. In the section 4.2.1.2 we present a bifurcation diagram of f^{++} in dependence with R_b and in section 4.2.1.3 we present a locally stable operating equilibrium point case. The section 4.3 is a summary of this chapter.

4.1 NOMINAL CASE

The parameter values choice was based on a real prototype we have in our facilities at Federal University of Santa Catarina at the Institute of Power Electronics - the power electronics institute inside the electrical engineering department. These results were obtaining designing R_b value in order to guarantee a stable equilibrium operation point. The resistance R_b was designed so that the power consumed in it is approximately 120% of the power P consumed in one APS when it is active. In other words, for $\gamma = 1,2$. The nominal case is stable, with all capacitance values the same. (Table 2) From here on, it is assumed $C_1 = C_2 = C$, $P_1 = P_2 = P$ and $R_{b1} = R_{b2} = R_b$ unless stated otherwise.

For each possible stage of the circuit (no power load, or one power load, or both active), the system vector field, phase portrait and some representative time responses were simulated. After that, the global system, that included all four fields and boundaries, is simulated. For the global case, the sliding regions over the boundaries were also illustrated.

Table 2 – Circuit parameters for simulation of the nominal case with stable operation equilibrium point. The resistance R_b is dimensioned so that $\gamma = 1,20$

N	V_{DC}[V]	$R_l[\Omega]$	C[mF]	P[W]	V_{Cmin}[V]	$R_b[\Omega]$
2	150	100	2,82	10	50	250

Source – Own Elaboration.

4.1.1 f_{--} field

The first simulated field is the $\boldsymbol{f}^{--}$ field. It corresponds to the system with no active power loads. As a matter of fact, this circuit is very simple, linear, and corresponds to a voltage divisor with two connected capacitors. As the system is linear, it has only one equilibrium point (as seen in previous subsection) (Figure 14). In Figure 14 we can see the nullclines $f_1^- = 0$ and $f_2^- = 0$ that divide the vector field in four main regions... each one has a predominant direction in which the vector field points to. From left to $f_1^- = 0$ the field points to the right, and for right it points to the left. At the intersection of the nullclines, there is the system equilibrium point $\boldsymbol{f}$.

Figure 14 – Vector field $\boldsymbol{f}^{--}$

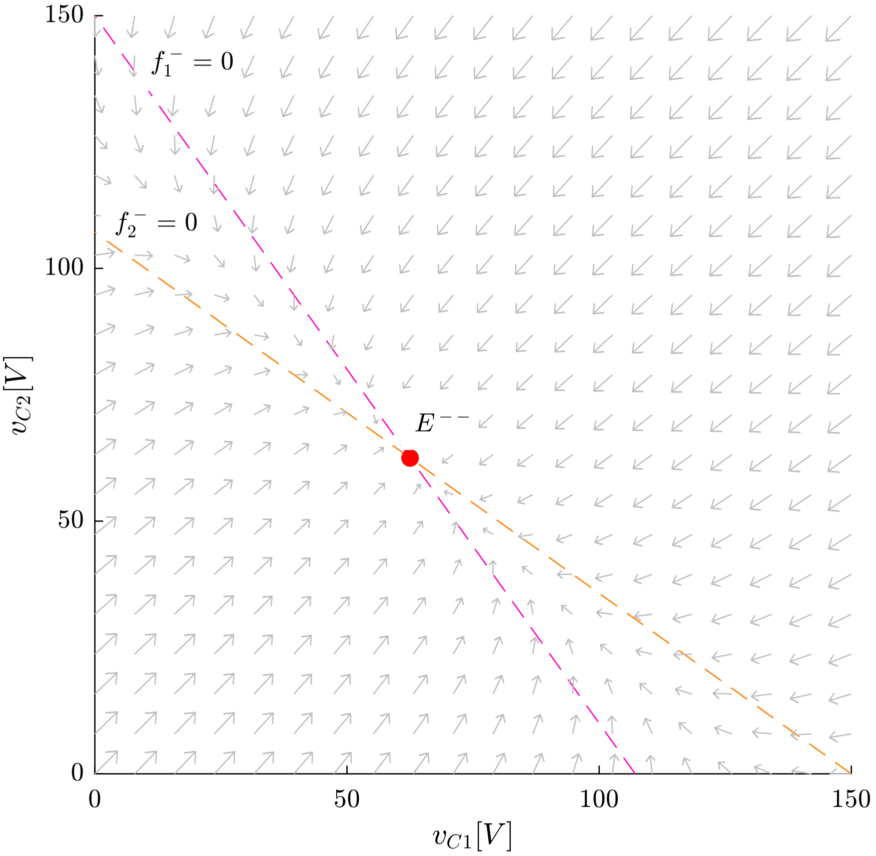

Source – Own elaboration.

The coordinates, eigenvalues and eigenvectors of $\boldsymbol{E}^{--}$ can be seen in Table 3. As seen in the theory subsection, the equilibrium is stable. Its eigenvalues have both a negative real part, so it is a stable node. As this field corresponds to a linear system, it is globally stable. We can see that in all the regions, the vector field points in the direction of this point.

The eigenvectors $\boldsymbol{v1}$ and $\boldsymbol{v2}$ (Table 3) in this point are aligned to two main directions. The vector $\boldsymbol{v1}$ is perpendicular and points towards to the direction of $v_{C1} + v_{C2} = V_{DC}$. That corresponds to the geometric place where the sum of the capacitor voltages is balanced with the voltage source V_{DC}. The vector $\boldsymbol{v_2}$ is perpendicular and points to $v_{C1} = v_{C2}$, which corresponds to the situation where the capacitors are balanced. Also the eigenvalue λ_1 associated with $\boldsymbol{v_1}$ is about six times greater than λ_2 associated with v_2. That means, for this parameter set, that the system approximately balances the sum of the capacitors with the voltage source V_{DC} about six times faster than the time it takes to balance v_{C1} and v_{C2}. That phenomen can be seen observing the system trajectories in its phase portrait (Figure 15).

Figure 15 – Phase portrait of $\boldsymbol{f}^{--}$

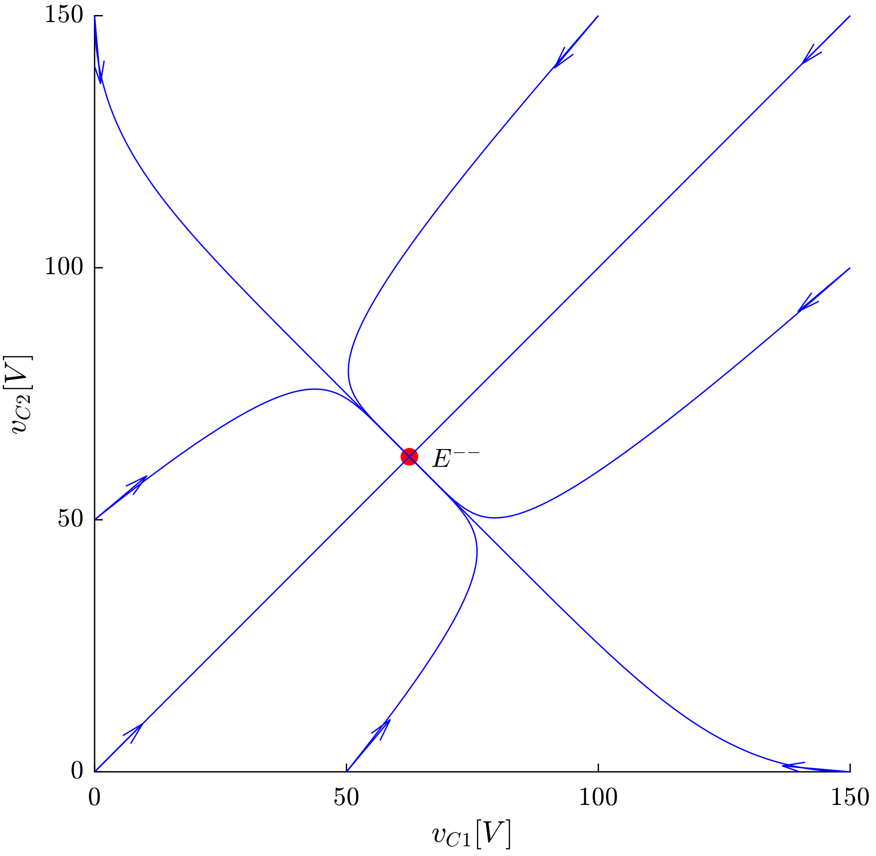

Source – Own elaboration.

Table 3 – Equilibrium points in f^{--} - coordinates, eigenvalues and eigenvectors of the linearized system around these equilibrium points.

Equilibrium Point	$(v_{C1}\ ;\ v_{C2})$	λ_1	λ_2	$\boldsymbol{v_1}$	$\boldsymbol{v_2}$
E^{--}	(62,5 ; 62,5)	-8,510	-1.418	$[0,707\ 0,707]^T$	$[0,707\ -0,707]^T$

Source – Own elaboration.

The time response corresponding to one of the trajectories in the phase plane can be seen in Figure 16. We can see in this figure that the voltage of both capacitors rise in the first instants, then they balance between themselves reaching the global stable equilibrium point.

Figure 16 – Time response of f^{--}

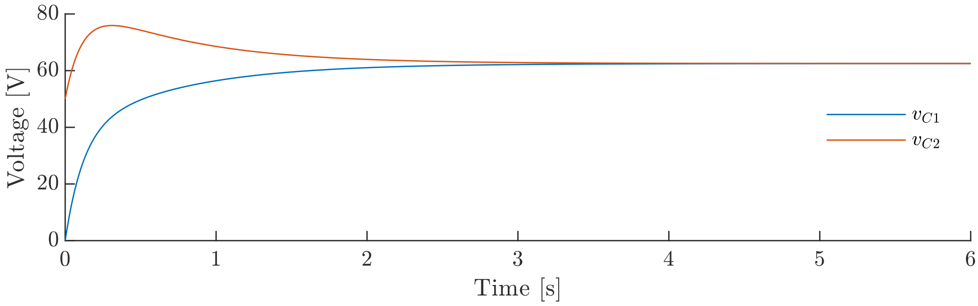

Source – Own elaboration.

4.1.2 f^{-+} field

The f^{-+} field is affected by the presence of one constant power load in one of the submodules. In figure 16 we can see its vector field. The null isocline $f_2^+ = 0$,

$$v_{C1} = V_{DC} - v_{C2}\left(1 + \frac{R_l}{R_{b2}}\right) - \frac{P_2 R_l}{v_{C2}},$$

is bent, in comparison with $f_2^- = 0$,

$$v_{C1} = V_{DC} - v_{C2}\left(1 + \frac{R_l}{R_{b2}}\right),$$

because of the hyperbola term $\left(\frac{-PR_l}{v_{C2}}\right)$. In this case, because of it, the nullclines do not intersect themselves, and there is no equilibrium point. That way, the field is divided in three main regions. The region to the left of $f_2^+ = 0$ and to the right of $f_1^- = 0$ point both towards the region "in the middle", that points mostly downward-right (or to southeast direction) towards the v_{C1} axis. That means that in this region v_{C1} tends to increase whereas v_{C2} decreases. This is reasonable since there is a constant power load only consuming power in the capacitor whose voltage is v_{C2}.

Figure 17 – Vector field $\boldsymbol{f}^{-+}$

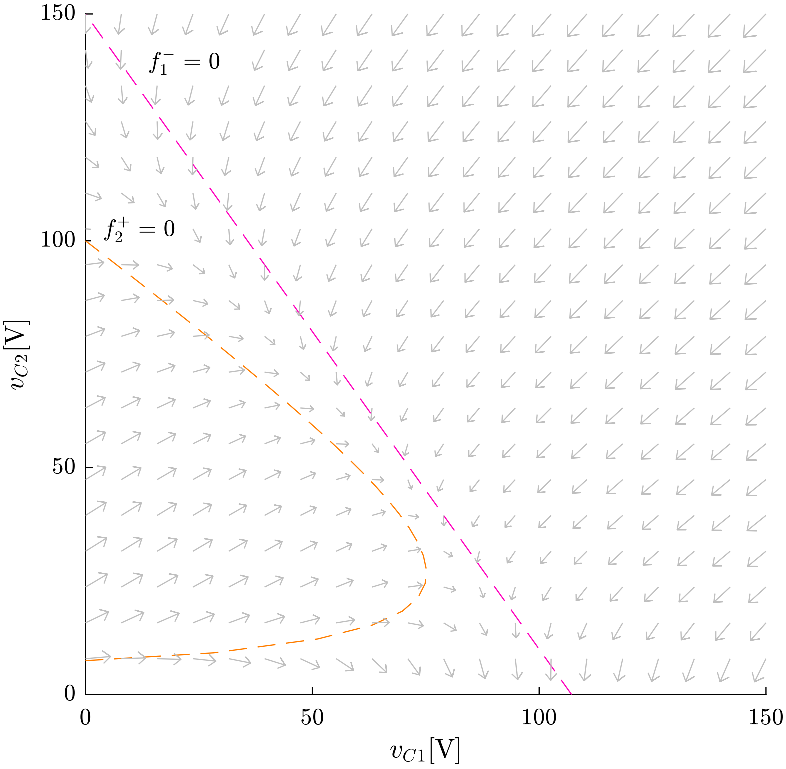

Source – Own elaboration.

The phase portrait of this field can be seen in figure 18. The trajectories converge to a place roughly near the $v_{C1} + v_{C2} = V_{DC}$ line region, indicating that the sum of the capacitors' voltages charge up to the V_{DC} value, and then go downward-right to the direction of v_{C1} axis, following the vector field directions. The simulation is stopped before v_{C2} reaches 0, because $v_{C2} = 0$ is not defined for $\boldsymbol{f}^{-+}$. There are no equilibrium points in this case.

A time response corresponding to one trajectory of the phase portrait of the system can be seen in figure 19. Both voltages begin to rise together and diverge, leading to charge in v_{C1} and discharge in v_{C2}. When v_{C2} reaches 0, the simulation stops. In the real system, the MMC may shut down since the voltage reaches a inferior safety threshold.

As seen in analysis section, the vector field could have another form depending on the parameter values. If the other parameters remained the same as the ones in Table 2 except that $P < P_{2c}^{-+} = 6.6964$ W (according to (39)), the null isocline $f_2^+ = 0$ would bent in a way that it crosses $f_1^- = 0$ in two points, thus there would be two equilibrium points. Analyzing the vector field directions, one would be a stable sink and the other an unstable saddle point. In that way, the system would be locally asymptotically stable and it would be possible to reach an equilibrium, even with a constant power load in only one of the two submodules. This equilibrium point would not be over the line

$v_{C1} = v_{C2}$, though. In that way, one could say that this equilibrium is not desired if trajectories begin at the starting point $(v_{C1}, v_{C2}) = (0,0)$, as trajectories converging to it do not correspond to a desirable behavior of the system. The form of this field can be understood physically. The constant power load has a characteristic that it drains more current when the voltage is lower and less current when it is higher, thus inducing the system onto unbalance and instability. Therefore, if the system is "unbalanced enough", its trajectory do not reach a stable equilibrium. Moreover, if the power consumed in it is high enough, such as this example, there is no state within the operating region from which the trajectory can reach any equilibrium point.

Figure 18 – Phase portrait of f^{-+}.

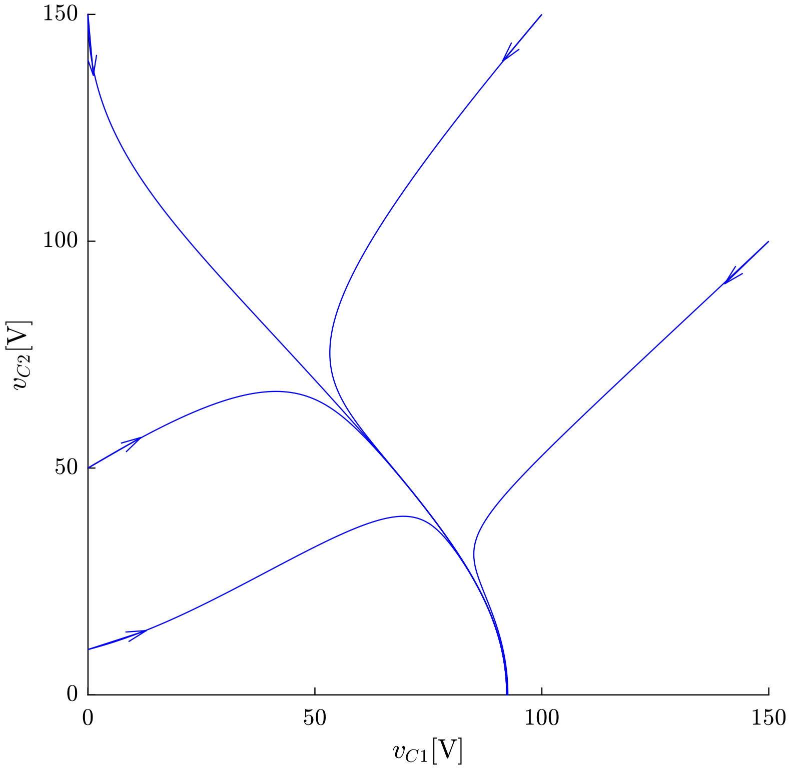

Source – Own elaboration.

Figure 19 – Time response of f^{-+}.

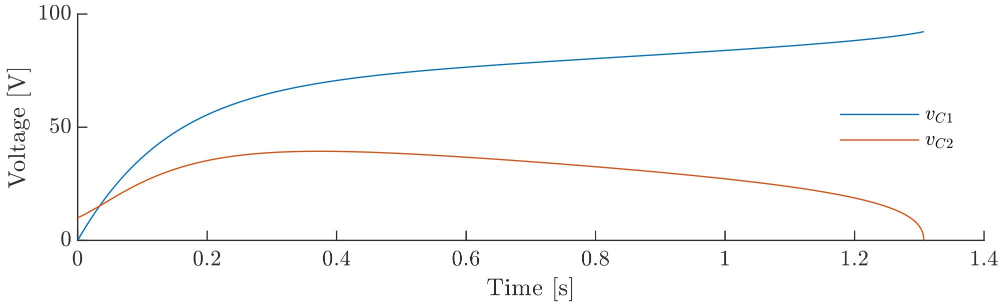

Source – Own elaboration.

4.1.3 f^{++} Field

In the $\boldsymbol{f}^{++}$, we have the constant power loads active in both submodules. In Figure 20 its vector field is illustrated. Both null isoclines $f_1+=0$ and $f_2+=0$,

$$v_{C2} = V_{DC} - v_{C1}\left(1+\frac{R_l}{R_{b1}}\right) - \frac{P_1 R_l}{v_{C1}},$$
$$v_{C1} = V_{DC} - v_{C2}\left(1+\frac{R_l}{R_{b2}}\right) - \frac{P_2 R_l}{v_{C2}},$$

are bent, because of the hyperbola terms $-\dfrac{PR_l}{v_{C1}}$ and $-\dfrac{PR_l}{v_{C2}}$, respectively. The nullclines intercept each other in four distinct points, dividing the field in seven regions. At these intersection, there are the equilibrium points, one locally stable and three unstable. We can also think of the region around each equilibrium point being divided in four, each one with a dominant vector field direction.

Figure 20 – Vector field $\boldsymbol{f}^{++}$

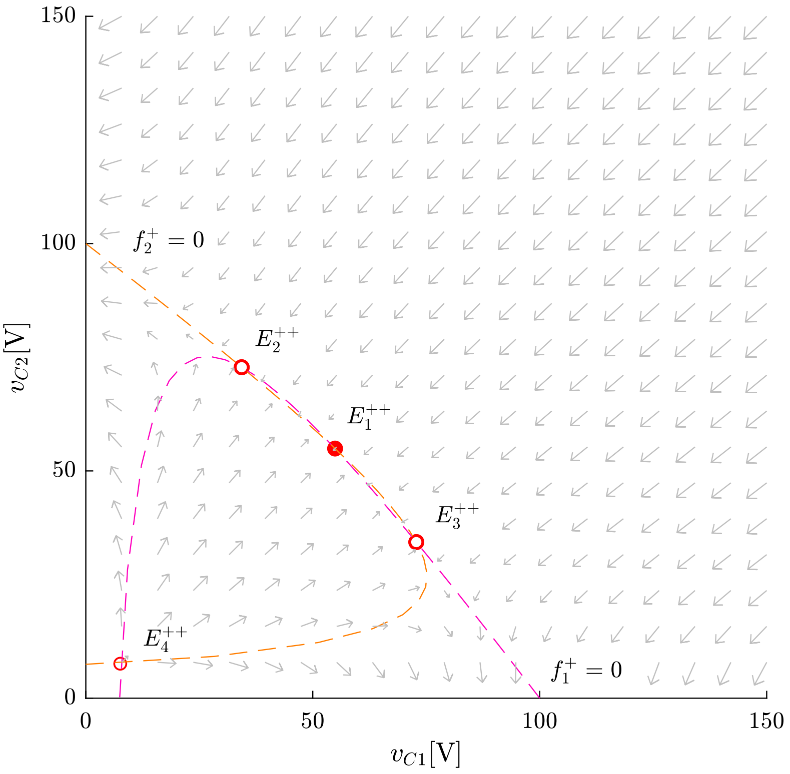

Source – Own elaboration.

The equilibrium point $\boldsymbol{E_1^{++}}$ is the desired operating equilibrium point of the system, where $v_{C1} = v_{C2}$, and it is a stable sink, since both eigenvalues of the system linearized around it have real negative part (Table 4). Similar to $\boldsymbol{E}^{--}$, its eigenvectors $\boldsymbol{v_1}$ and $\boldsymbol{v_2}$ are pointing in the direction of $v_{C1}+v_{C2} = V_{DC}$ and $v_{C1} = v_{C2}$ respectively. The eigenvalue λ_1 associated with $\boldsymbol{v_1}$ is approximately 30 times greater than λ_2 associated with $\boldsymbol{v_2}$. In that way, it is expected that in the neighborhood of $\boldsymbol{E_1^{++}}$, the trajectories tend to go faster towards $v_{C1} + v_{C2} = V_{DC}$, than towards $v_{C1} = v_{C2}$, meaning that the system first tends to charge so that the sum of capacitor voltages balance the voltage source voltage V_{DC} and then later they balance between themselves.

The equilibrium points $\boldsymbol{E_2^{++}}$ and $\boldsymbol{E_3^{++}}$ are both saddle points, as both have both a real positive and a real negative eigenvalue (Table 4). As the parameter values in each submodule are equal in this nominal case, the system has a symmetry in the vector field in relation to the line $v_{C1} = v_{C2}$: so $E_{21}^{++} = E_{32}^{++}$ and $E_{31}^{++} = E_{22}^{++}$. They eigenvectors $\boldsymbol{v_1}$ and $\boldsymbol{v_2}$ point to approximately the same directions of the eigenvalues of $\boldsymbol{E_1^{++}}$, and the difference in the order of magnitude of the eigenvalues is approximately equal to the case in $\boldsymbol{E_1^{++}}$.

The last equilibrium point is $\boldsymbol{E_4^{++}}$. It is an unstable node, since both of its eigenvalues are real positive (Table 4). It occurs because the less the voltage is, the greater is the current drained by the constant power load. So if the voltages v_{C1} or v_{C2} are low enough, there would be no current enough to charge the capacitors.

Table 4 – Equilibrium points in f^{++} - coordinates, eigenvalues and eigenvectors of the linearized system around these equilibrium points.

Equilibrium Point	$(v_{C1}\ ;\ v_{C2})$	λ_1	λ_2	$\boldsymbol{v_1}$	$\boldsymbol{v_2}$
$\boldsymbol{E_1^{++}}$	(54,912 ; 54,912)	-7,334	- 0,242	$[0,707\ 0,707]^T$	$[-0,707\ 0,707]^T$
$\boldsymbol{E_2^{++}}$	(72,804 ; 34,338)	-6,860	0.607	$[-0.810\ -0,586]^T$	$[0,586\ 0,810]^T$
$\boldsymbol{E_3^{++}}$	(34,338 ; 72,804)	0.607	- 6,860	$[0.810\ -0,586]^T$	$[0,586\ 0.810]^T$
$\boldsymbol{E_4^{++}}$	(7,587 ; 7,587)	53,079	60,171	$[-0,707\ -0,707]^T$	$[-0,707\ 0,707]^T$

Source – Own elaboration.

The operating equilibrium point is locally asymptotically stable, and we can find trajectories that both converge to and diverge from it. The system trajectories can be seen in the phase portrait in Figure 21. If the initial conditions of the trajectory are within the attraction domain of the stable node $\boldsymbol{E_1^{++}}$, then they will asymptotically converge to it. If they start outside, the system trajectory will diverge from it, meaning an unbalance either discharging v_{C1} and charging v_{C2} or vice-versa. The simulation is stopped before $v_{C1} = 0$ or $v_{C2} = 0$, because these values are not defined for f^{++}. The attraction domain of $\boldsymbol{E_1^{++}}$ is delimited by the green lines in Figure 21, which correspond to the stable subspace of the saddle points $\boldsymbol{E_2^{++}}$ and $\boldsymbol{E_3^{++}}$. It is also interesting to notice that the real-negative eigenvalues of $\boldsymbol{E_2^{++}}$ and $\boldsymbol{E_3^{++}}$ are associated with eigenvectors tangent to its stable subspace (Table 4). Any trajectory starting over this subspace will converge to these equilibrium points. However, this space is as thin as a line, and it is practically not feasible that such thing ever happens.

In Figure 22 it is illustrated a time response of the system corresponding to a trajectory with initial conditions inside the attraction domain of $\boldsymbol{E_1^{++}}$. It converges to the operating point, thus reaching balance. Similarly to time responses of the fields f^{--} and f^{-+}, the voltages initially rise together, and then balance between themselves in a slower dynamic. In Figure 23 it is shown a time response corresponding to a trajectory that diverges from the operating point, reaching unbalance.

Figure 21 – f^{++} phase portrait.

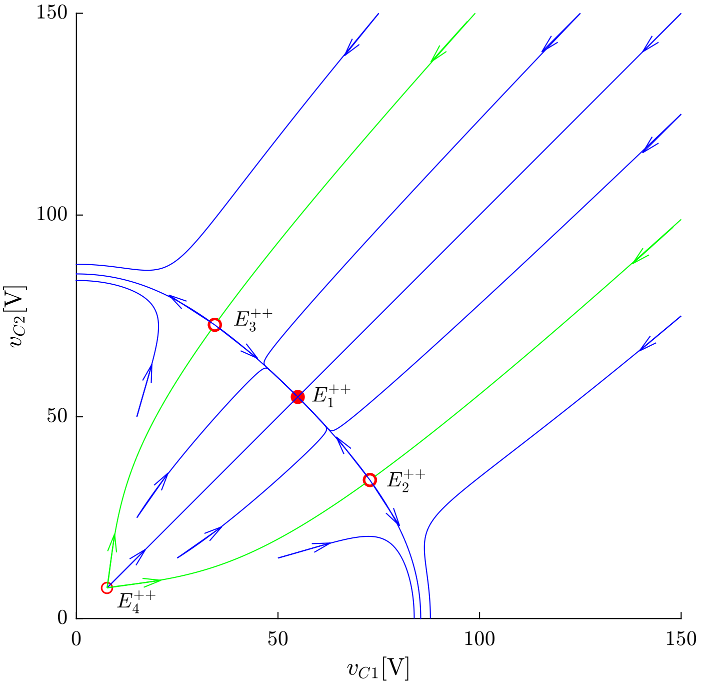

Source – Own elaboration.

Figure 22 – f^{++} Time response - converging.

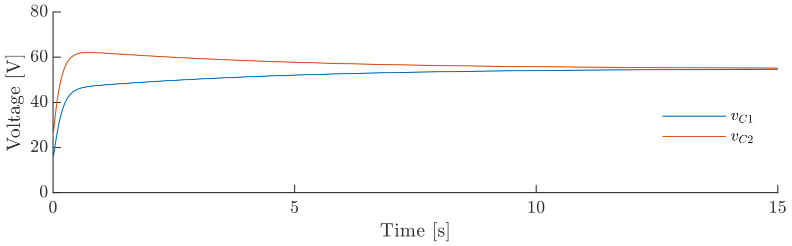

Source – Own elaboration.

Figure 23 – f^{++} Time response - diverging

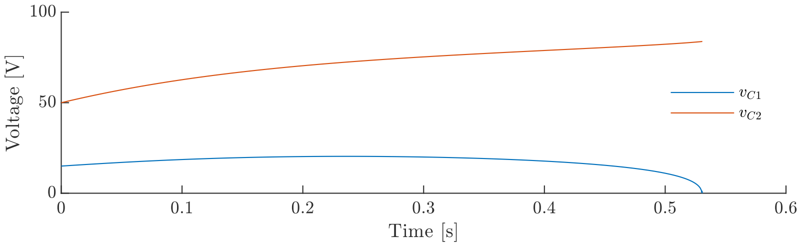

Source – Own elaboration.

4.1.4 f Field

Lastly for the nominal case, are the simulation results regarding $\boldsymbol{f}$. In Figure 24 we can see its vector field. There is only one equilibrium point, $\boldsymbol{E_1^{++}}$, and there are discontinuities in the vector fields at the boundaries Σ_1 and Σ_2. The fact that the constant power loads are only active if the corresponding capacitor voltage is greater than the minimum voltage V_{Cmin} curiously helps to stabilize the system, which is in this case, apparently, globally asymptotically stable. In order to check it, we can look carefully at each field and interaction with its boundaries, as well as the dynamics in the boundaries themselves.

Figure 24 – Vector field $\boldsymbol{f}$

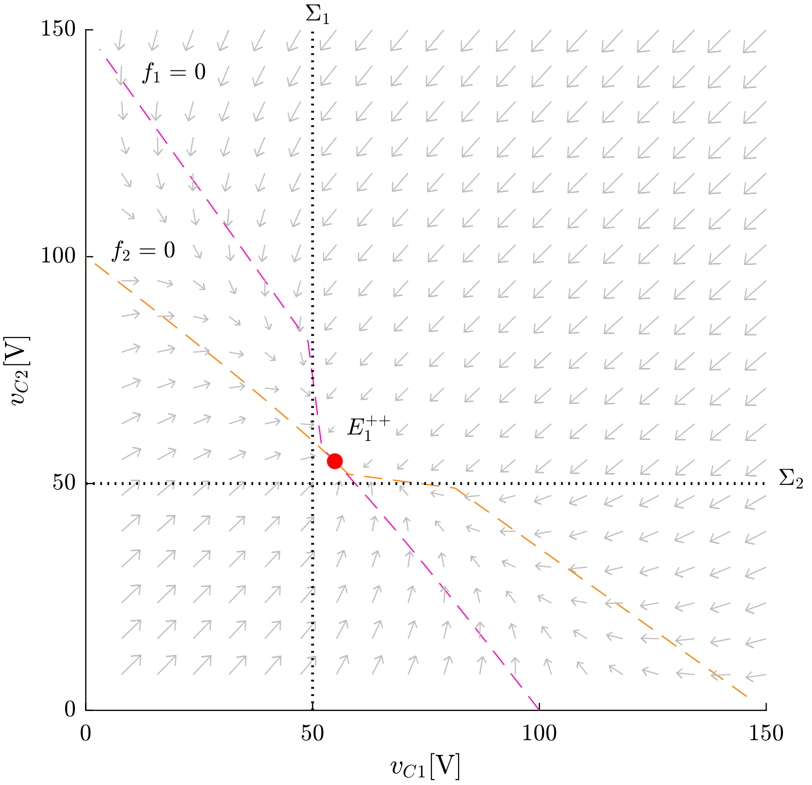

Source – Own elaboration.

In Figure 25 there are the sliding regions at the boundaries Σ_1 and Σ_2. As they are symmetric, we explain here what happens in Σ_1 and in Σ_2 it is just the same. The thicker lines over the boundaries Σ_1 and Σ_2 represent the attractive sliding regions Σ_1^{as} and Σ_2^{as}. In these regions, the vector field at each side of the boundaries point towards the boundary, and any trajectory that reaches this region slides over it. Analytically, it corresponds to the conditions $L_{f^{--}}h_1 = L_{f^{-+}}h_1 > 0$ and $L_{f^{+-}}h_1 = L_{f^{++}}h_1 < 0$. In the extremes of the sliding regions, there are the tangency points. For Σ_1 there is the invisible fold $\boldsymbol{T_1^+}$ and the visible fold $\boldsymbol{T_1^-}$. The dot-dashed lines correspond to points where the field is perpendicular to the boundary gradient vector. In its intersection with the boundary, the tangency points are located. Analytically, they correspond to when the Lie derivatives are null. Here, they coincide with the field nullclines because the boundaries are perpendicular lines to the axis v_{C1} and v_{C2}, so its gradients are parallel to the respective axis. For example, left from the dot-dashed line $f_1^- = 0$, the v_{C1} component points to the right. Also, in the region over the $f_{1+} = 0$ curve, the v_{C1} component points to the left. At the intersection of these two regions, in Σ_1 the field from both sides of Σ_1 points towards them, therefore it is an attractive sliding region. Points in Σ_1 that are not in Σ_1^{as} neither $\boldsymbol{T_1^-}$ or $\boldsymbol{T_1^+}$ are crossing points. In Figure 26, we can see that there are no pseudo-equilibrium points, that is, $f_2^+ = 0$ does not cross the sliding region.

Figure 25 – Sliding regions, tangency points and null Lie derivatives in $\boldsymbol{f}$

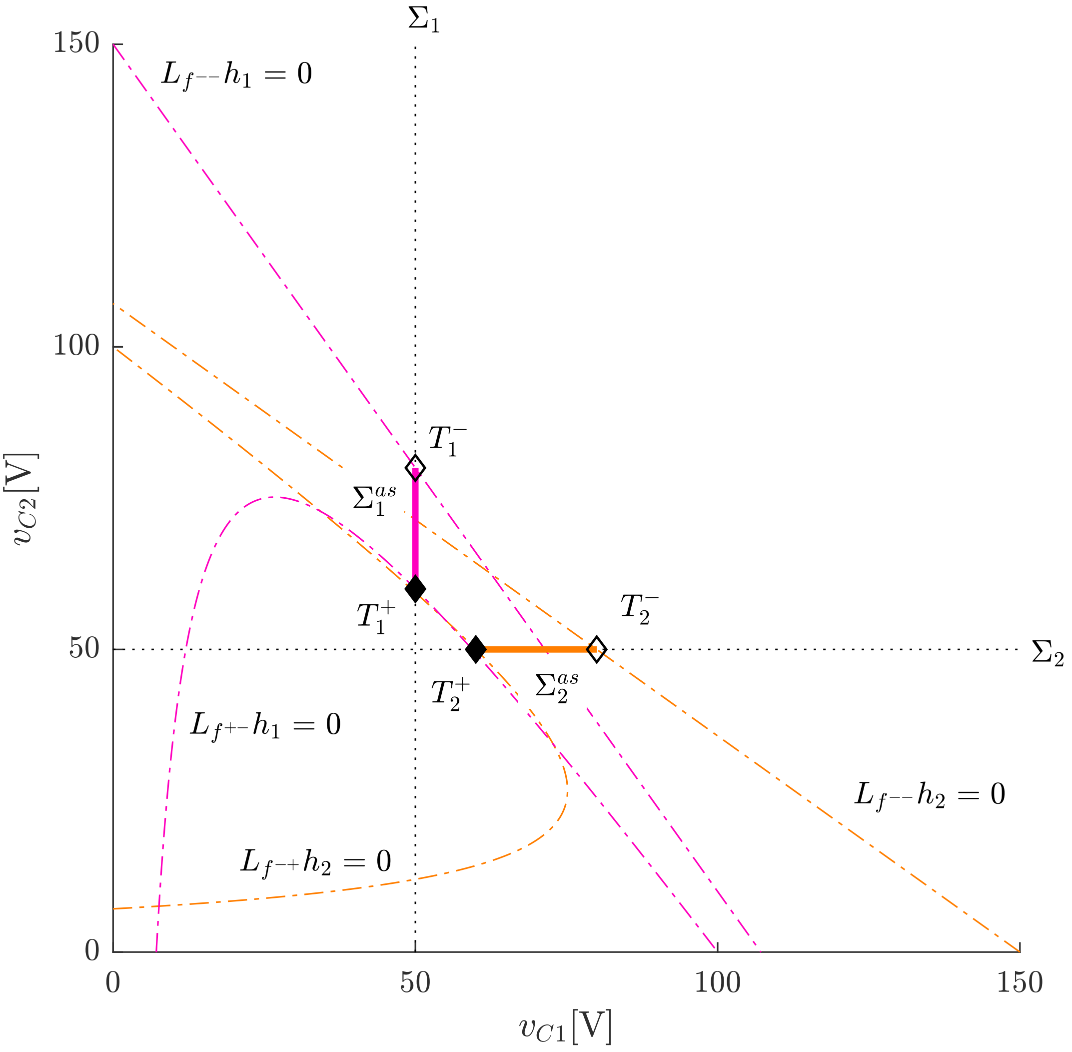

Source – Own elaboration.

Figure 26 – Sliding regions, tangency points and null Lie derivatives in $\boldsymbol{F}$ near Σ_{1as}.

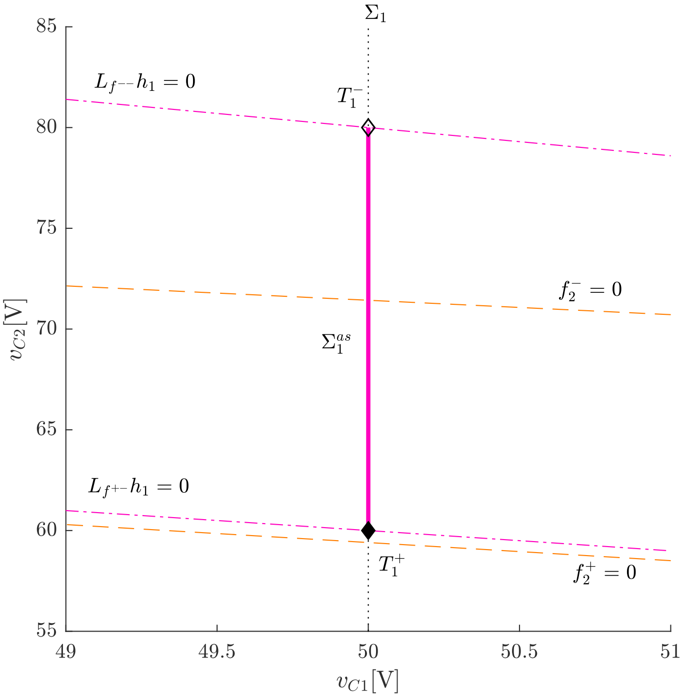

Source – Own elaboration.

We can make a global analysis of $\boldsymbol{f}$ by looking at the vector field (Figure 24), sliding regions (Figure 25) and trajectories at the $\boldsymbol{f}$ phase portrait (Figure 27). Starting on $\mathbb{D}_1$ where $\boldsymbol{f}^{--}$ actuates, the fields leads the system trajectories towards crossings in Σ_1 and in Σ_2. In regions $\mathbb{D}_2$ and $\mathbb{D}_3$, where $\boldsymbol{f}_{-+}$ and $\boldsymbol{f}_{+}$ respectively actuate, the vector field leads the system trajectories to crossings towards $\mathbb{D}_4$ or to sidings over Σ_1^{as} or Σ_2^{as}. The sliding trajectories can be seen in Figure 27. These trajectories slide until they reach one of the visible fold tangency points $\boldsymbol{T_1^-}$ or $\boldsymbol{T_2^-}$ and then cross to the $\mathbb{D}_4$ region, where $\boldsymbol{f}^{++}$ actuates. The vector field in $\mathbb{D}_4$ leads the trajectories to the operating stable equilibrium point, or, to the attractive sliding regions, where they return to $\mathbb{D}_4$ and eventually reach the equilibrium point, or finally, to a crossing towards $\mathbb{D}_2$ or $\mathbb{D}_3$ where they circundate the invisible fold tangency points $\boldsymbol{T_1^+}$ or $\boldsymbol{T_2^+}$, end up in the sliding regions Σ_1^{as} or Σ_2^{as} and slide until the visible fold tangency points $\boldsymbol{T_1^-}$ and $\boldsymbol{T_2^-}$ where they cross to $\mathbb{D}_4$ again and eventually also reach the equilibrium point $\boldsymbol{E_1^{++}}$. We can conclude therefore that considering the operating domain of F, the system is, for this set of parameter values, globally asymptotically stable.

The APSs help to balance the system in this case, because they are turned on only when the voltage in its capacitor is greater than V_{Cmin}. In this example, when v_{C2} is greater than v_{C1}, the auxiliary power supply is turned on, and the time derivative of v_{C2} diminishes while the time derivative of v_{C1} stays the same, thus helping the system to balance faster. This can be seen at the system phase portrait (Figure 27) as all the trajectories beginning in $\mathbb{D}_1$ tend to "funnel" as they cross the boundaries Σ_1 and Σ_2.

Figure 27 – Phase Portrait of f in nominal case simulation.

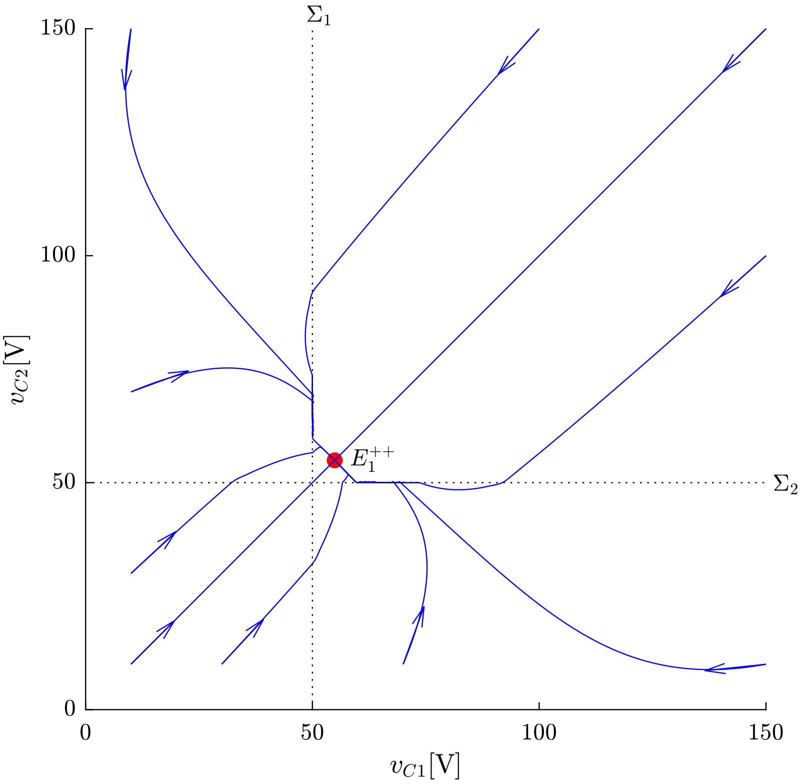

Source – Own elaboration.

It is important to make a remark that, in the practical case, all trajectories part from initial conditions in the $\mathbb{D}_1$ region, ideally from $(v_{C1};v_{C2}) = (0;0)$. Also, in the real system, at least in the prototype we have in our facilities, the system actually turns off if the trajectory crosses from $\mathbb{D}_4$ back to $\mathbb{D}_2$ or $\mathbb{D}_3$ (if an auxiliary power supply is turned on and then it must be turned off because the voltage is too low), because of safety reasons. In the Figure 28, it is possible to see trajectories that come from $\mathbb{D}_1$, cross to $\mathbb{D}_2$ and $\mathbb{D}_3$ and then go to $\mathbb{D}_4$ (or cross directly to $\mathbb{D}_4$) and then reach the operating point, showing that it is feasible that the system works as desired in a real situation where the safety measures are implemented.

A time response of the system with initial conditions in $\mathbb{D}_1$ is illustrated in Figure 29. We can see that in the first instants the voltages begin to rise together. We can see that then the constant power load is active in the second submodule, because there is a discontinuity in the time derivative of v_{C2} near 0,1 s. After that, the same happens also for v_{C1} near 0,2 s. Then the voltages slowly converge to the equilibrium voltage, balancing between themselves.

In sum, the dynamics of the studied piecewise smooth system show that: (i) there is no real pseudo equilibrium point, (ii) there are two sliding regions and (iii) there is only one real equilibrium point of f which is the operating point of the system.

Figure 28 – Phase Portrait of $\boldsymbol{f}$ - Zoom near $\boldsymbol{E_1^{++}}$

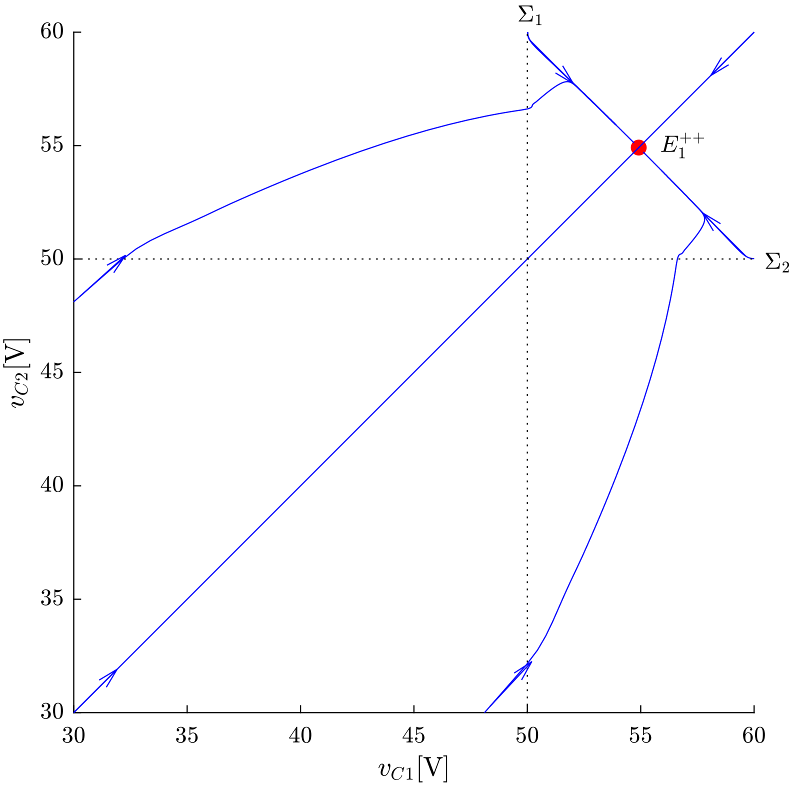

Source – Own elaboration.

Figure 29 – Time response of $\boldsymbol{f}$. Full time (a) and zoom in its first instants (b).

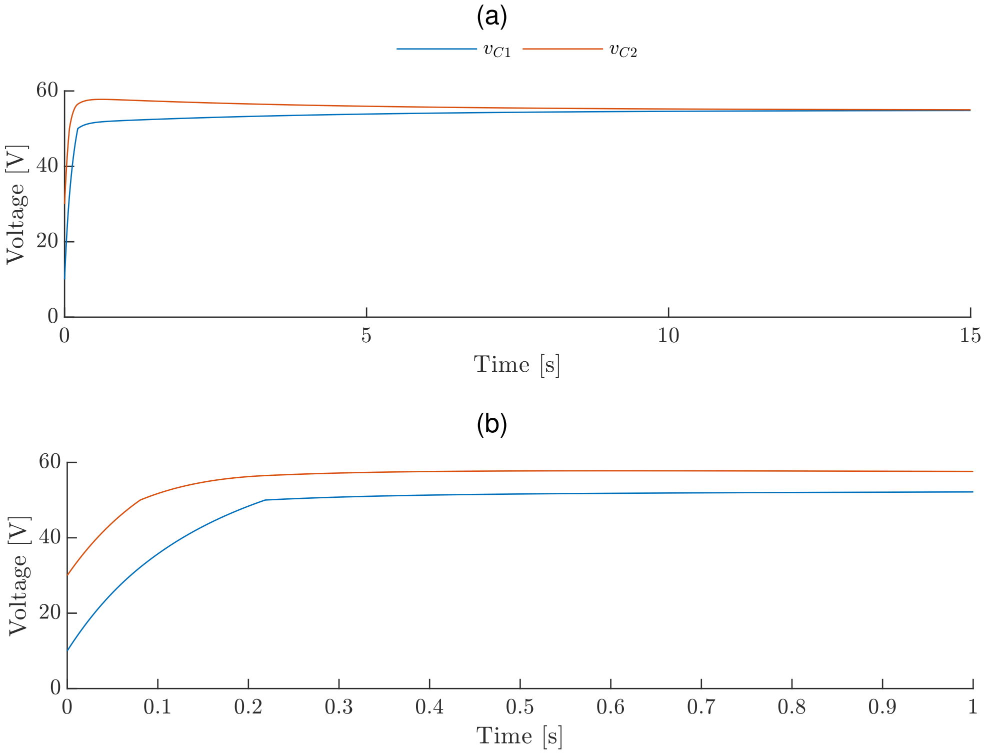
(a)

(b)

Source – Own elaboration.

4.2 STUDY OF THE SYSTEM UNDER PARAMETRIC VARIATION

4.2.1 Two Submodule System - Variation of R_b

As seen in the analysis section and illustrated by the previous simulation results, introducing R_b with adequate value, the system can be stabilized. In this section, it is shown what happens to the system, specially regarding stability, with the variation of R_b. It is shown that it is not sufficient that the R_b value is chosen so that the operating point is stable in order to the system to work as desired.

4.2.1.1 *Insuficient γ or E_1^{++} unstable*

We begin by showing what happens when the value of R_b does not satisfy (61). For the parameters specified in Table 5, we simulated the f^{++} field, which contains the operating point. Its vector field (Figure 30) contains two equilibrium points, instead of four like in the previous case. By looking at the vector field direction, and also to the equilibrium points correspondent eigenvalues presented in Table 6, we see that $\boldsymbol{E_4^{++}}$ remains as an unstable node, whereas $\boldsymbol{E_1^{++}}$ becomes a saddle point (unstable). The equilibrium points $\boldsymbol{E_2^{++}}$ and $\boldsymbol{E_3^{++}}$ are not present. These change of equilibrium points number and type in the vector field in dependence of the variation of one parameter configures a bifurcation. More specifically, a bifurcation of type pitchfork is present in this circuit's system. Whenever $\gamma > 1$, $\boldsymbol{E_1^{++}}$ is stable, $\boldsymbol{E_2^{++}}$ and $\boldsymbol{E_3^{++}}$ exist as saddle points. If $\gamma = 1$, these three points collide, and $\gamma < 1$ corresponds to this present case.

Table 5 – Circuit parameters for simulation of the case with an unstable operation equilibrium point. The resistance R_b is dimensioned so that $\gamma = 0{,}8$.

N	V_{DC}[V]	$R_l[\Omega]$	C[mF]	P[W]	$R_b[\Omega]$
2	150	100	2,82	10	450

Source – Own elaboration.

Table 6 – Equilibrium points in f^{++} - coordinates, eigenvalues and eigenvectors of the linearized system around these equilibria for $\gamma = 0.8$.

Equilibrium Point	$(v_{C1}\ ;\ v_{C2})$	λ_1	λ_2	$\boldsymbol{v_1}$	$\boldsymbol{v_2}$
$\boldsymbol{E_1^{++}}$	(60 ; 60)	- 6,8952	0.19701	$[0{,}70711\ 0{,}70711]^T$	$[-0{,}70711\ 0{,}70711]^T$
$\boldsymbol{E_4^{++}}$	(7,5 ; 7,5)	55,1615	62,2537	$[-0{,}70711\ -0{,}70711]^T$	$[-0{,}70711\ 0{,}70711]^T$

Source – Own Elaboration.

Figure 30 – Vector field of f^{++} for $\gamma = 0.8$

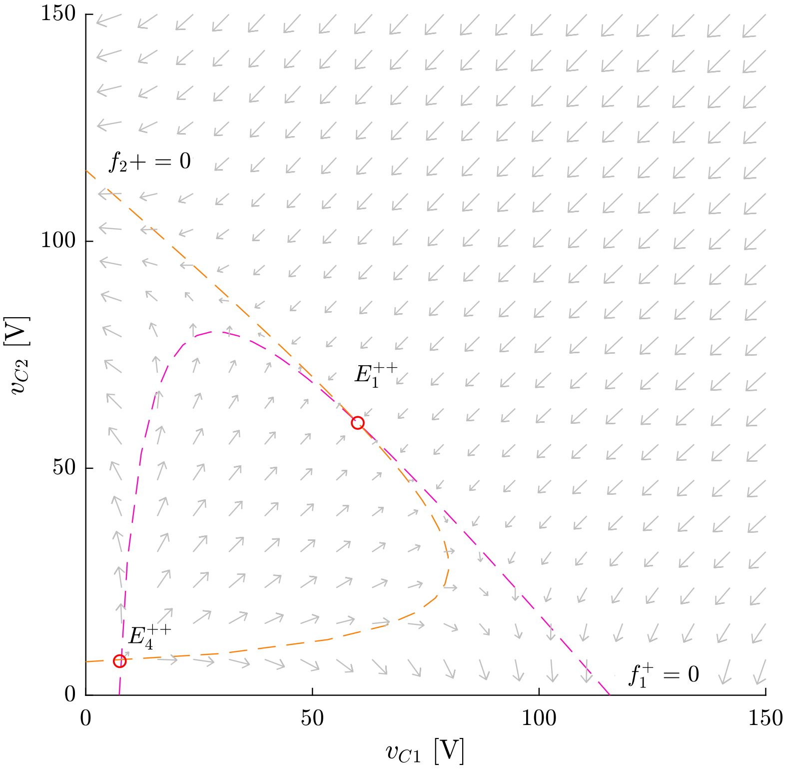

Source – Own elaboration.

We can see the system phase portrait in Figure 31. Because $\boldsymbol{E_1^{++}}$ is a saddle point, it has a stable subspace (or manifold) associated to it, drawn in green. Any trajectory with initial conditions starting over this subspace will asymptotically converge to $\boldsymbol{E_1^{++}}$. This means that, theoretically, if the circuit parameters in every submodule is perfectly equal, and it started in a initial condition where v_{C1} is identical to v_{C2}, the system would reach balance. In the real world, though, these conditions are not feasible. There are always some uncertainty or lack of accuracy in the parameter values, and even if they were perfect, any deviation caused by any disturbance would take the system away from the equilibrium and leading to unbalance, since the equilibrium is unstable. A typical time response of this situation is illustrated in Figure 32.

Figure 31 – Phase portrait of f^{++} for $\gamma = 0,8$

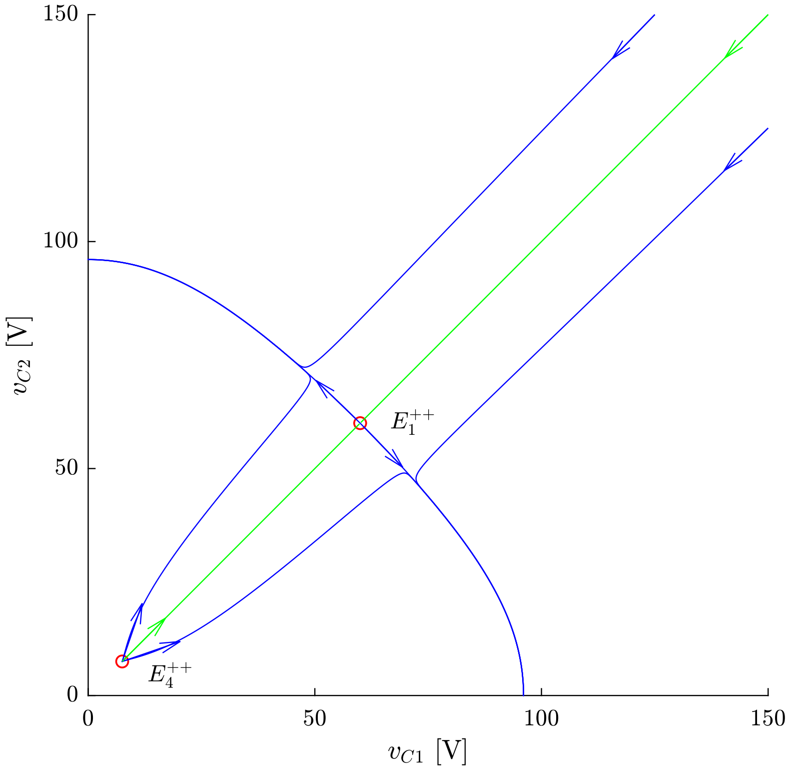

Source – Own Elaboration.

Figure 32 – A time response of f^{++} for $\gamma = 0,8$

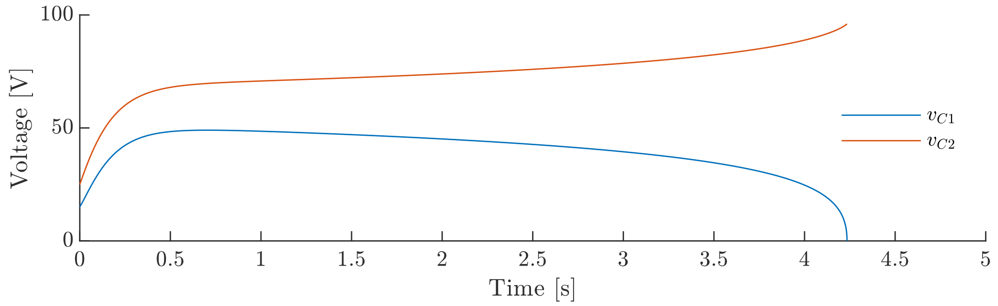

Source – Own Elaboration.

4.2.1.2 *Attraction domain of* E_1^{++} *variation in dependence with* R_b

In order to work properly, some conditions must be fulfilled. The operating equilibrium point $\boldsymbol{E_1^{++}}$ must be stable. The system trajectory, when reaches $\mathbb{D}_4$, should be inside the attraction domain of $\boldsymbol{E_1^{++}}$. Otherwise, the system trajectories tend to reach the boundaries Σ_1 or Σ_2 and the real circuit turns itself off for safety reasons.

For $\gamma < 1$, $\boldsymbol{E_1^{++}}$ is a saddle point. For $\gamma = 1$, the equilibrium points $\boldsymbol{E_1^{++}}$, $\boldsymbol{E_2^{++}}$ and $\boldsymbol{E_3^{++}}$ collide in one degenerated point, that has a saddle point characteristic. These cases are developed in more details in the next tertiary sections "$\boldsymbol{f^{++}}$ *Bifurcation Diagram*" and "*A Locally Stable Case*".

For $\gamma > 1$, $\boldsymbol{E_1^{++}}$ is stable and there is an attraction domain. The equilibrium points $\boldsymbol{E_2^{++}}$ and $\boldsymbol{E_3^{++}}$ are present in distinct loci, and their stable subspaces delimit the attraction domain of $\boldsymbol{E_1^{++}}$.

We can see the stable manifolds of $\boldsymbol{E_2^{++}}$ and $\boldsymbol{E_3^{++}}$ for several γ values in Figure 33. For $\gamma > 1$, these delimit the attraction domain of $\boldsymbol{E_1^{++}}$. For $\gamma = 1$, $\boldsymbol{E_1^{++}}$, $\boldsymbol{E_2^{++}}$ and $\boldsymbol{E_3^{++}}$ collide in one point that has a saddle point characteristic. The γ values and respective R_b values are listed in Table 7. Interestingly, the influence of γ in expanding the limits of the attraction domain of $\boldsymbol{E_1^{++}}$ tends to diminish as γ increases.

In a practical case, γ must be more than only sufficient to stabilize $\boldsymbol{E_1^{++}}$. In the next chapter, we try to answer what is the minimum value of γ that maintains the system properly working, taking into account uncertainties in the capacitance values, a situation that is far common in a real system. We search also for a value of R_b that ensures not only local, but global stability.

Table 7 – Circuit parameters for simulations of variation of $\boldsymbol{E_1^{++}}$ attraction domain limits in dependence with γ or R_b

Simulation Number	N	V_{DC}[V]	$R_l[\Omega]$	C[mF]	P[W]	$R_b[\Omega]$	γ
1	2	150	100	2,82	10	332,4173	1,0
2	2	150	100	2,82	10	288,9176	1,1
3	2	150	100	2,82	10	252,0833	1,2
4	2	150	100	2,82	10	220,2374	1,3
5	2	150	100	2,82	10	192,1147	1,4
6	2	150	100	2,82	10	166,6667	1,5

Source – Own Elaboration.

Figure 33 – Stable manifolds of $\boldsymbol{E}_{\mathbf{2}}^{++}$ and $\boldsymbol{E}_{\mathbf{3}}^{++}$ for several γ values.

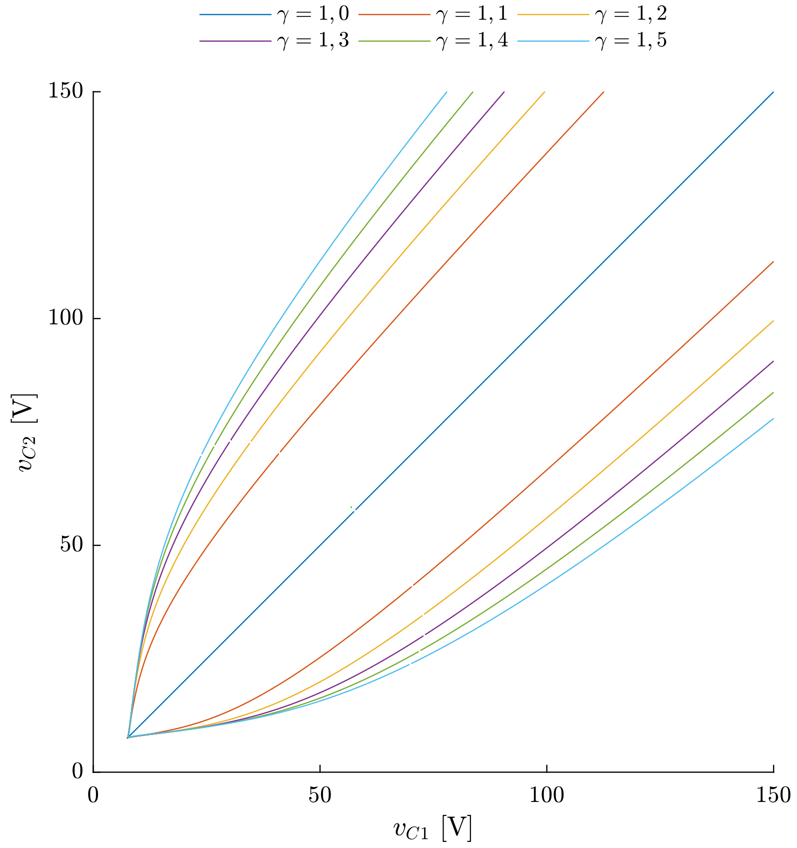

Source – Own Elaboration.

f^{++} Bifurcation Diagram

We analyze here the existence and stability of the equilibrium points in $\boldsymbol{f}^{++}$ in dependence with the variation of R_b, in a bifurcation diagram. In the bifurcation diagram, we plot a coordinate of the $\boldsymbol{f}^{++}$ equilibrium points, and also show whether the equilibrium are stable or not in dependence with R_b.

Recall that $\boldsymbol{f}^{++}$ is given by (26)

$$\boldsymbol{f}^{++} = \begin{bmatrix} f_1^{+} \\ f_2^{+} \end{bmatrix} = \begin{bmatrix} \dfrac{1}{C_1}\left(\dfrac{V_{DC}-(v_{C1}+v_{C2})}{R_l} - \dfrac{P_1}{v_{C1}} - \dfrac{v_{C1}}{R_{b1}}\right) \\ \dfrac{1}{C_2}\left(\dfrac{V_{DC}-(v_{C1}+v_{C2})}{R_l} - \dfrac{P_2}{v_{C2}} - \dfrac{v_{C2}}{R_{b2}}\right) \end{bmatrix},$$

with the equilibrium points given by (46-49):

$$\boldsymbol{E_1^{++}} = \left(E_{11}^{++}, E_{12}^{++}\right) = \left(\frac{R_bV_{DC}+\sqrt{R_b^2V_{DC}^2-4PR_lR_b(R_l+2R_b)}}{2(R_l+2R_b)}, \frac{R_bV_{DC}+\sqrt{R_b^2V_{DC}^2-4PR_lR_b(R_l+2R_b)}}{2(R_l+2R_b)}\right)$$

$$\boldsymbol{E_2^{++}} = \left(E_{21}^{++}, E_{22}^{++}\right) = \left(\frac{R_bV_{DC}-\sqrt{R_b^2V_{DC}^2-4PR_b(R_l+R_b)^2}}{2(R_l+R_b)}, \frac{R_bV_{DC}+\sqrt{R_b^2V_{DC}^2-4PR_b(R_l+R_b)^2}}{2(R_l+R_b)}\right)$$

$$\boldsymbol{E_3^{++}} = \left(E_{31}^{++}, E_{32}^{++}\right) = \left(\frac{R_bV_{DC}+\sqrt{R_b^2V_{DC}^2-4PR_b(R_l+R_b)^2}}{2(R_l+R_b)}, \frac{R_bV_{DC}-\sqrt{R_b^2V_{DC}^2-4PR_b(R_l+R_b)^2}}{2(R_l+R_b)}\right)$$

$$\boldsymbol{E_4^{++}} = \left(E_{41}^{++}, E_{42}^{++}\right) = \left(\frac{R_bV_{DC}-\sqrt{R_b^2V_{DC}^2-4PR_lR_b(R_l+2R_b)}}{2(R_l+2R_b)}, \frac{R_bV_{DC}-\sqrt{R_b^2V_{DC}^2-4PR_lR_b(R_l+2R_b)}}{2(R_l+2R_b)}\right).$$

The existence condition for $\boldsymbol{E_1^{++}}$ and $\boldsymbol{E_4^{++}}$ is, as in (50)

$$P \leq \frac{R_bV_{DC}^2}{4R_l(R_l+2R_b)} = P_{c14}^{++}.$$

Now, for $\boldsymbol{E_2^{++}}$ and $\boldsymbol{E_3^{++}}$, the condition is as in (51)

$$P \leq \frac{V_{DC}^2R_b}{4(R_l+R_b)^2} = P_{c23}^{++}.$$

Also, we have

$$\boldsymbol{A}^{++} = \begin{bmatrix} \frac{1}{C_1}\left(\frac{P}{v_{C1}^2}-\frac{1}{R_l}-\frac{1}{R_b}\right) & -\frac{1}{R_lC_1} \\ -\frac{1}{R_lC_2} & \frac{1}{C_2}\left(\frac{P}{v_{C2}^2}-\frac{1}{R_l}-\frac{1}{R_b}\right) \end{bmatrix},$$

from which we can determine whether the equilibrium point is stable. An equilibrium point $\boldsymbol{E}^{++} \in \left\{\boldsymbol{E_1^{++}}, \boldsymbol{E_2^{++}}, \boldsymbol{E_3^{++}}, \boldsymbol{E_4^{++}}\right\}$ is stable if $det\left(\boldsymbol{A}^{++}\right)\big|_{\boldsymbol{v_C}=\boldsymbol{E}^{++}} > 0$ and $tr\left(\boldsymbol{A}^{++}\right)\big|_{\boldsymbol{v_C}=\boldsymbol{E}^{++}} < 0$. Based on that, we can plot the bifurcation diagram. The parameters used are exhibited in Table 8.

Table 8 – Parameter values used to draw a bifurcation diagram of f^{++} in dependency with R_b variation.

N	V_{DC}[V]	$R_l[\Omega]$	P[W]
2	150	100	10

Source – Own Elaboration.

The bifurcation diagram of f^{++} varying R_b diagram can be seen in Figure 34, above with the corresponding $\gamma(R_b)$ at $\boldsymbol{E_1^{++}}$. In Figure 34 (b) we can see a saddle-node bifurcation (SNB) for a value of R_b around 27Ω. When R_b is approximately 31Ω, a subcritical pitchfork (sPB) bifurcation happens. We can see in Figure 34 (a) that there is a limited range of values so that $\boldsymbol{E}_1^{++}$ is stable, corresponding to the region where $\gamma > 1$. For $R_b \approx 325\Omega$, there is another sPB bifurcation, and $\boldsymbol{E}_1^{++}$ becomes a saddle point. We can see also, that except for γ_{max}, there are two different R_b values that lead to the same γ value. If one designs R_b like seen in chapter 3, the value from the right-hand side is chosen.

Figure 34 – Bifurcation diagram of $\boldsymbol{f}^{++}$ varying R_b and corresponding $\gamma(R_b)$. Full diagram (a) and zoom close saddle-node bifurcation (b).

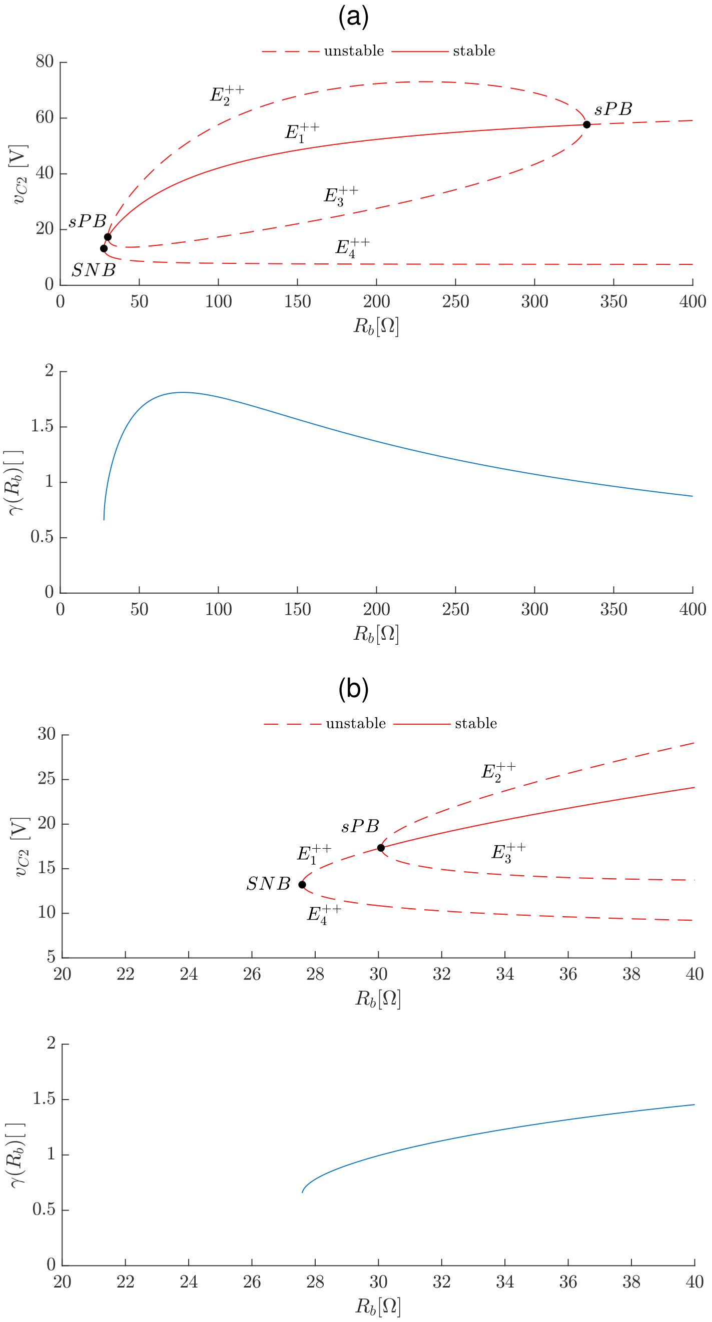

Source – Own Elaboration.

4.2.1.3 *A Locally Stable Operating Point Case*

In this section, we just simulate the whole field f, showing an example of the system in a local-stable operating point situation. We simulate its vector field, sliding regions, phase portrait and calculate data about its equilibrium points.

In Table 9 we show the parameters used in the simulations. The balancing resistance was chosen so that $\gamma = 1.005$. In Figure 35 we can see that in this case $\boldsymbol{E}_{\mathbf{1}}^{++}$ is stable $\boldsymbol{E}_{\mathbf{2}}^{++}$ and $\boldsymbol{E}_{\mathbf{3}}^{++}$ are real and saddle points (Table 10), as discussed in the previous session. Also, the two stable pseudo-nodes $\boldsymbol{E}_{\mathbf{2}}^{s\mathbf{1}+}$ and $\boldsymbol{E}_{\mathbf{2}}^{s\mathbf{2}+}$ are also real.

In Figure 36 we can see the sliding regions of f. The nullcline $f_2^+ = 0$ crosses Σ_1^{as}. Therefore the stable pseudo-node $\boldsymbol{E}_{\mathbf{2}}^{s\mathbf{1}+}$ is real, and by symmetry, $\boldsymbol{E}_{\mathbf{2}}^{s\mathbf{2}+}$ is real too.

In Figure 37 the phase portrait of f is shown. There is an attraction domain around $\boldsymbol{E}_{\mathbf{1}}^{++}$ that is in between the asymptotes that cross $\boldsymbol{E}_{\mathbf{2}}^{++}$ and $\boldsymbol{E}_{\mathbf{3}}^{++}$. The trajectories inside this domain asymptotically converge to $\boldsymbol{E}_{\mathbf{1}}^{++}$, whereas the other can asymptotically converge to $\boldsymbol{E}_{\mathbf{2}}^{++}$ or $\boldsymbol{E}_{\mathbf{3}}^{++}$, if they start on their respective asymptotes (another name for stable subspace), or else, to $\boldsymbol{E}_{\mathbf{2}}^{s\mathbf{1}+}$ or $\boldsymbol{E}_{\mathbf{2}}^{s\mathbf{2}+}$.

In the real system, only the trajectories that asymptotically converge to $\boldsymbol{E}_{\mathbf{1}}^{++}$ correspond to the correct operation of the system. Trajectories that converge to the saddle points corresponds to a non realistic situation, and for our particular prototype, the ones that converge to a pseudo-equilibrium correspond to a situation where the submodules are turned off for safety reasons.

Table 9 – Circuit parameters for simulation of the case with local operating equilibrium point. R_b is dimensioned so that $\gamma = 1.005$

N	V_{DC}[V]	$R_l[\Omega]$	C[mF]	P[W]	V_{Cmin}[V]	$R_b[\Omega]$
2	150	100	2,82	10	50	330,0512

Source – Own elaboration.

Table 10 – Equilibrium points in f - coordinates, eigenvalues and eigenvectors of the linearized system around these equilibria for $\gamma = 1,005$.

Equilibrium Point	$(v_{C1}\ ;\ v_{C2})$	λ_1	λ_2	$\boldsymbol{v}_{\mathbf{1}}$	$\boldsymbol{v}_{\mathbf{2}}$
$\boldsymbol{E}_{\mathbf{1}}^{++}$	(57,59 ; 57,59)	- 7,097	-0.00534	$[0,707\ 0,707]^T$	$[-0,707\ 0,707]^T$
$\boldsymbol{E}_{\mathbf{2}}^{++}$	(54,00 ; 61,11)	-7,086	0,0107	$[0,693\ 0,720]^T$	$[0,720\ 0,693]^T$
$\boldsymbol{E}_{\mathbf{3}}^{++}$	(61,11 ; 54,00)	-7,086	0,0107	$[-0,720\ -0,693]^T$	$[0,693\ -0,720]^T$
$\boldsymbol{E}_{\mathbf{2}}^{s\mathbf{1}+}$	(50,00 ; 64,92)	-	-	-	-
$\boldsymbol{E}_{\mathbf{2}}^{s\mathbf{2}+}$	(64,92 ; 50,00)	-	-	-	-

Source – Own elaboration.

Figure 35 – $\boldsymbol{f}$ vector field for $\gamma = 1{,}005$. Domain $\mathbb{D}$ (a) and zoom near $\boldsymbol{E_1^{++}}$ (b)

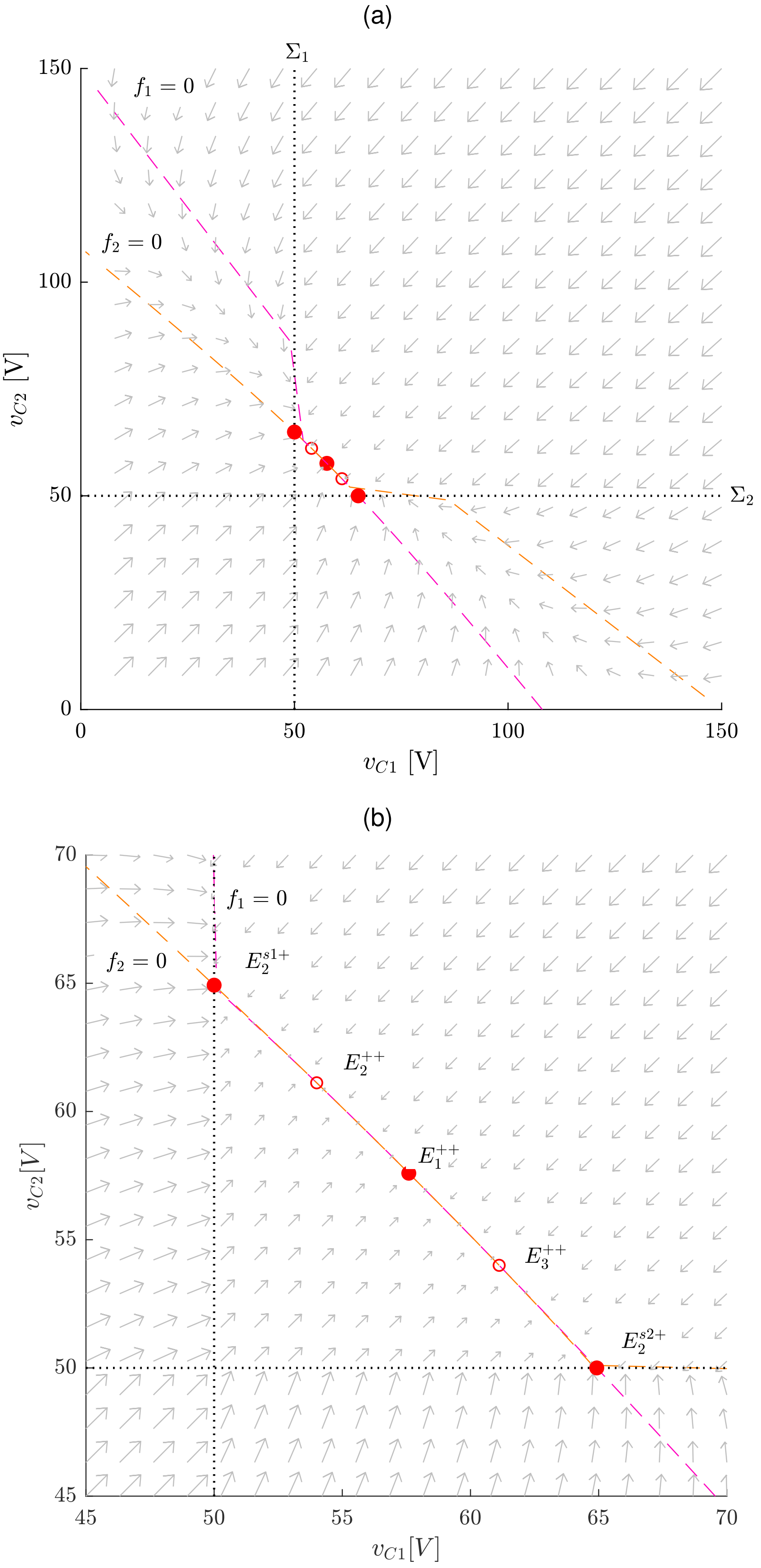

Source – Own Elaboration.

Figure 36 – $\boldsymbol{f}$ sliding regions for $\gamma = 1.005$. Domain $\mathbb{D}$ (a) and zoom near $\boldsymbol{T_1^+}$ (b).

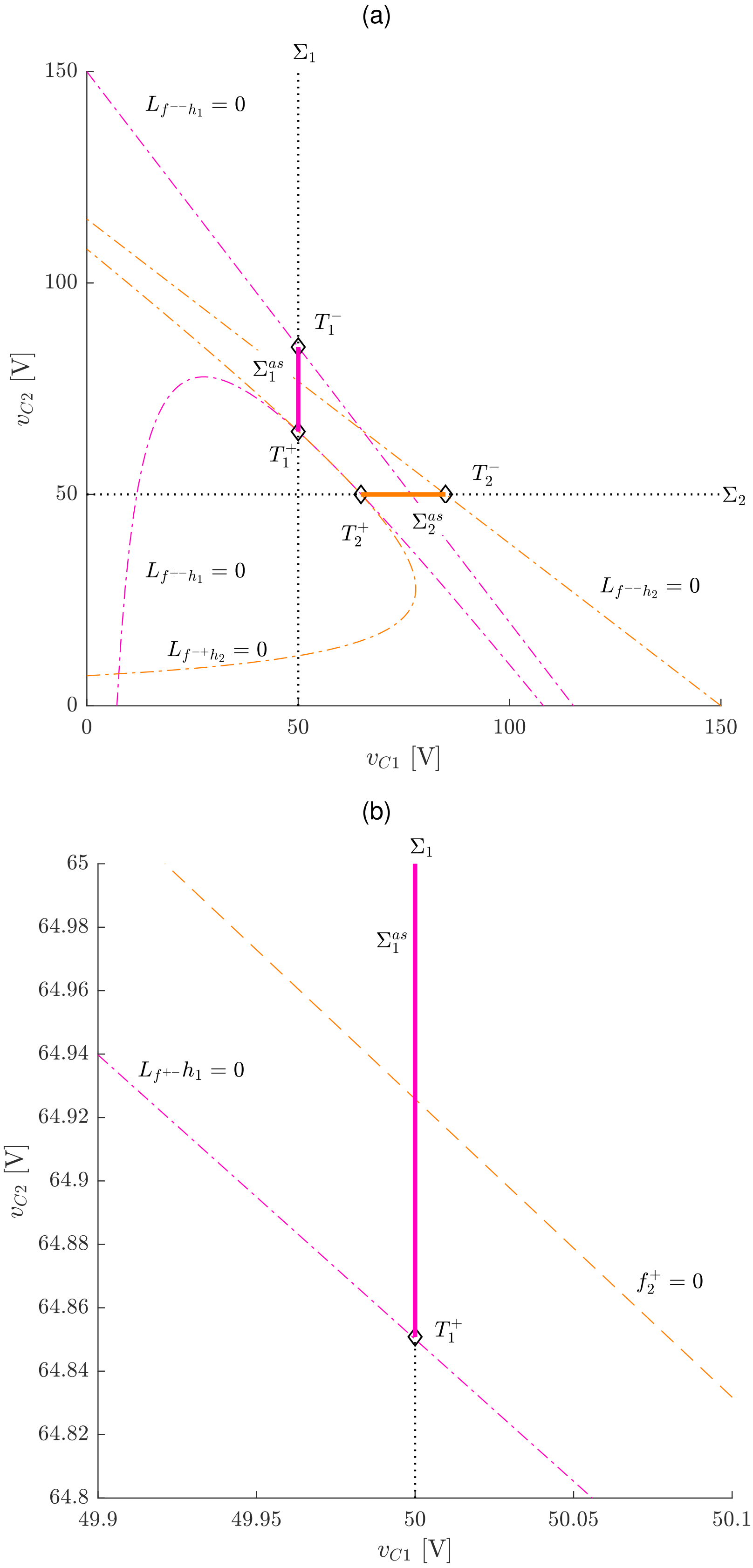

Source – Own Elaboration.

Figure 37 – f phase portrait for $\gamma = 1.005$. Domain D (a) and zoom near E_1^{++} (b).

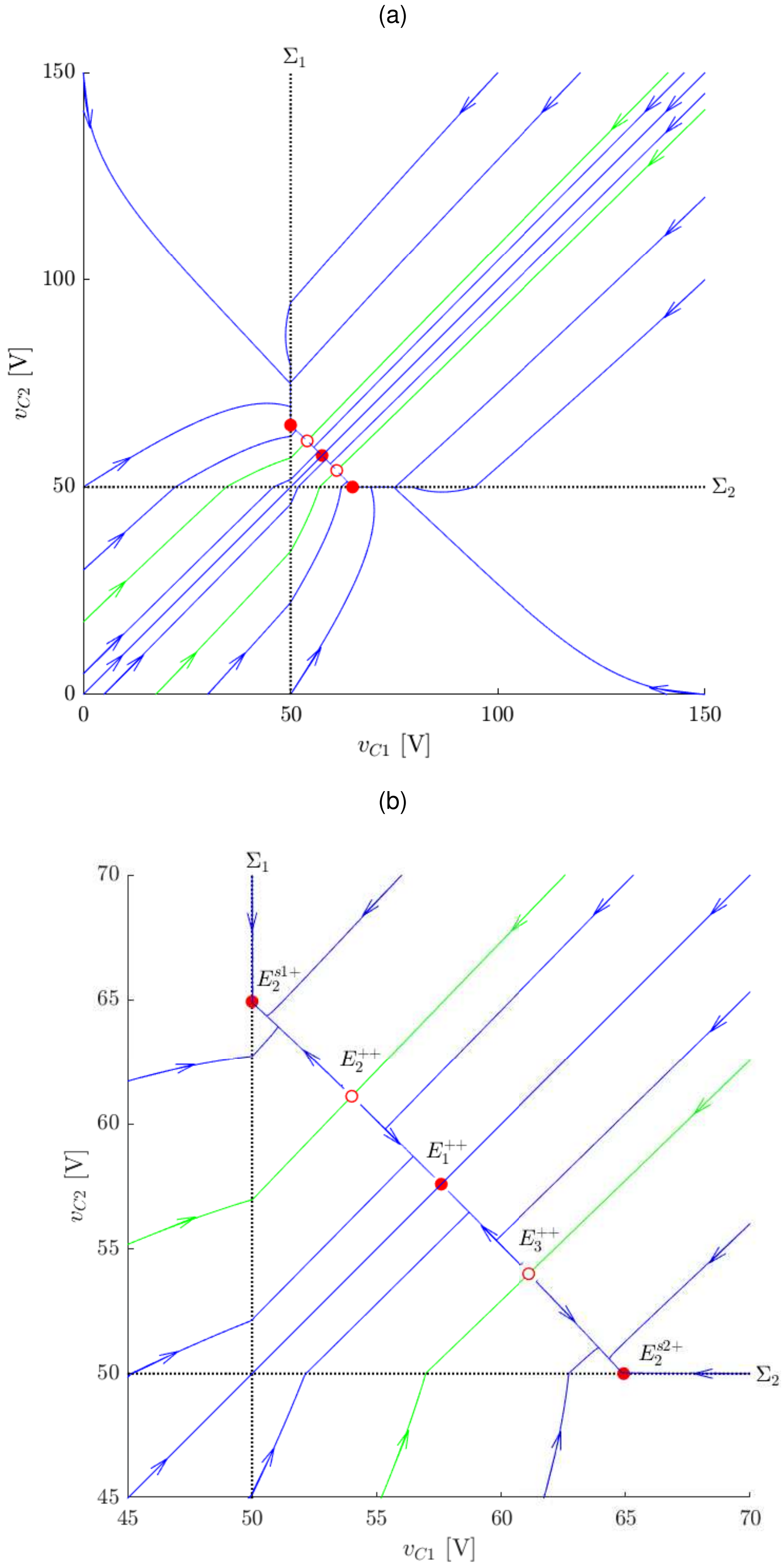

Source – Own Elaboration.

4.2.2 Variation of the capacitances C_i

In this session we test the influence of the variation of C_i. In some preliminary results, we have observed the following phenomenon: choosing random values for C_i within an uncertainty range around the nominal value, for a given range, the system started to malfunction, even though the value of R_b was theoretically sufficient to make the operating point stable. This was even one of the first motivations of this work. In chapter 3 we see that C_i does not influence for the nullcline, equilibrium or pseudo-equilibrium positions. It is also does not influence sliding regions or tangency points location, neither their classification. Here we explain with an example, how a given variation in C_i can lead the system to malfunction despite the operating point being stable.

The simulation is made with the parameters in Table 11. They are the same used in the local stable case of the previous section, except for the C_i values. Here, they were chosen as 1,2 and 0,8 of the nominal value C. These are the extremes of a usual manufacturing tolerance, and also the same we have in the capacitors of a real prototype in our facilities. The worst case scenario is chosen, that is, one capacitance in the maximum value and another in the minimum, so that they charge in different rates leading to a greater unbalance than other cases.

Table 11 – Circuit parameters for local stable case with varying capacitances for the two-submodule system. The balancing resistance R_b is designed so that $\gamma = 1,005$

N	V_{DC}[V]	$R[\Omega]$	C[mF]	$\frac{C_1}{C}$	$\frac{C_2}{C}$	P[W]	V_{Cmin}[V]	$R_b[\Omega]$
2	150	100	2,82	1,2	0,8	10	50	330,0512

Source – Own Elaboration.

As seen in (8), C_i multiplies the whole equation of a given state. This corresponds to a scaling in a given axis direction in the vector field. In Figure 38 we can see f vector field. The vectors are slighty more vertical position than in the previous case. The nullclines and equilibrium points remain in the same position. The eigenvectors associated with the equilibrium points, are also tilted towards the vertical (v_{C2}) direction, though (Table 12). This influences the trajectories and also, the assimptotes of $\boldsymbol{E_2^{++}}$ and $\boldsymbol{E_3^{++}}$, which determine the position of the attraction domain of $\boldsymbol{E_1^{++}}$.

In Figure 39 we can see that the attraction domain of $\boldsymbol{E_1^{++}}$ is tilted compared to the previous case, and, more importantly, the origin is out of it. In this phase plane figure, only the trajectory starting at the origin is plot. This corresponds to the trajectory of the real system, that should start with discharged capacitances. We can see that it reaches the pseudo-node $\boldsymbol{E_2^{s1+}}$ instead of $\boldsymbol{E_1^{++}}$, therefore, the system is not working as desired, even though $\boldsymbol{E}_1^{++}$ is stable.

Table 12 – Equilibrium points in $\boldsymbol{f}$ - coordinates, eigenvalues and eigenvectors of the linearized system around these equilibria for $\gamma = 1{,}005$.

Equilibrium Point	$(v_{C1}\ ;\ v_{C2})$	λ_1	λ_2	$\boldsymbol{v_1}$	$\boldsymbol{v_2}$
$\boldsymbol{E}_1^{++}$	(57,59 ; 57,59)	-0,00534	-7,393	[0,707 -0,707]^T	[0,554 0,832]^T
$\boldsymbol{E}_2^{++}$	(54,00 ; 61,11)	0,0106	-7,436	[0,720 -0,693]^T	[0,540 0,841]^T
$\boldsymbol{E}_3^{++}$	(61,11 ; 54,00)	0,0108	-7,235	[0,693 -0,720]^T	[0,569 0,822]^T
$\boldsymbol{E}_2^{s1+}$	(50,00 ; 64,92)	-	-	-	-
$\boldsymbol{E}_2^{s2+}$	(64,92 ; 50,00)	-	-	-	-

Source – Own Elaboration.

The corresponding time response can be seen in Figure 40. The voltages v_{C1} and v_{C2} diverge and unbalance (Figure 40 (a)). In the first instants (Figure 40 (b)), the discontinuous variation can be seen in $\frac{dv_{C1}}{dt}$ and in $\frac{dv_{C2}}{dt}$. In Figure 40 (c), we can see the voltage v_{C1} reaches the pseudo-equilibrium value of 50 V. In the real system, the system would be automatically shut down for safety reasons.

This concludes the example, that it is possible to have a stable operating point, and the system still not work as desired. Also, it is shown how the capacitances C_i take part in this phenomenon. In the chapter 6, a condition for guaranteeing global stability in a two SM system is presented and proved. The global stable system can work regardless of variation in the C_i values.

Figure 38 – $\boldsymbol{f}$ vector field for $\gamma = 1,005$, but also varying the capacitances. Domain $\mathbb{D}$ (a) and zoom near $\boldsymbol{E}_1^{++}$ (b).

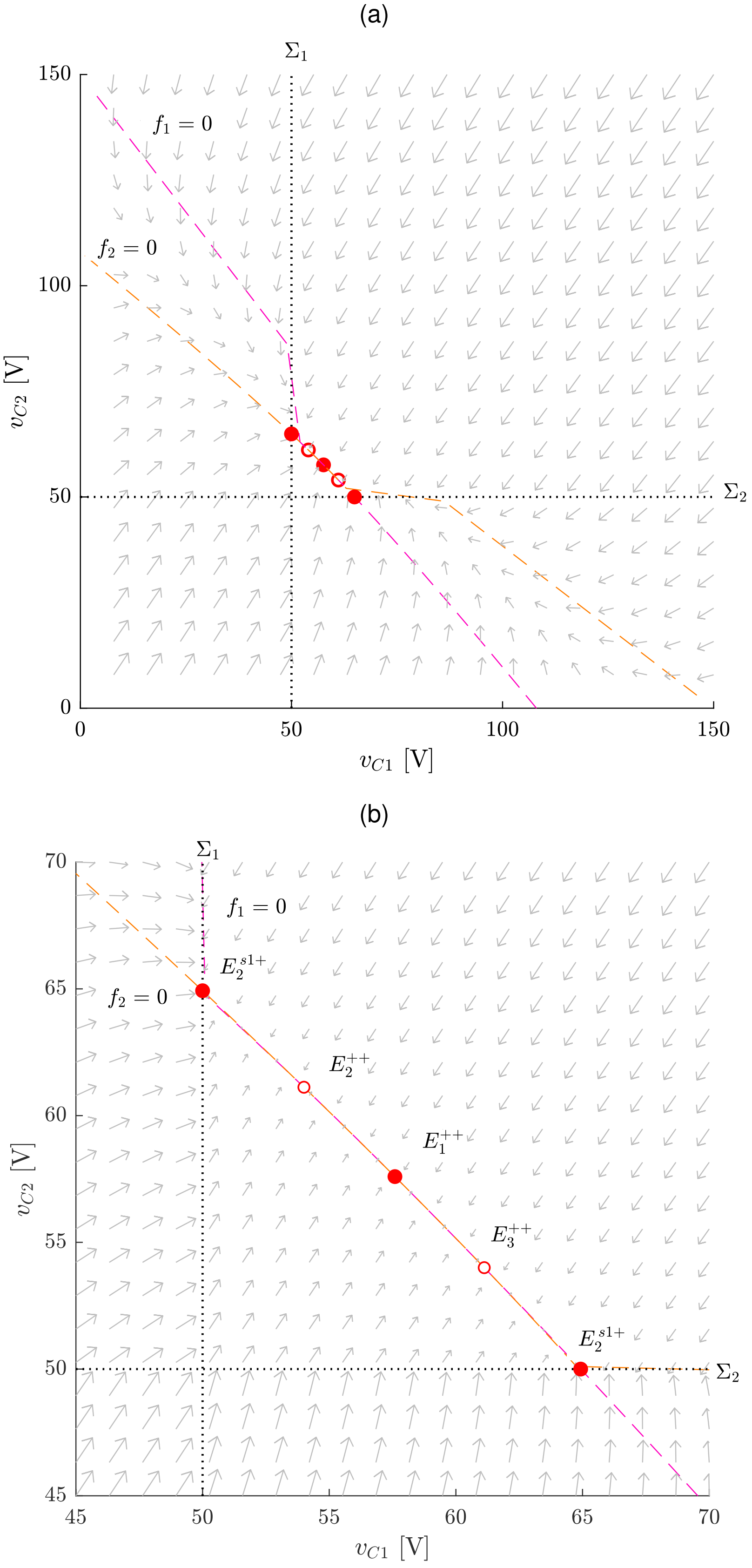

Source – Own Elaboration.

Figure 39 – $\boldsymbol{f}$ Trajectory starting at $v_{C0} = [0{,}001\ 0{,}001]^T$ in the phase plane, for $\gamma = 1{,}005$, but also varying the capacitances. Domain $\mathbb{D}$ (a) and zoom near $\boldsymbol{E}_{\mathbf{1}}^{++}$ (b).

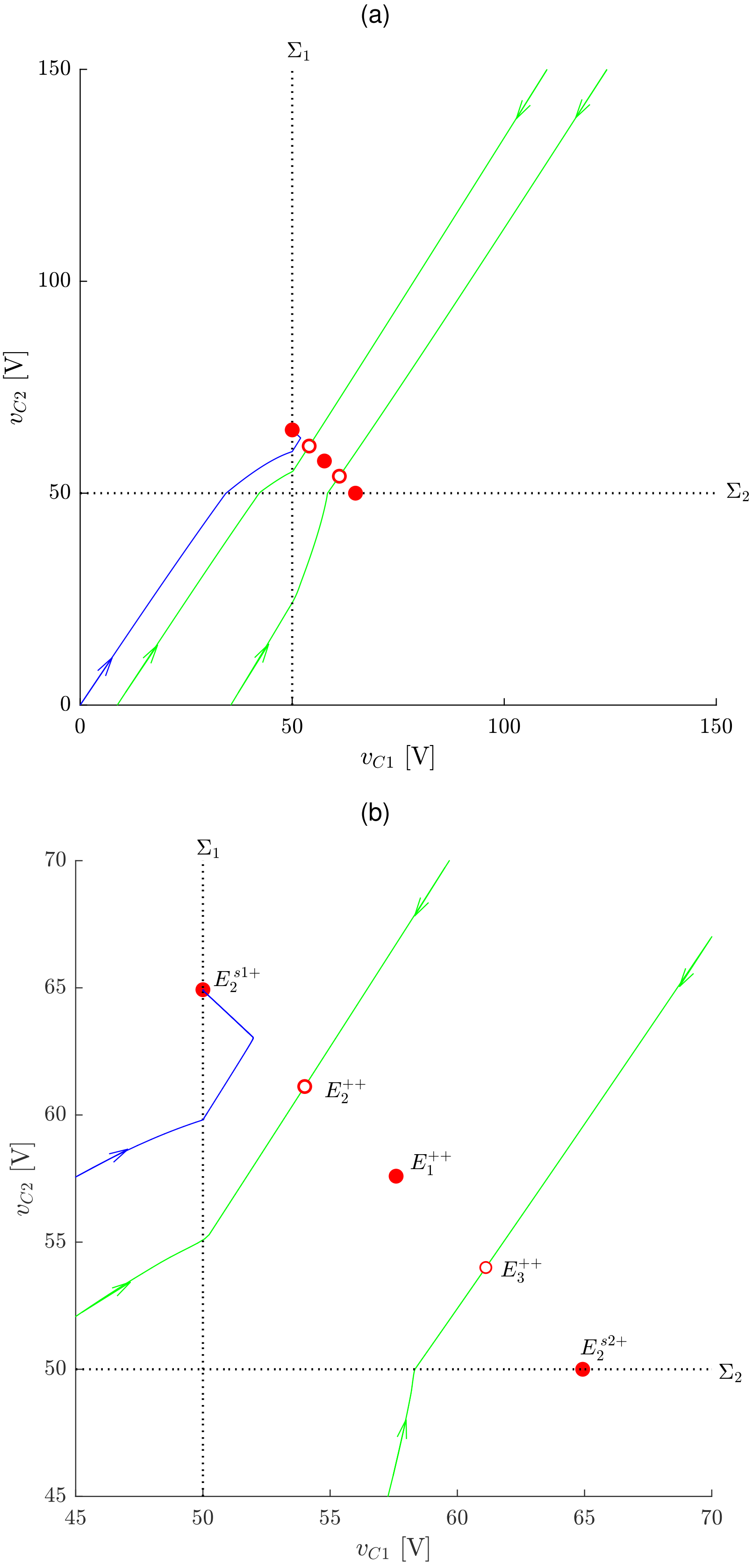

Source – Own Elaboration.

Figure 40 – *f* Time response at $v_{C0} = [0,001\ 0,001]^T$ for $\gamma = 1.005$, but also varying the capacitances. Whole time response (a), first instants (b) and zoom around pseudo-equilibrium voltage v_{C1} (c).

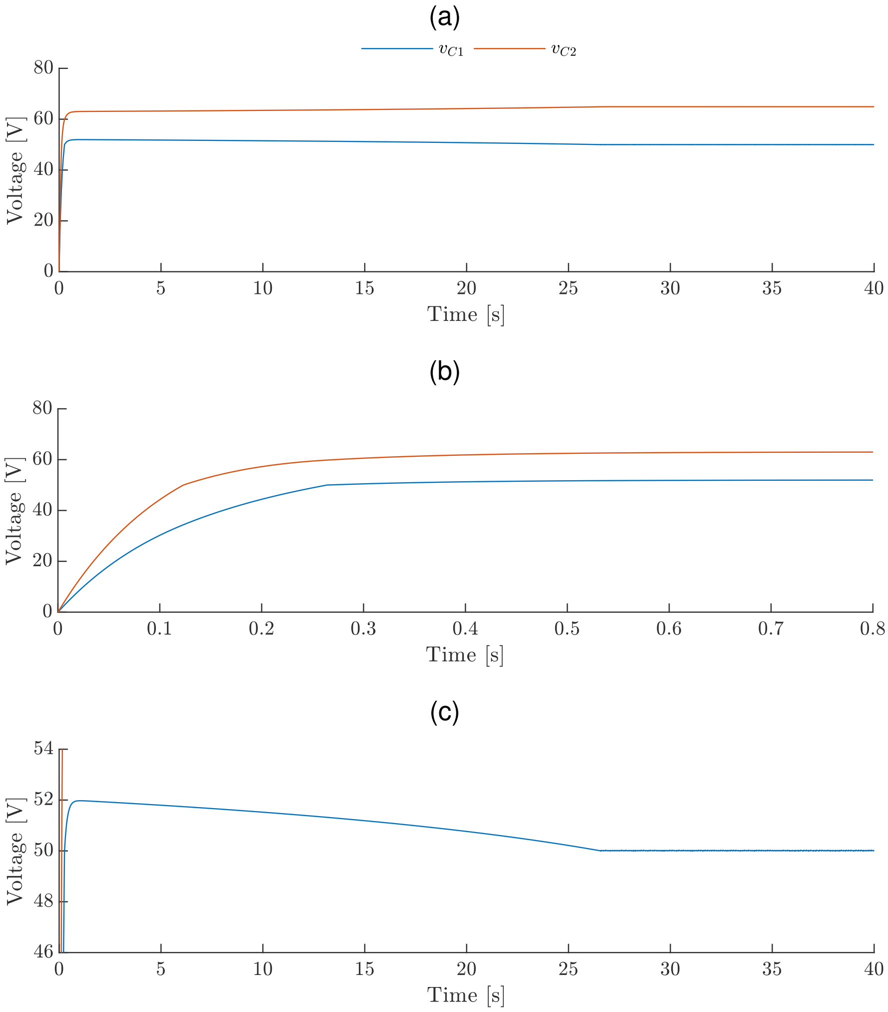

Source – Own Elaboration.

4.2.3 Variation of V_{Cmin}

Here we study the influence of V_{Cmin} variation in the system dynamics. Designing the system for a low V_{Cmin} value can bring some advantages. As it determines the points that the APS are turned on, a low value means that the system spends less time in the uncontrolled precharge stage, and can help in the system stability if an adequate control method is used in the controlled stage of the precharge. However, if the value is too low, it can lead to the system malfunction. We show in the following case how can that occur.

The parameter V_{Cmin} does not influence the position or stability of natural equilibrium points of $\boldsymbol{f}$. However, variations in this parameter may influence whether these equilibrium points are real or virtual[1]. Also, it influences the existence of pseudo-equilibrium points in Σ_1 and Σ_2. We simulate here a case of a V_{Cmin} value such as $\boldsymbol{E_4^{++}}$ is real. The simulation parameters are listed in Table 13.

The sliding regions of $\boldsymbol{f}$ can be seen in Figure 41. They cover a vast part of Σ_1 and Σ_2. The tangency points $\boldsymbol{T_1^-}$ and T_2^- are invisible folds in this case. Over these sliding regions, there are also real pseudo-equilibrium points in Σ_1 and Σ_2. We can see them in $\boldsymbol{f}$ vector field in Figure 42. In Figure 42 (b), we can see that there is a pseudo-equilibrium point, $\boldsymbol{E^{ss}}$, at the intersection of Σ_1^{as} and Σ_2^{as}. For the direction of the vector field, we can conclude that it is a stable pseudo-node, by looking at the vector field direction. This point is problematic.

As $\boldsymbol{E^{ss}}$ is a stable node, and there are no crossing regions around $\mathbb{D}_1$ in this case, the trajectories with initial conditions can only eventually reach $\boldsymbol{E^{ss}}$ and stay there. Therefore, the system can not reach its desired operating point. The phase portrait of $\boldsymbol{f}$ including these trajectories can be seen in Figure 43. A time response with initial conditions in $\mathbb{D}_1$ can be seen in Figure 44. The voltages rise up together but do not surpass the V_{Cmin} value of 5V. A real system may shut down because one of the capacitor voltages has reached an inferior safety threshold. Note also that all of it happens, even if the operating point $\boldsymbol{E^{++}}$ is stable (Table 14).

Table 13 – Circuit parameters for simulation of $\boldsymbol{f}$ such that $\boldsymbol{E_4^{++}}$ is real.

N	V_{DC}[V]	$R_l[\Omega]$	C[mF]	P[W]	V_{Cmin}[V]	$R_b[\Omega]$
2	150	100	2,82	10	5	250

Source – Own Elaboration.

---

[1] A virtual equilibrium point occur in the case of PWS systems, and it is an equilibrium point that is located outside the vector field in which this point are defined.

Figure 41 – f sliding regions for the case in which $\boldsymbol{E_1^{++}}$ is real.

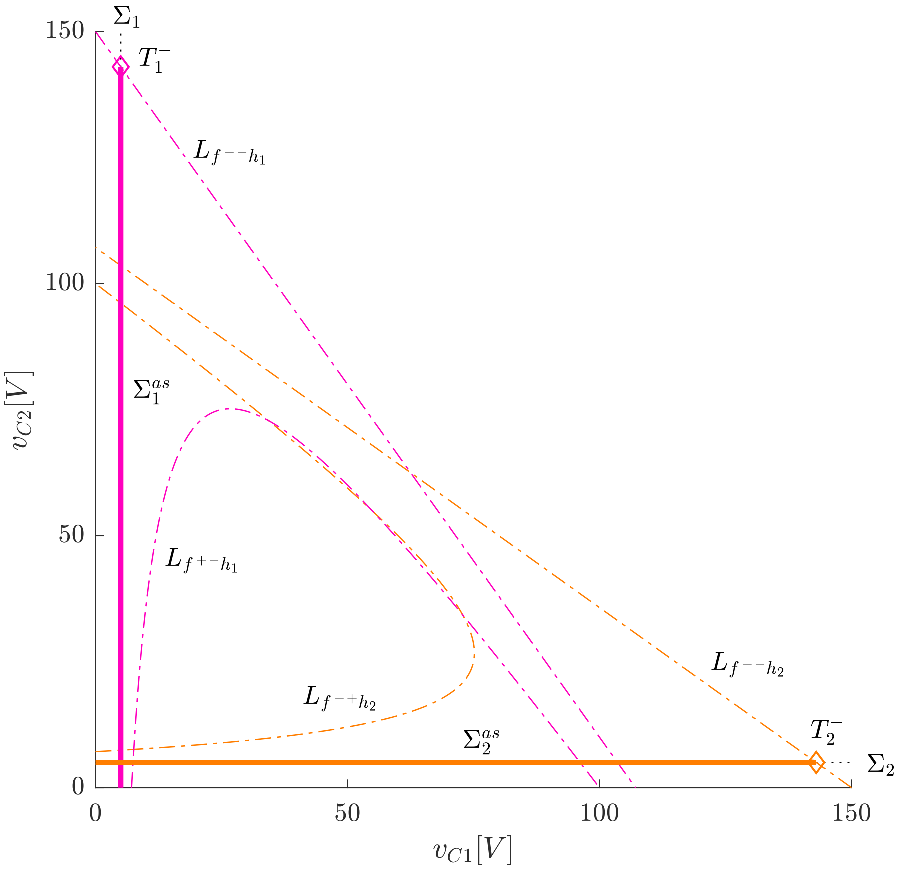

Source – Own Elaboration.

That concludes the example showing how a V_{Cmin} poorly designed can lead to the system malfunctioning, even with a local stable operating point. Another choice of V_{Cmin} that would lead the system to malfunction would be $V_{Cmin} > E_{11}^{++}$. In that way, the operating point $\boldsymbol{E_1^{++}}$ is virtual, and it is not possible to reach it. This concludes the example as well as the simulation results of this work.

Table 14 – Equilibrium points in f - coordinates, eigenvalues and eigenvectors of the linearized system around these equilibria for $\gamma \approx 1,2$.

Equilibrium Point	$(v_{C1}\ ;\ v_{C2})$	λ_1	λ_2	$\boldsymbol{v_1}$	$\boldsymbol{v_2}$
$\boldsymbol{E_1^{++}}$	(54,912 ; 54,912)	-7,334	- 0,2424	$[0,707\ 0,707]^T$	$[-0,707\ 0,707]^T$
$\boldsymbol{E_2^{++}}$	(72,804 ; 34,338)	-6,860	0.6075	$[-0.810\ -0,586]^T$	$[0,586\ 0,810]^T$
$\boldsymbol{E_3^{++}}$	(34,338 ; 72,804)	0.607	- 6,860	$[0.810\ -0,586]^T$	$[0,586\ 0.810]^T$
$\boldsymbol{E_4^{++}}$	(7,587 ; 7,587)	53,079	60,171	$[-0,707\ -0,707]^T$	$[-0,707\ 0,707]^T$
$\boldsymbol{E_1^{s1+}}$	(5,000 ; 7.429)	-	-	-	-
$\boldsymbol{E_2^{s1+}}$	(5,000 ; 96.141)	-	-	-	-
$\boldsymbol{E_1^{s2+}}$	(7.429 ; 5,000)	-	-	-	-
$\boldsymbol{E_2^{s2+}}$	(96.141 ; 5,000)	-	-	-	-
$\boldsymbol{E^{ss}}$	(5,000 ; 5,000)	-	-	-	-

Source – Own Elaboration.

Figure 42 – Vector field $\boldsymbol{f}$ such that $\boldsymbol{E_4^{++}}$ is real. Domain $\mathbb{D}$ (a) and zoom near $\boldsymbol{E_4^{++}}$ (b).

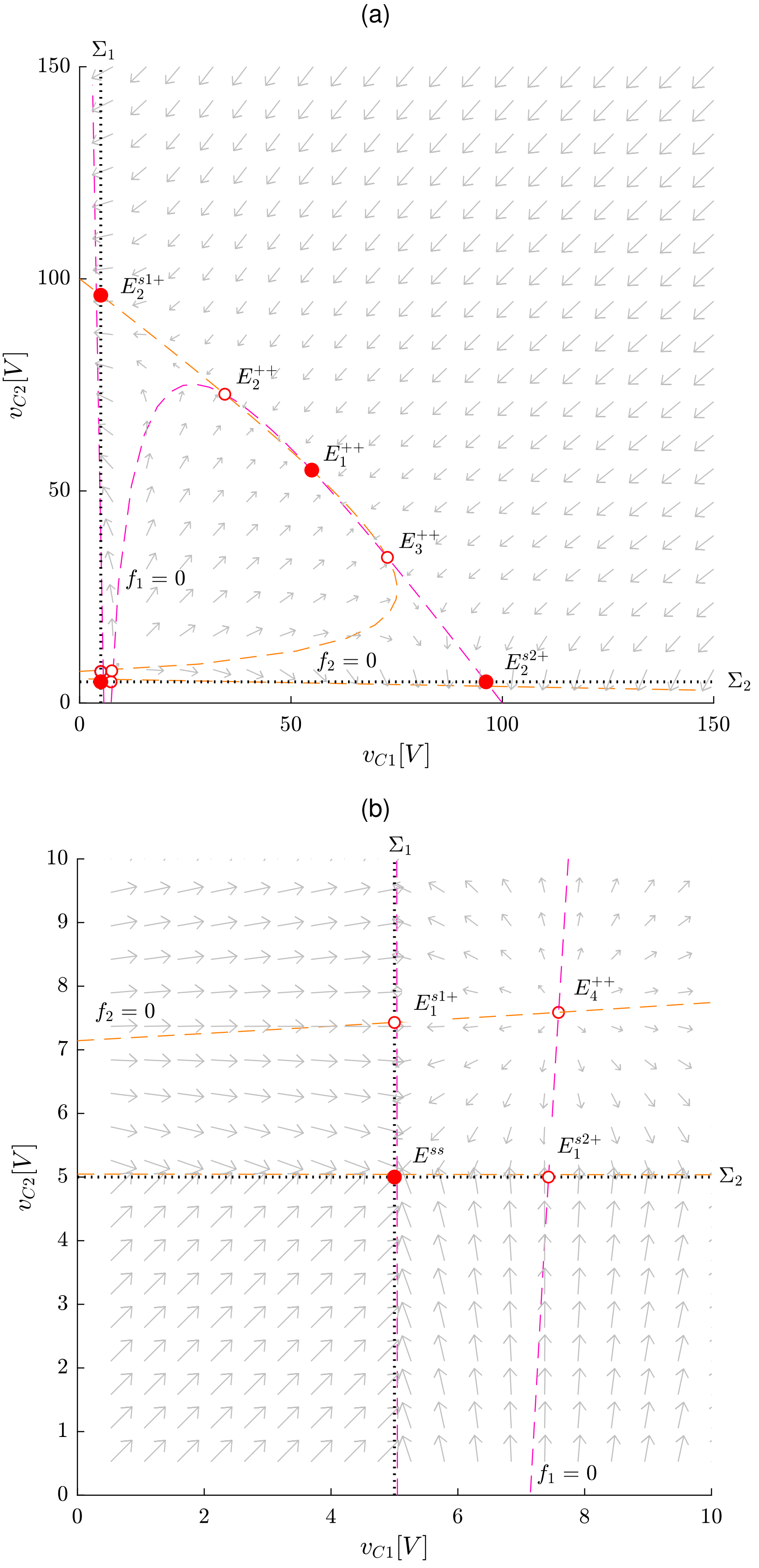

Source – Own Elaboration.

Figure 43 – Phase Portrait of $\boldsymbol{f}$ such that $\boldsymbol{E_4^{++}}$ is real. Domain $\mathbb{D}$ (a) and zoom near $\boldsymbol{E_4^{++}}$ (b).

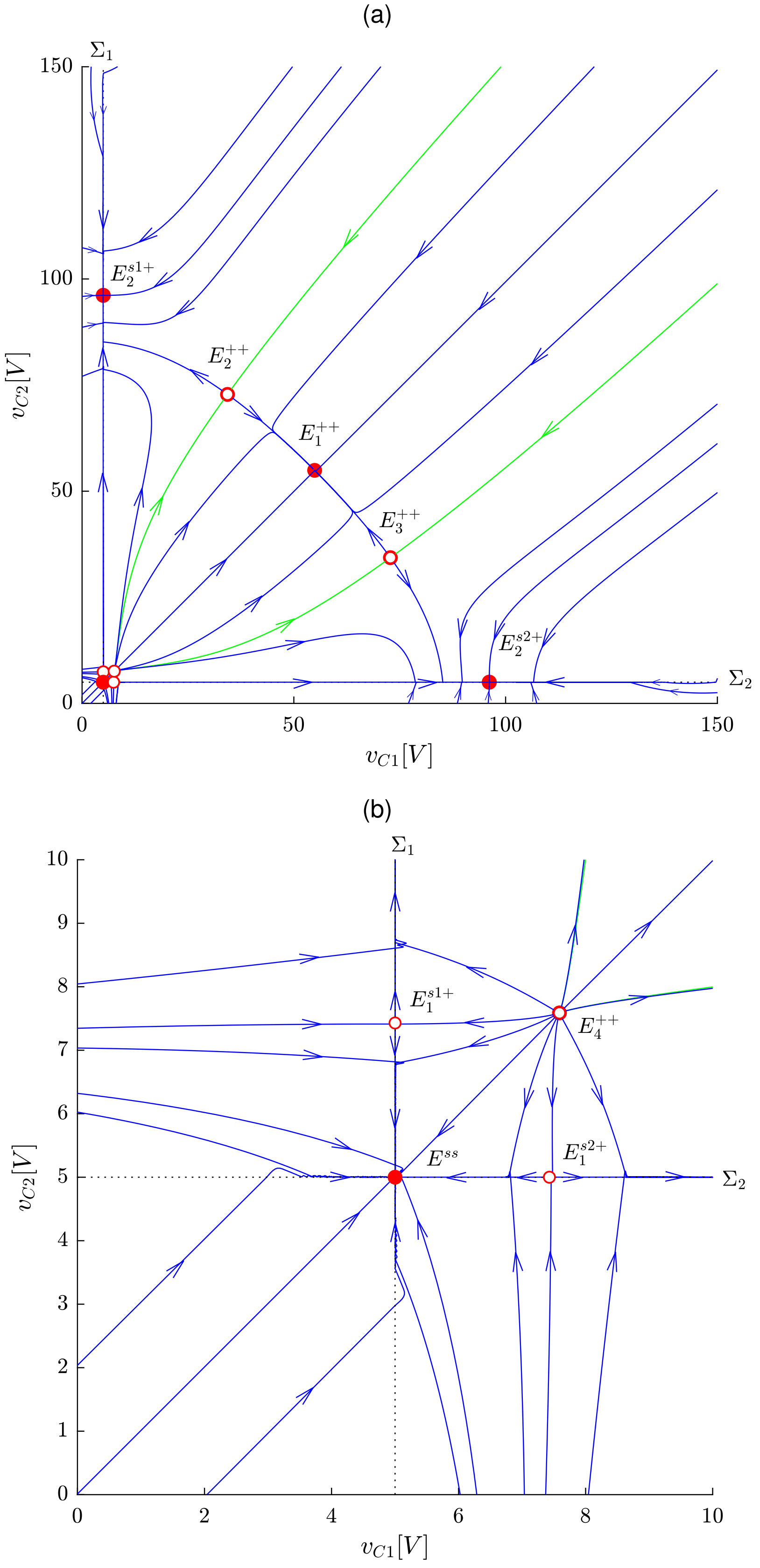

Source – Own Elaboration.

Figure 44 – A time response of $\boldsymbol{f}$ such that $\boldsymbol{E}_4^{++}$ is real.

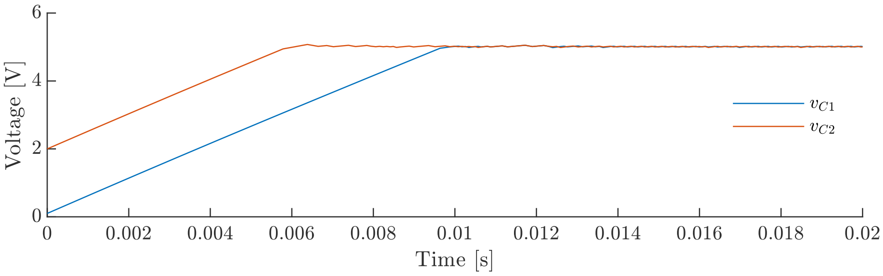

Source – Own Elaboration.

4.3 SUMMARY

In this chapter, we have seen:

- Vector fields, phase portraits and time responses of f^{--}, f^{-+} and f^{++} were simulated, in order to help understand the dynamics in each of these fields separately.
- The vector field f was simulated in order to better understand the interaction between f^{--}, f^{-+}, f^{+-} and f^{++} as well as the dynamics in Σ_1 and Σ_2.
- The simulations were made for a nominal case, where the SM parameter values are equal and $\boldsymbol{E}_{\mathbf{1}}^{++}$ is stable.
- The influence of parametric variation in the system dynamics was also investigated. Variations in R_b, C_i and in V_{Cmin} were studied.
- Regarding the variation of R_b, it was shown a case where $\boldsymbol{E}_{\mathbf{1}}^{++}$ is unstable. Also, The variation of the attraction domain of $\boldsymbol{E}_{\mathbf{1}}^{++}$ and f^{++} bifurcation diagram. It is shown that a saddle-node and also to sub-critical pitchfork bifurcations occur when R_b varies. Regarding f, the variation of R_b can result in an unstable, local stable or even global stable $\boldsymbol{E}_{\mathbf{1}}^{++}$.
- With respect to the variation of C_i, although it does not change the nullclines or equilibrium points position and classification, it does distort the vector field. In a local stable case, it can move the attraction domain away from the null initial condition, which is the one used in a real case. This causes the system not to reach the operating point, leading to malfunction.
- Regarding the variation of V_{Cmin}, it is shown that either if it is chosen so that $\boldsymbol{E}_{\mathbf{1}}^{++}$ is virtual, or such that $\boldsymbol{E}_{\mathbf{4}}^{++}$ is real, it causes the system to malfunction. The first case, because the operating point becomes virtual, thus not reachable, and the second, because the stable-pseudo node $\boldsymbol{E}^{ss}$ in the intersection of Σ_1^{as} and Σ_2^{as} becomes real, and the system trajectories with initial conditions in $\mathbb{D}_1$ (with all APS turned off) eventually all converge to $\boldsymbol{E}^{ss}$.

In the next chapter, experimental results show an example of the proposed solution being effective in a real case. The insights learned from the simulations are used to find an analytical condition for the global stability of a system with two SM in chapter 6.

5 EXPERIMENTAL RESULTS

Experiments were conducted on a prototype with ten SM per phase, whose photo can be seen in Figure 46. This prototype was already present in the university facilities. The experiments exemplify a case in which the proposed solution was effective. The same circuit was tested with and without the balancing resistances R_b. The circuit parameter values are shown in Table 15. Note that the parameter values used in the simulations in the previous chapter were made based on this prototype parameter values - only the voltage V_{DC} was reduced so that the operating point voltage matches the prototype's. There are uncertainties associated with the capacitance values, as well as in the power consumed by the APSs of the communication and control circuits. The power P in the table is actually the average value of P_i, calculated for power dissipations in the range $[11.37, 14.3]$ W. The balancing resistance R_b value was chosen for a $\gamma \approx 1,2$.

The experiments results can be seen in Figure 45. In the first stage of the precharge operation, the auxiliary power supplies are still not turned on, and therefore the v_{Ci} are not measured. They appear as null, but that does not correspond to their real value. Because the submodules don't have identical parameter values, each auxiliary power supply turns on at a different time instant. In Figure 45 (a), one can see that the voltages tend to diverge and unbalance. That happens until one of the values reach a minimum or maximum voltage threshold value and then the circuit is all turned off for safety reasons.

In Figure 45 (b), it is shown a case in which the balancing resistance is used. The capacitor voltages converge to a stable operating point. In this point, the voltages are not equal, and spread in the range $[65.3, 73.2]$ V ([-6.4%, +4.8%] in respect to average), corresponding to calculated power dissipations in the range $[11.37, 14.3]$ W. Standard deviation in steady state is $\sigma_{\text{ss}} = 3.2\%$. The unbalance in v_{Ci} values is likely caused by the dispersion in values of P_i and R_b and further uncertainties in the measurements, which are obtained from the own submodule acquisition system based on a microcontroller (SCHMIDT et al., 2019).

Table 15 – Circuit parameters for the experimental case. R_b was tested in open circuit $R_b \to \infty$ and $R_b = 375\ \Omega$.

Experiment	N	V_{DC}[V]	$R_l[\Omega]$	C[mF]	P[W]	$R_b[\Omega]$	γ
1	10	740	$100\ \pm 5\%$	$2.82\ \pm 20\%$	10,74	$\to \infty$	$\to 0$
2	10	740	$100\ \pm 5\%$	$2.82\ \pm 20\%$	10,74	375	1,2

Source – Schmidt et al. (2019).

Figure 45 – Experimental results for the (a) precharge without balancing and (b) with passive balancing ($R_b = 375\ \Omega$).

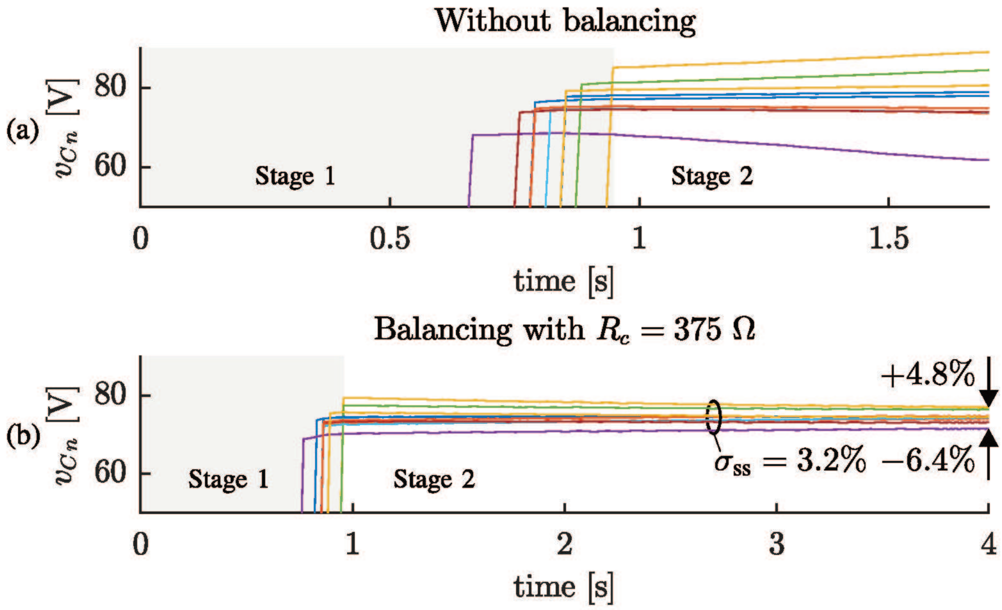

Source – Schmidt et al. (2019).

Figure 46 – Photograph of the MMC prototype used in this work.

Source – Schmidt et al. (2019).

5.1 SUMMARY

In this chapter we have seen:

- An experiment was conducted showing a real case that illustrates the unbalancing of the capacitor voltages problem, and the effectiveness of the proposed solution.
- There is some deviation in the capacitor voltages, caused by differences of power consumption in each APS. Nevertheless, the operating point is stable and the system reaches it, keeping the voltages constant.

In the next chapter, analytical conditions for global stability of a system with 2 SM are shown and proved.

6 GLOBAL STABILITY IN THE PLANAR CASE

In this chapter we show conditions that guarantee global stability of the operating point in the two SM sytem presented in chapter 3. In the section 6.1 we present the conditions and present the system vector field in the case the conditions are satisfied and show by a qualitative analysis that the operating point is globally asymptotically stable. In the next sections, we prove that the field has the configuration presented in section 6.1. In 6.2 we prove that the analyzed domain is positively invariant, in 6.3 we prove that the dynamics on the switching boudaries are as presented in section 6.1 and in 6.4 we prove that the operating is the only real equilibrium point, as presented in section 6.1 if the conditions are satisfied. Finally, we propose guidelines for the design of R_b section 6.5 based on the stability conditions. The section 6.6 is a summary of this chapter.

6.1 A PICTURE OF THE GLOBALLY STABLE OPERATING POINT VECTOR FIELD

If the operating point $\boldsymbol{E}_{\mathbf{1}}^{++}$ is stable and real, and the saddle points $\boldsymbol{E}_{\mathbf{2}}^{++}$ and $\boldsymbol{E}_{\mathbf{3}}^{++}$ are virtual, then the operating point is globally stable. We consider $\mathbb{D}$, as given by (19):

$$\mathbb{D} = \{(v_{C1}, v_{C2}) \in \mathbb{R}^2 : 0 < v_{C1} \leq V_{DC} \text{ and } 0 < v_{C2} \leq V_{DC}\}.$$

We prove that any trajectory with initial conditions in any place inside $\mathbb{D}$, will asymptotically converge to $\boldsymbol{E}_{\mathbf{1}}^{++}$, if the conditions (61) (the condition for local stability of $\boldsymbol{E}_{\mathbf{1}}^{++}$) and (77), namely

$$\begin{aligned} &\frac{V_{Cb}^2}{R_b} > P, \\ &E_{21}^{++} < V_{Cmin} < E_{11}^{++}, \end{aligned} \tag{77}$$

are satisfied.

We look at the general picture of $\boldsymbol{f}$ satisfying conditions (61) and (77). We can see that, wherever in $\mathbb{D}$ (Figure 47) is the initial condition, the trajectory starting in it asymptotically converges to $\boldsymbol{E}_{\mathbf{1}}^{++}$. In the next sections, it is proved that the vector field has the characteristics depicted in Figure 48 and its phase portrait is topologically equivalent to the one shown in Figure 49.

Figure 47 – Domain $\mathbb{D} = \mathbb{D}_1 \cup \mathbb{D}_2 \cup \mathbb{D}_3 \cup \mathbb{D}_4 \cup \Sigma_1 \cup \Sigma_2$

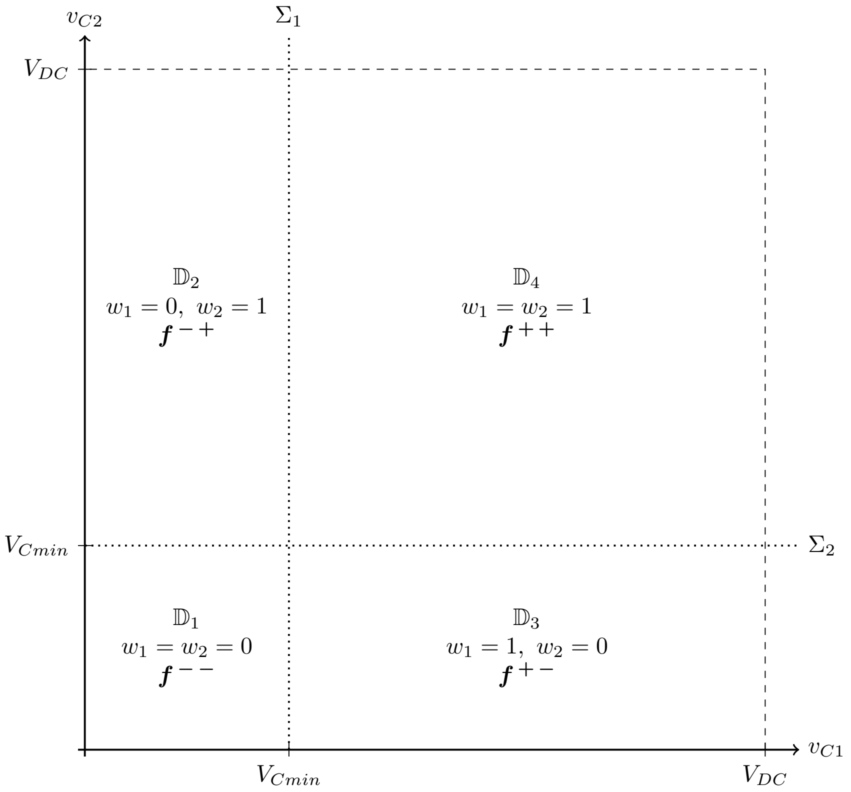

Source – Own Elaboration.

Take any trajectory in $\mathbb{D}_1$. The vector field $\boldsymbol{f}^{--}$ governs this domain, and its equilibrium, $\boldsymbol{E}^{--}$, is virtual. The trajectory is attracted to the virtual equilibrium point, and can cross to $\mathbb{D}_2$, $\mathbb{D}_3$ or even to $\mathbb{D}_4$, as there are only crossing regions in the boundaries Σ_1^- and Σ_2^-.

If the trajectory is in $\mathbb{D}_2$, where $\boldsymbol{f}^{-+}$ governs, it tends to go towards the v_{C1} axis as seen in the previous chapter. It can either cross directly to $\mathbb{D}_4$ or to slide in Σ_1^{as} and go out of it through the invisible fold $\boldsymbol{T_1^+}$ and then go to $\mathbb{D}_4$. Analogously, the same occurs in $\mathbb{D}_3$: trajectories in there can either cross directly to D_4 or slide in Σ_{2as} and then cross to $\mathbb{D}_4$ when they reach the visible fold $\boldsymbol{T_2^+}$. Figure 49 shows an example of a phase portrait of $\boldsymbol{f}$ in which that happens.

Finally, in $\mathbb{D}_4$, the trajectories also all end up converging to $\boldsymbol{E_1^{++}}$. They can directly converge to $\boldsymbol{E_1^{++}}$, or converge to Σ_1^{as} or Σ_2^{as} and slide until reach the respective visible fold $\boldsymbol{T_1^+}$ or $\boldsymbol{T_2^+}$ and then converge to $\boldsymbol{E_{++,1}}$ or yet, cross to $\mathbb{D}_2$ or $\mathbb{D}_3$. Note that the trajectories entering $\mathbb{D}_4$ through one of the visible folds or through a crossing point does not touch the switching boundary anymore, for it converges to $\boldsymbol{E_1^{++}}$, which is a stable node. Therefore, the system is globally stable. In the next sections, it is proved that the vector field has the characteristics illustrated in Figure 48.

Figure 48 – Vector field $\boldsymbol{f}$ satisfying the global stability conditions.

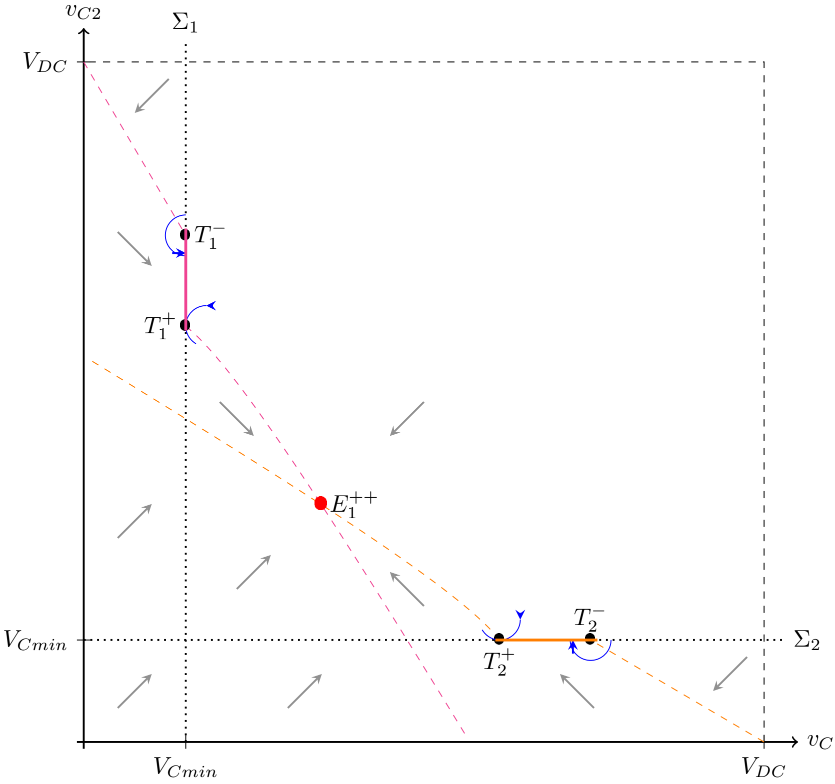

Source – Own elaboration.

Figure 49 – A phase portrait example with the globally stable operating point.

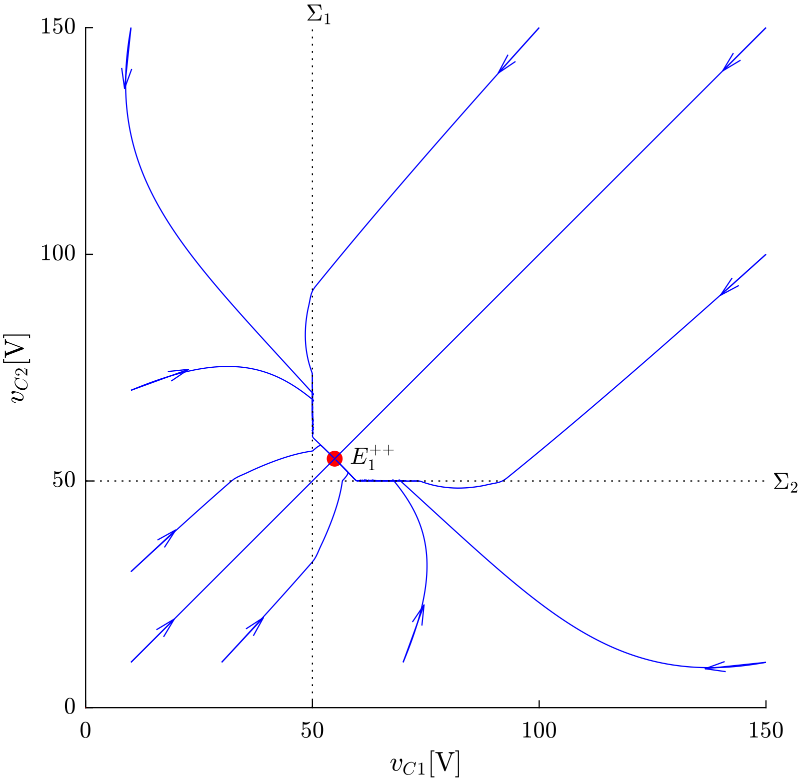

Source – Own elaboration.

6.2 OUTER BOUNDARIES: D IS POSITIVELY INVARIANT

We will show that the domain $\mathbb{D}$ is positively invariant. That means: any trajectories that start within $\mathbb{D}$, will remain inside it for all positive time. This means that for any initial condition inside $\mathbb{D}$, it is always valid that $0 \leq v_{C1} \leq V_{DC}$, and also $0 \leq v_{C2} \leq V_{DC}$.

We look at the vector field over the axis v_{C2}. We have

$$\begin{aligned} \left.\frac{dv_{C1}}{dt}\right|_{\boldsymbol{v_C}=(0,v_{C2})} &= \left.\left(\frac{V_{DC}-(v_{C1}+v_{C2})}{R_l}-\frac{v_{C1}}{R_b}\right)\right|_{\boldsymbol{v_C}=(0,v_{C2})}. \\ &= V_{DC}-v_{C2} > 0. \end{aligned}$$

This holds true for $0 \leq v_{C2} < V_{DC}$. However, for $v_{C2} = V_{DC}$, we have:

$$\begin{aligned} \left.\frac{dv_{C2}}{dt}\right|_{\boldsymbol{v_C}=(0,V_{DC})} &= \left.\left(\frac{V_{DC}-(v_{C1}+v_{C2})}{R_l}-\frac{P}{v_{C2}}-\frac{v_{C2}}{R_b}\right)\right|_{\boldsymbol{v_C}=(0,V_{DC})}. \\ &= -\frac{P}{v_{C2}}-\frac{V_{DC}}{R_c} < 0. \end{aligned}$$

So no trajectory will leave $\mathbb{D}$ through the v_{C2} axis. The same happens over the v_{C1} axis, in analogous form. In the upper boundary $v_{C2} = V_{DC}$, we have $\frac{dv_{C1}}{dt} = 0$ and:

$$\left.\frac{dv_{C2}}{dt}\right|_{\boldsymbol{v_C}=(v_{C1},V_{DC})} = -\frac{v_{C1}}{R_l}-\frac{V_{DC}}{R_b}-\frac{P}{V_{DC}} < 0.$$

So no trajectory will leave $\mathbb{D}$ through $v_{C2} = V_{DC}$. The same happens in analogous form for $v_{C1} = V_{DC}$.

Therefore, $\mathbb{D}$ is positively invariant. Now that we know what happens in the outer boundaries of $\mathbb{D}$, we can look at what happens in the inner boundaries Σ_1 and Σ_2 in the next section.

6.3 DYNAMICS IN Σ_1 AND Σ_2

In chapter 3, it was already studied the dynamics of Σ_1. Some of them are parameter dependent, and other not. Here we investigate what happens in Σ_1 and Σ_2 in the case our hypothesis (61) and (77) are true. As the equations have similar form and symmetry in relation to $v_{C1} = v_{C2}$, what happens for Σ_1 also happens in Σ_2. Therefore, we show the results only in Σ_1, knowing that in Σ_2 the same happens.

Crossing And Sliding Regions in Σ_1

These are already studied in chapter 3, and are such as Figure 50. The coordinates of the tangency points are

$$\begin{aligned} \boldsymbol{T_1^-} &= (T_{11}^-, T_{12}^-) = \left(V_{Cmin}, V_{DC}-\frac{V_{Cmin}(R_l+R_b)}{R_b}\right), \\ \boldsymbol{T_1^+} &= (T_{11}^+, T_{12}^+) = \left(V_{Cmin}, V_{DC}-\frac{PR_l}{V_{Cmin}}-\frac{V_{Cmin}(R_l+R_b)}{R_b}\right). \end{aligned}$$

Figure 50 – Crossing and sliding regions in Σ_1^{as}. Vector field $\frac{v_{C1}}{dt}$ components are drawn in gray.

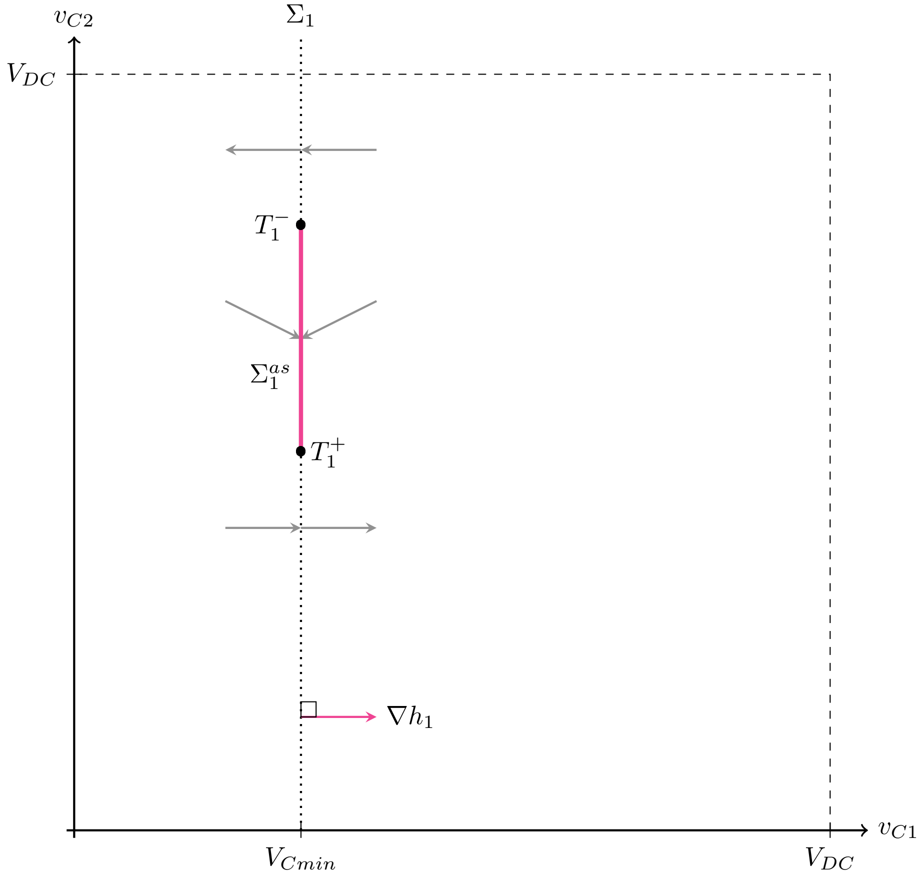

Source – Own Elaboration.

Dynamics in Σ_1^{as}

As ilustrated in Figure 48, $\boldsymbol{T_1^-}$ is an invisible fold and $\boldsymbol{T_1^+}$ is a visible fold and there are no real pseudo equilibrium points in Σ_1^{as}. We check if $\boldsymbol{T_1^-}$ and $\boldsymbol{T_1^+}$ belong to Σ_1^- or to Σ_1^+, because that is needed to classify them. We prove that both points belong to Σ_1^+.

If $\boldsymbol{T_1}^+ \in \Sigma_1^+$, then $\boldsymbol{T_1}^- \in \Sigma_1^+$, because $T_{12}^- > T_{12}^+$ and therefore, $\Sigma_1^{as} \in \Sigma_1^+$. Checking if $\boldsymbol{T_1^+} \in \Sigma_1^+$, we have:

$$T_{12}^+ = V_{DC} - \frac{PR_l}{V_{Cmin}} - \frac{V_{Cmin}(R_l+R_b)}{R_b} > V_{Cmin},$$

that, provided that $V_{Cmin} \neq 0$, is equivalent to

$$-(R_l+2R_b)V_{Cmin}^2 + V_{DC}R_bV_{Cmin} - PR_lR_b > 0. \tag{78}$$

Studying the signal of (78) as a function of V_{Cmin}, we see that

$$\frac{V_{DC}R_b - \sqrt{V_{DC}^2R_b^2 - 4PR_lR_b(R_l+2R_b)}}{2(R+R_b)} < V_{Cmin} < \frac{V_{DC}R_b + \sqrt{V_{DC}^2R_b^2 - 4PR_lR_b(R_l+2R_b)}}{2(R_l+R_b)},$$

which can be rewritten as, according to (47) and (48),

$$E_{21}^{++} < V_{Cmin} < E_{31}^{++}. \tag{79}$$

The initial hypothesis (77) satisfies (79) because $E_{11}^{++} < E_{31}^{++}$, thus $\boldsymbol{T_1^+} \in \Sigma_1^+$ and $\boldsymbol{T_1^-} \in \Sigma_1^+$.

Now we prove that T_1^- is an invisible fold. We can do that by calculating $L_{f^{-+}h_1}^2\Big|_{v_C=\boldsymbol{T_1^-}}$[1]. If it is an invisible fold, we have

$$L_{f^{-+}h_1}^2\Big|_{v_C=\boldsymbol{T_1^-}} > 0.$$

That is

$$-\frac{1}{C_1C_2R_b}\left(\frac{PR_b^3}{R_l(R_l+R_b)V_{Cmin}-R_lR_bV_{DC}}+\frac{(2R_b+R_l)V_{Cmin}}{R_l}-\frac{R_bV_{DC}}{R_l}\right)>0, \tag{80}$$

that can be rearranged as

$$-\frac{(R_l+2R_b)}{C_1C_2R_bR_l}\left(\frac{\dfrac{R_b^3P}{(R_l+R_b)(R_l+2R_b)}}{V_{Cmin}-\dfrac{V_{DC}R_b}{R_l+R_b}}+V_{Cmin}-\frac{V_{DC}R_b}{R_l+2R_b}\right)>0. \tag{81}$$

That is true because

$$V_{Cmin} < \frac{V_{DC}R_b}{R_l+2R_b} < \frac{V_{DC}R_b}{R_l+R_b}.$$

We know that because our initial hypothesis states that $V_{Cmin} < E_{11}^{++}$. Also

$$V_{Cmin} < E_{11}^{++} < E_1^{--}. \tag{82}$$

We can see it by substituting (46) and (29) in (82), which results in:

$$V_{Cmin} < \frac{R_bV_{DC}+\sqrt{R_b^2V_{DC}^2-4PR_lR_b(R_l+2R_b)}}{2(R_l+2R_b)} < \frac{V_{DC}R_b}{R_l+2R_b}.$$

Therefore the inequality (81) is true, and $\boldsymbol{T_1^-}$ is an invisible fold.

Finally, we prove that both $\boldsymbol{T_2^+}$ is a visible fold and there are no pseudo-equilibrium points in Σ_1^{as}. This situation fits a kind of local boundary saddle bifurcation cataloged. This bifurcation is a catastrophic disappearance of a stable pseudo-node and it is cataloged as the boundary saddle BS_2 case in (KUZNETSOV; RINALDI; GRAGNANI, 2003), seen in Figure 51.

In this bifurcation, if $V_{Cmin} < E_{21}^{++}$, $\boldsymbol{E_2^{++}}$ is real, $\boldsymbol{T_1^+}$ is an invisible fold and there is the real stable pseudo-node $\boldsymbol{E_2^{s1+}}$ in Σ_1^{as}, [2]. In the critical parameter value $V_{Cmin} = E_{21}^{++}$,

---

[1] The second order Lie derivative of a scalar function h in respect to a vector field f is given by $L_f^2h = \langle \nabla L_fh, f\rangle$

[2] This case is exemplified in chapter 4 in Figure 37.

these three points collide. When $V_{Cmin} > E_{21}^{++}$, that is our hypothesis, $\boldsymbol{E_2^{s1+}}$ and $\boldsymbol{E_2^{++}}$ become virtual, and $\boldsymbol{T_1^+}$ becomes a visible fold. The pseudo-saddle $\boldsymbol{E_1^{s1+}}$ is virtual, because, recalling:

$$E_{12}^{s1+} < E_{22}^{s1+} < T_{12}^{+},$$

therefore, $\boldsymbol{E_1^{s1+}} \notin \Sigma_1^{as}$ as well.

Figure 51 – Bifurcation of a saddle point X_α with a boundary Σ. In case BS_2, a saddle X_α coexists with an invisible tangent point T_{alpha} and a stable pseudo-node P_α for $\alpha < 0$, while only a visible tangent point T_α remains for $\alpha > 0$. This is a catastrophic disappearance of a stable pseudo-node.

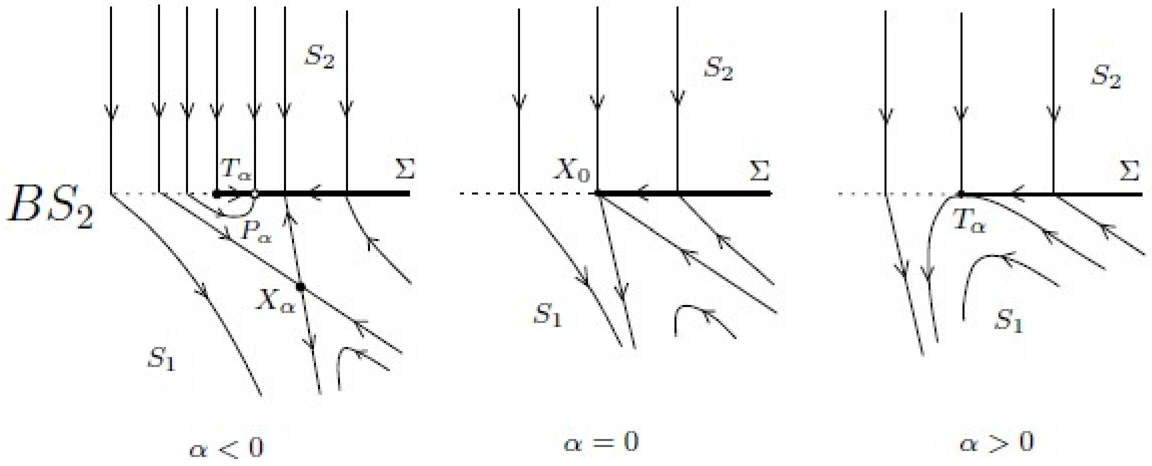

Source – Kuznetsov, Rinaldi, and Gragnani (2003).

6.4 EQUILIBRIUM POINTS IN $\mathbb{D}_1$, $\mathbb{D}_2$ AND $\mathbb{D}_4$

Now we prove that, as in Figure 48, there are no real equilibrium points in $\mathbb{D}_1$, $\mathbb{D}_2$ (consequently in $\mathbb{D}_3$) and that $\boldsymbol{E_1^{++}}$ is the only real equilibrium point in $\mathbb{D}_4$.

Equilibrium points in $\mathbb{D}_1$

In $\mathbb{D}_1, \boldsymbol{f^{--}}$ actuates, which has only the equilibrium $\boldsymbol{E^{--}}$. If $\boldsymbol{E_1^{++}}$ is real, then $\boldsymbol{E^{--}}$ is virtual:

$$V_{Cmin} < E_{11}^{++} < E_1^{--}.$$

We can see it by substituting E_{11}^{++} and E_1^{--} according to (29) and (46):

$$V_{Cmin} < \frac{V_{DC}R_b}{R_l+2R_b} < \frac{R_bV_{DC}+\sqrt{R_b^2V_{DC}^2-4PR_lR_b(R_l+2R_b)}}{2(R_l+2R_b)},$$

thus, there are no real equilibrium points in $\mathbb{D}_1$.

Equilibrium points in $\mathbb{D}_2$

In $\mathbb{D}_2, \boldsymbol{f}^{-+}$ actuates. There are two equilibrium points in this field, $\boldsymbol{E}_{\mathbf{1}}^{-+}$ and $\boldsymbol{E}_{\mathbf{2}}^{-+}$, and both are virtual. First we verify

$$E_{11}^{++} < E_{11}^{-+},$$

that is

$$\frac{R_bV_{DC}+\sqrt{R_b^2V_{DC}^2-4PR_lR_b(R_l+2R_b)}}{2(R_l+2R_b)} < \frac{2V_{DC}R_lR_b+3V_{DC}R_b^2-R_b\sqrt{V_{DC}^2R_b^2-4PR_b(R_l+R_b)(R_l+2R_b)}}{2(R_l+R_b)(R_l+2R_b)},$$

which is equivalent to

$$\underbrace{(R_l+R_b)\sqrt{R_b^2V_{DC}^2-4PR_b(R_l+2R_b)}}_{<V_{DC}R_b(R_l+R_b)} < V_{DC}R_b(R_l+R_b)+\underbrace{V_{DC}R_b^2-R_b\sqrt{V_{DC}^2R_b^2-4PR_b(R_l+R_b)(R_l+2R_b)}}_{>0}.$$

That is true, so

$$V_{Cmin} < E_{11}^{++} < E_{11}^{-+},$$

therefore $\boldsymbol{E}^{-+}$ is virtual.

Now we verify that $\boldsymbol{E}_{\mathbf{2}}^{-+}$ is virtual. We have

$$E_{11}^{-+} < E_{21}^{-+},$$

that is

$$\begin{aligned}&\frac{2V_{DC}R_lR_b+3V_{DC}R_b^2-R_b\sqrt{V_{DC}^2R_b^2-4PR_b(R_l+R_b)(R_l+2R_b)}}{2(R_l+R_b)(R_l+2R_b)}\\ &< \frac{2V_{DC}R_lR_b+3V_{DC}R_b^2+R_b\sqrt{V_{DC}^2R_b^2-4PR_b(R_l+R_b)(R_l+2R_b)}}{2(R_l+R_b)(R_l+2R_b)},\end{aligned}$$

so we have

$$V_{Cmin} < E_{11}^{++} < E_{11}^{-+} < E_{21}^{-+},$$

thus, both $\boldsymbol{E}_{\mathbf{1}}^{-+}$ and $\boldsymbol{E}_{\mathbf{2}}^{-+}$ are virtual.

Equilibrium points in $\mathbb{D}_4$

In $\mathbb{D}_4, \boldsymbol{f}^{++}$ actuates. In our hypothesis, $\boldsymbol{E}_{\mathbf{1}}^{++}$ is real, and $\boldsymbol{E}_{\mathbf{2}}^{++}$ and $\boldsymbol{E}_{\mathbf{3}}^{++}$ are virtual. There is only need to verify that $\boldsymbol{E}_{\mathbf{4}}^{++}$ is virtual. We have

$$E_{41}^{++} < E_{21}^{++}.$$

That becomes, replacing (49) and (47),

$$\frac{R_bV_{DC}-\sqrt{R_b^2V_{DC}^2-4PR_lR_b(R_l+2R_b)}}{2(R_l+2R_b)} < \frac{R_bV_{DC}-\sqrt{R_b^2V_{DC}^2-4PR_b(R_l+R_b)^2}}{2(R_l+R_b)}.$$

That is true, so we have

$$E_{41}^{++} < E_{21}^{++} < V_{Cmin},$$

therefore $\boldsymbol{E_4^{++}}$ is virtual.

This concludes all the proofs that $\boldsymbol{f}$, provided that (61) and (77) are satisfied, has the elements such as Figure 48, and, as discussed in the beginning of this chapter, is globally stable.

6.5 GUIDELINES FOR THE DESIGN OF R_b - GLOBAL STABILITY OF THE OPERATING POINT IN A TWO SM SYSTEM

In chapter 3 we have seen some first guidelines for the design of R_b. Assuring the local stability conditions, we choose a γ between one and the maximum value, and calculate the corresponding R_b. In this chapter, we have seen conditions for assuring global stability - $\boldsymbol{E_1^{++}}$ being real and stable, and $\boldsymbol{E_2^{++}}$ and $\boldsymbol{E_1^{++}}$ being virtual. If it is possible, one can then choose an R_b value that ensures these conditions to attain global stability. As it is difficult to obtain a closed solution of $E_{21}^{++} < v_{Cmin}$ for R_b, one way is to do it iteratively with the aid of numerical computation tools. One can choose a γ in the range seen in (69)

$$1 < \gamma < \frac{V_{DC}^2}{4NPR_l} - 1,$$

calculate the corresponding R_b and then check whether the global stability condition (77) is satisfied. It is important to notice that greater values for γ tend to bring the saddle points apart and closer to the origin, as well as the operating point. With that in mind, the designer of R_b can choose a value trying to satisfy the global stability condition.

The condition does not depend on the values of C_i. However, uncertainties in the value of other parameters can affect the stability and position of equilibrium points. It is therefore advisable to choose a γ value still greater than the minimum sufficient value in order to have a safety margin around parameter uncertainty. Studying the stability conditions in the case of variations in the parameters V_{DC}, P_i, and R_l are beyond the scope of this work.

6.6 SUMMARY

In this chapter we have seen:

- Analytical conditions for global stability of the operating point $\boldsymbol{E_1^{++}}$ were presented and proved for a system with two SM.
- These conditions are that $\boldsymbol{E_1^{++}}$ is real and stable, and the saddle points $\boldsymbol{E_2^{++}}$ and $\boldsymbol{E_3^{++}}$ are virtual.
- These conditions can be achieved through an adequate design of the parameters R_b or V_{Cmin}, for example.
- With these satisfied, the system should be able to reach the operating point regardless of uncertainties in C_i values.

The next and final chapter concludes this thesis and suggests some ways to extend it in future works.

7 CONCLUSION

Stages 1 and 2 of the precharge operation described in chapter 1 were modeled. The resulting model was an instantaneous, piecewise-smooth nonlinear model. An analysis for a system with two submodules per phase was made. Nullclines, coordinates, existence conditions, classification and stability of equilibrium points was analyzed for the nominal system, that is, with submodules with equal parameter values. Sliding regions, coordinates, classification and stability of the system's pseudo-equilibrium points was also studied. Through that, local stability criteria for the operating point were obtained with an analytically proven solution, initially for a two submodules system and then extended for a system with an arbitrary number of submodules. These conditions help in the design of the balancing resistance.

It was also shown that it is not sufficient that the operating point is stable, but also its attraction domain must be large enough so that the trajectory corresponding to the system starting from null initial conditions, corresponding to an all capacitors discharged situation, belongs to it. Numerical simulations were made to investigate the size and shape of the attraction domain of the operating point, depending on parametric variations in the balancing resistance and in the capacitances of the submodules. The variation of the capacitances does not alter the shape of nullclines, equilibrium point coordinates, stability or classification, but it scales the vector field in a given direction, and this molds the shape of the attraction domain, therefore explaining why the variation in the capacitances can cause the system to malfunction, even though they do not influence stability properties of the equilibrium points.

Still regarding stability, conditions for global stability of a system with two submodules per phase were established and proved. These conditions also can help in the design of the balancing resistance. Experiments were conducted and their result was successfully predicted by the theory.

For future works, the same model, techniques and analysis used in this work could be made in a system with three submodules per phase. Even though it does not correspond to a typical real case, where the number of submodules per phase is even, graphical tools that help to obtain insights about the system, like the phase plane can still be used. It could be investigated if the dynamics of a system with more than two submodules per phase are similar to the ones studied in this thesis, and therefore the results from here can be extended for a system with arbitrary number of submodules, or if new phenomena arise from such configuration.

The influences of variation in another parameter may also be studied. A normalized model with reduced parameter number would perhaps be a good way to approach these questions. As a suggestion, first varying P and then considering different P_i in the SM would be a good start. Some bifurcation analysis made for typically used parameter values could be a good approach to explore.

The three-phase system may also be studied. A simplified three-phase (or even a theoretical two-phase) system with one SM per phase may be a good starting point to investigate if there are coupling dynamics in between phases and how significant they are for the capacitor voltage balancing problem.

Also, a model with minor modifications could be used to investigate similar solutions, with active balancing, based on switched balancing resistance and a control law. Some proposals of control law are comparing the voltage in the capacitor with a constant reference, another, with a reference that is the medium value of all capacitor voltages.

Numerical approaches also open perspective for future works. It can be used parameter values with limited ranges, corresponding only to the ones used in most of the practical applications. This may help to deal with the system with higher dimensions or number of SMs and also to obtain results for the system with two SMs that could not be made by analytical proofs for the general case.

A study about the stability of voltage balancing in precharge made through the MMC's AC port with is also an option. It may be used a model similar to the one proposed at this work. For that, it is necessary to study stability in non-autonomous system, because of the time-varying voltage in the AC port.

All of these works and approaches would benefit from the use of a normalized model, because the number of parameter is reduced, an consequently its complexity. Also, the results obtained from it are more general.

Finally, the techniques learned in the course of this work can be used to study other power electronic problems in which their application is suitable, or in problems similar to the voltage balancing, or even just involving piecewise smooth systems, taking into account the instantaneous and nonlinear dynamics.

REFERENCES

ADAM, Grain Philip et al. Review of dc-dc converters for multi-terminal HVDC transmission networks. **IET Power Electronics**, v. 9, n. 2, p. 281–296, 2016. ISSN 17554543. DOI: `10.1049/iet-pel.2015.0530`.

BISSAL, Ara; ALI, Waqas. A Fast Acting Precharge Control Strategy for Modular Multilevel Converters. **2019 IEEE 13th International Conference on Power Electronics and Drive Systems (PEDS)**, July, p. 1–4, 2019.

CESAR, Eduardo Lenz et al. Modelagem e análise da dinâmica de microrredes de distribuição de energia elétrica, 2017.

COTTET, Didier et al. Integration technologies for a medium voltage modular multi-level converter with hot swap capability. **2015 IEEE Energy Conversion Congress and Exposition, ECCE 2015**, p. 4502–4509, 2015. DOI: `10.1109/ECCE.2015.7310295`.

CRISTIANO, Rony et al. Bifurcation analysis in discontinuous piecewise-smooth systems: applications in power electronics, 2018.

DEBNATH, Suman et al. Operation, control, and applications of the modular multilevel converter: A review. **IEEE Transactions on Power Electronics**, IEEE, v. 30, n. 1, p. 37–53, 2015. ISSN 08858993. DOI: `10.1109/TPEL.2014.2309937`.

DEKKA, Apparao et al. Evolution of topologies, modeling, control schemes, and applications of modular multilevel converters. **IEEE Journal of Emerging and Selected Topics in Power Electronics**, IEEE, v. 5, n. 4, p. 1631–1656, 2017.

FLOURENTZOU, Nikolas; AGELIDIS, Vassilios G; DEMETRIADES, Georgios D. VSC-based HVDC power transmission systems: An overview. **IEEE Transactions on power electronics**, IEEE, v. 24, n. 3, p. 592–602, 2009.

GEYER, Tobias; DARIVIANAKIS, Georgios; VAN DER MERWE, Wim. Model predictive control of a STATCOM based on a modular multilevel converter in delta configuration. **2015 17th European Conference on Power Electronics and Applications, EPE-ECCE Europe 2015**, Jointly owned by EPE Association and IEEE PELS, p. 1–10, 2015. DOI: `10.1109/EPE.2015.7309148`.

KNAAK, Hans-joachim. Modular Multilevel Converters and HVDC / FACTS : a success story The modular multilevel technology. **Proceedings of the 14th European Conference on Power Electronics and Applications (EPE 2011)**, IEEE, n. 150, p. 1–6, 2011.

KOURO, Samir; MALINOWSKI, Mariusz, et al. Recent advances and industrial applications of multilevel converters. **IEEE Transactions on industrial electronics**, IEEE, v. 57, n. 8, p. 2553–2580, 2010.

KOURO, Samir; RODRIGUEZ, Jose, et al. Powering the future of industry: High-power adjustable speed drive topologies. **IEEE Industry Applications Magazine**, v. 18, n. 4, p. 26–39, 2012. ISSN 10772618. DOI: `10.1109/MIAS.2012.2192231`.

KUZNETSOV, Yu A.; RINALDI, S.; GRAGNANI, A. One-parameter bifurcations in planar Filippov systems. **International Journal of Bifurcation and Chaos in Applied Sciences and Engineering**, v. 13, n. 8, p. 2157–2188, 2003. ISSN 02181274. DOI: `10.1142/S0218127403007874`.

LACHICHI, A. Modular multilevel converters with integrated batteries energy storage. **3rd International Conference on Renewable Energy Research and Applications, ICRERA 2014**, IEEE, p. 828–832, 2014. DOI: `10.1109/ICRERA.2014.7016501`.

LESNICAR, A.; MARQUARDT, R. An innovative modular multilevel converter topology suitable for a wide power range - Power Tech Conference Proceedings, 2003 IEEE Bologna. **2003 IEEE Bologna PowerTech - Conference Proceedings**, v. 3, p. 1–6, 2003. DOI: `10.1109/PTC.2003.1304403`.

LI, Binbin et al. Closed-loop precharge control of modular multilevel converters during start-up processes. **IEEE Transactions on Power Electronics**, IEEE, v. 30, n. 2, p. 524–531, 2015. ISSN 08858993. DOI: `10.1109/TPEL.2014.2334055`.

LUO, Longfei. A Novel Method Based on Self-Power Supply Control for Balancing Capacitor Static Voltage in MMC. **IEEE Transactions on Power Electronics**, IEEE, v. 33, n. 2, p. 1038–1049, 2018. DOI: `10.1109/TPEL.2017.2679130`.

LUO, Longfei; CAO, Hui, et al. Based on Curve Fitting Method to Analyze and Calculate The Equalizing Resistance of Sub-modules in Series of MMC System. **2016 Chinese Control and Decision Conference (CCDC)**, p. 3677–3681, 2016.

LUO, Longfei; ZHANG, Yanbin, et al. Capacitor static voltage balance based on auxiliary-power supply pulse width control for. **IET Power Electronics**, v. 11, n. 11, p. 1796–1803, 2018. DOI: `10.1049/iet-pel.2017.0672`.

LYU, Jing; CAI, Xu; MOLINAS, Marta. Optimal design of controller parameters for improving the stability of MMC-HVDC for wind farm integration. **IEEE Journal of Emerging and Selected Topics in Power Electronics**, IEEE, v. 6, n. 1, p. 40–53, 2018. ISSN 21686785. DOI: `10.1109/JESTPE.2017.2759096`.

MARQUARDT, R. Stromrichterschaltungen mit verteilten energiespeichern. **German Patent DE10103031A1**, v. 24, 2001.

NOVAKOVIC, Bora; NASIRI, Adel. Modular multilevel converter for wind energy storage applications. **IEEE Transactions on Industrial Electronics**, IEEE, v. 64, n. 11, p. 8867–8876, 2017.

PEREZ, Marcelo A. et al. Circuit Topologies, Modelling, Control Schemes and Applications of Modular Multilevel Converters. **IEEE Transactions on Power Electronics**, v. 30, n. 1, p. 4–17, 2015. ISSN 0885-8993. DOI: `10.1109/TPEL.2014.2310127`.

SCHMIDT, Luiz H T et al. Passive Capacitor Voltage Balancing in Modular Multilevel Converter During its Precharge : Analysis and Design. **15th Brazilian Power Electronics Conference and 5th IEEE Southern Power Electronics Conference**, p. 323–328, 2019.

SIEMENS AG (Ed.). **SINAMICS PERFECT HARMONY GH150**. [S.l.: s.n.], 2017. Available from: `www.siemens.com/sinamics-perfect-harmony-gh150`.

SOUZA, Gean Jacques Maia de. Estudo de Conversores Modulares Multiníveis(MMC) Uni- e Bidirecionais. **Dept. Eng. Eletrica, Universidade Federal de Santa Catarina, Florianópolis**, n. 2100, 2014. DOI: `10.1128/JVI.00638-09`.

TIAN, Kai et al. A Simple and Cost-effective Precharge Method for Modular Multilevel Converters by Using a Low-Voltage DC Source. **IEEE Transactions on Power Electronics**, IEEE, v. 31, n. 7, p. 5321–5329, 2016. ISSN 08858993. DOI: `10.1109/TPEL.2015.2484222`.

TOH, Chuen Ling; NORUM, LE. Implementation of high speed control network with fail-safe control and communication cable redundancy in modular multilevel converter. In: IEEE. 2013 15th European Conference on Power Electronics and Applications (EPE). [S.l.: s.n.], 2013. P. 1–10.

XU, Jianzhong et al. New precharge and submodule capacitor voltage balancing topologies of modular multilevel converter for VSC-HVDC application. In: IEEE. 2011 Asia-Pacific Power and Energy Engineering Conference. [S.l.: s.n.], 2011. P. 1–4.

XUE, Yinglin; XU, Zheng; TANG, Geng. Self-Start control with grouping sequentially precharge for the C-MMC-Based HVDC System. **IEEE Transactions on Power Delivery**, IEEE, v. 29, n. 1, p. 187–198, 2014. ISSN 08858977. DOI: `10.1109/TPWRD.2013.2279106`.

ZHANG, Lei et al. A Generalized Precharging Strategy for Soft Startup Process of the Modular Multilevel Converter-Based HVDC Systems. **IEEE Transactions on Industry Applications**, v. 53, n. 6, p. 5645–5657, 2017. ISSN 00939994. DOI: `10.1109/TIA.2017.2736958`.

ZHU, Zhe et al. Testing a complete control and protection system for multi-terminal MMC HVDC links using hardware-in-the-loop simulation. In: IEEE. IECON 2014-40th Annual Conference of the IEEE Industrial Electronics Society. [S.l.: s.n.], 2014. P. 4402–4408.

ZYGMANOWSKI, Marcin; GRZESIK, Bogusław; NALEPA, Radosław. Capacitance and inductance selection of the modular multilevel converter. In: IEEE. 2013 15th European Conference on Power Electronics and Applications (EPE). [S.l.: s.n.], 2013. P. 1–10.